

July 2022

## Stability and Interaction Analysis of Inverter-Based Resources in Power Grids

Li Bao

*University of South Florida*

Follow this and additional works at: <https://digitalcommons.usf.edu/etd>



Part of the [Electrical and Computer Engineering Commons](#)

---

### Scholar Commons Citation

Bao, Li, "Stability and Interaction Analysis of Inverter-Based Resources in Power Grids" (2022). *USF Tampa Graduate Theses and Dissertations*.

<https://digitalcommons.usf.edu/etd/9295>

This Dissertation is brought to you for free and open access by the USF Graduate Theses and Dissertations at Digital Commons @ University of South Florida. It has been accepted for inclusion in USF Tampa Graduate Theses and Dissertations by an authorized administrator of Digital Commons @ University of South Florida. For more information, please contact [scholarcommons@usf.edu](mailto:scholarcommons@usf.edu).

Stability and Interaction Analysis of Inverter-Based Resources in Power Grids

by

Li Bao

A dissertation submitted in partial fulfillment  
of the requirements for the degree of  
Doctor of Philosophy  
Department of Electrical Engineering  
College of Engineering  
University of South Florida

Major Professor: Lingling Fan, Ph.D.  
Zhixin Miao, Ph.D.  
Morris Chang, Ph.D.  
Kaiqi Xiong, Ph.D.  
Achilleas Kourtellis, Ph.D.

Date of Approval:  
June 24, 2022

Keywords: Inverter-Based Resource, Stability Analysis, Reactive Power Compensation

Copyright © 2022, Li Bao

## Acknowledgments

First, I would like to express my gratitude to my advisor, Dr. Lingling Fan, who provided constant support and guidance to help me become a qualified Ph.D. Without her instruction, this work would not have been possible.

Second, I would like to thank to Dr. Zhixin Miao for his support on teaching lab and project. Also, I am grateful to my defense committee members: Dr. Morris Chang, Dr. Kaiqi Xiong, Dr. Achilleas Kourtllis and Dr. Zhenyu Wang for their insightful comments and suggestions.

Further, I would like to thank my colleagues from Smart Grid Power System (SPS) Laboratory at University of South Florida, in particular: Dr. Anas Almunif, Dr. Yin Li, Dr. Minyue Ma, Dr. Yangkang Xu, Yi Zhou, Dr. Miao Zhang, Rabi Kar, Dr. Abdullah Alassaf, Zhengyu Wang, Ratik Mittal, Huazhao Ding, Ali Aljumah. You all show me a great courage against the global pandemic in last two years.

Last but not least, I owe my deepest thanks to my parents, Kaiwei Zhao and Hui Bao, for their endless love and encouragement.

## Table of Contents

List of Tables . . . . .	iii
List of Figures . . . . .	iv
Abstract . . . . .	vii
Chapter 1: Introduction . . . . .	1
1.1 Background . . . . .	1
1.2 Stability Analysis of VSC Connected to Weak Grid . . . . .	2
1.3 Stability Enhancement . . . . .	5
1.3.1 SynCon and STATCOM . . . . .	5
1.3.2 STATCOM Controller Interaction . . . . .	6
1.3.3 Study Approaches . . . . .	8
1.4 List of Publication . . . . .	9
1.5 Outline of Dissertation . . . . .	10
Chapter 2: Methodology of Modeling and Analysis . . . . .	11
2.1 Description of System . . . . .	11
2.2 Hardware Test Bed Setup . . . . .	13
2.2.1 Hardware Test Bed Challenge . . . . .	20
2.3 Simulation Test Bed . . . . .	21
2.4 Admittance-Based Model . . . . .	21
2.4.1 Harmonic Injection Process . . . . .	22
2.4.1.1 Harmonic Injection in MATLAB Test Bed . . . . .	28
2.4.1.2 Harmonic Injection with MATLAB Script . . . . .	28
2.4.1.3 Harmonic Injection in PSCAD . . . . .	31
2.4.2 Analytical Model . . . . .	37
2.4.2.1 Eigenvalue Analysis . . . . .	40
2.4.2.2 Bode Response Model . . . . .	40
2.5 System Parameters . . . . .	41
Chapter 3: Investigation of Weak Grid Oscillations . . . . .	42
3.1 Introduction . . . . .	42
3.2 P/Q Control with Parameters I . . . . .	42
3.3 P/Q Control with Parameters II . . . . .	43
3.4 P/V Control with Parameters I . . . . .	43
3.5 P/V Control with Parameter II . . . . .	44
3.6 Analytical Model Validation . . . . .	44

3.7	Summary . . . . .	48
Chapter 4:	IBR System with VAR Devices . . . . .	49
4.1	Comparison of SynCon and STATCOM . . . . .	49
4.1.1	Model Description . . . . .	49
4.1.1.1	Wind Farm . . . . .	49
4.1.1.2	STATCOM . . . . .	49
4.1.1.3	SynCon . . . . .	59
4.1.2	EMT Simulation Results . . . . .	60
4.1.2.1	Wind Farm Only . . . . .	60
4.1.2.2	Wind Farm with STATCOM . . . . .	61
4.1.2.3	Wind Farm with SynCon . . . . .	65
4.1.3	Admittance Model Extraction . . . . .	66
4.1.4	Stability Analysis . . . . .	68
4.1.4.1	Wind Farm Only . . . . .	70
4.1.4.2	Wind Farm with STATCOM . . . . .	70
4.1.4.3	Wind Farm with SynCon . . . . .	71
4.1.5	Comparison of Admittance of STATCOM and SynCon . . . . .	71
4.2	Controller Interaction of STATCOM in Type-4 Wind Farm System . . . . .	75
4.2.1	STATCOM on Type-4 Wind Farm . . . . .	75
4.2.2	Linear System Identification . . . . .	77
4.2.3	Impact of STATCOM Controller on System's Stability . . . . .	81
Chapter 5:	Conclusion and Future Work . . . . .	85
5.1	Conclusion . . . . .	85
5.2	Future Work . . . . .	86
5.2.1	Eigenvalue Analysis for PQ/V $\theta$ Model . . . . .	86
5.2.2	Participation Factor Analysis . . . . .	88
References	. . . . .	89
Appendix A:	Copyright Permissions . . . . .	96
About the Author	. . . . .	End Page

## List of Tables

Table 2.1	Hardware test bed devices . . . . .	19
Table 2.2	Parameters of the circuit . . . . .	41
Table 2.3	Parameters of the controller . . . . .	41
Table 3.1	Results comparison . . . . .	48
Table 4.1	Parameters of the type-4 wind farm . . . . .	51
Table 4.2	Parameters of STATCOM . . . . .	58
Table 4.3	Parameters of synchronous condenser . . . . .	60

## List of Figures

Figure 1.1	U.S. electricity generation prediction. . . . .	1
Figure 1.2	Texas low-frequency oscillation. . . . .	3
Figure 1.3	The installation of SynCon in Kiamal, South Australia. . . . .	7
Figure 2.1	Configuration of grid-connected three-phase VSC and its control system. . . . .	12
Figure 2.2	Block diagram of PLL. . . . .	12
Figure 2.3	Configuration of the hardware test bed. . . . .	14
Figure 2.4	LabVIEW development system. . . . .	16
Figure 2.5	RT-Lab model structure. . . . .	17
Figure 2.6	RT-Lab and Imperix module connection. . . . .	18
Figure 2.7	Configuration of EMT model. . . . .	22
Figure 2.8	Block diagram of injection system. . . . .	26
Figure 2.9	Block diagram of PQ/ $V\theta$ injection system. . . . .	27
Figure 2.10	Model setup for harmonic injection. . . . .	29
Figure 2.11	Dq-axis injected signals. . . . .	31
Figure 2.12	Admittance comparison of harmonic injection and frest. . . . .	32
Figure 2.13	Configuration of PSCAD model for harmonic injection. . . . .	33
Figure 2.14	(a) Three-phase voltage signals generation. . . . .	34
Figure 2.15	Identifier number for (a) d-axis voltage harmonic signal. . . . .	35
Figure 2.16	(a) RTP/COMTRADE Recorder block. . . . .	35
Figure 2.17	PSCAD harmonic injection data in folder. . . . .	37
Figure 2.18	Flowchart for harmonic injection in PSCAD model. . . . .	38

Figure 2.19	Configuration of analytical model. . . . .	39
Figure 3.1	Response of P, Q and PCC voltage under P/Q control with Parameters I when P is given a step change from 1.65 pu. . . . .	43
Figure 3.2	Response of P, Q and PCC voltage under P/Q control with Parameters II when P is given a step change from 1.58 pu. . . . .	44
Figure 3.3	Response of P, Q and PCC voltage under P/V control with Parameters I when P is given a step change from 1.92 pu. . . . .	45
Figure 3.4	Response of P, Q and PCC voltage under P/V control with Parameters II when P is given a step change from 1.53 pu. . . . .	45
Figure 3.5	Steady-state operation condition comparison of EMT model and analytical model under (a) P/V control, (b) P/Q control. . . . .	46
Figure 3.6	Eigen loci for different cases, interval for each point is 0.02 pu. . . . .	47
Figure 4.1	EMT test bed structure of a type-4 wind farm with reactive power devices. . . . .	50
Figure 4.2	GSC control structure. . . . .	51
Figure 4.3	STATCOM circuit and control. . . . .	52
Figure 4.4	STATCOM operation. . . . .	54
Figure 4.5	STATCOM dynamic performance analysis. . . . .	55
Figure 4.6	System configuration of 48-pulse GTO-VSC based STATCOM. . . . .	56
Figure 4.7	Comparison of $\alpha$ and $\alpha_v$ . . . . .	57
Figure 4.8	Voltage control block diagram of STATCOM. . . . .	58
Figure 4.9	Synchronous condenser exciter model. . . . .	59
Figure 4.10	Voltage at PCC bus in wind farm system. . . . .	61
Figure 4.11	(a) Voltage at PCC bus and reactive power from STATCOM. . . . .	62
Figure 4.12	(a) System dynamic performance comparison of different PI controller when $X_g$ increases to 0.42 pu. . . . .	63
Figure 4.13	STATCOM open loop control system. . . . .	63
Figure 4.14	With open loop control, voltage at PCC bus and the reactive power from the STATCOM when (a) $X_g$ increases to 0.42 pu. . . . .	64



Figure 4.15	Voltage at PCC bus and the reactive power from the STATCOM when (a) $X_g$ increases to 0.41 pu and 0.42 pu with Para I. . . . .	64
Figure 4.16	Voltage at PCC bus and the reactive power from the STATCOM when $X_g$ increases to 0.49 pu and 0.50 pu with Para II. . . . .	65
Figure 4.17	(a) Voltage at PCC bus and synchronous condenser reactive power in wind farm system when $X_g$ changes from 0.20 to 0.42 pu. . . . .	66
Figure 4.18	Simplified system diagram using harmonic injection. . . . .	66
Figure 4.19	Comparison of the wind farm admittance model from vector fitting and harmonic injection measurement points. . . . .	67
Figure 4.20	Eigen loci for varying line impedance $X_g$ for (a) wind farm, (b) wind farm with STATCOM, and (c) wind farm with SynCon. . . . .	72
Figure 4.21	$Dq$ -domain admittance comparison of synchronous condenser and STATCOM. . . . .	73
Figure 4.22	Equivalent circuit model of a wind farm connected with a SynCon. . . . .	74
Figure 4.23	PCC bus voltage and reactive power from STATCOM under voltage and reactive power control. . . . .	76
Figure 4.24	PCC bus voltage and reactive power from STATCOM with fixed firing angle control. . . . .	77
Figure 4.25	Block diagram of STATCOM control systems. . . . .	78
Figure 4.26	Signal injection for obtaining frequency response. . . . .	79
Figure 4.27	Comparison of the linear model from vector fitting and harmonic injection for (a) reactive power control, (b) voltage control. . . . .	80
Figure 4.28	Comparison of step change responses. . . . .	81
Figure 4.29	Root locus diagram for reactive power control. . . . .	82
Figure 4.30	PCC bus voltage when $X_g$ increases to 0.42 pu at 1 second. . . . .	82
Figure 4.31	Root locus diagram for voltage control. . . . .	83
Figure 4.32	PCC bus voltage and reactive power from STATCOM under voltage control with different gains. . . . .	84
Figure 5.1	A transmission line impedance. . . . .	87

## Abstract

The increasing penetration of inverter-based resources (IBRs) introduces some unexpected dynamic issues, including low-frequency oscillations. To investigate these phenomenon, a laboratory-scale grid-following voltage-source converter (VSC) system is implemented to demonstrate weak grid oscillations. Grid-following control is applied in VSC to provide active power, reactive power or ac voltage control. The test bed is also replicated in electromagnetic transient (EMT) simulation environment (MATLAB/SimPowerSystems) for benchmark purpose. Case studies are carried out to demonstrate low-frequency oscillations under real power/ac voltage or real power/reactive power control. An analytical model is carried out to examine the stability condition and compared with EMT or hardware test bed results by using eigenvalue analysis.

To enhance the stability of an IBRs-integrated power system, reactive power (VAR) compensation is an effective method. Synchronous condenser (SynCon) and static synchronous compensator (STATCOM) are widely used among VAR devices. They have the capability of increasing the transmission system stability and efficiency by absorbing or generating reactive power. A comparison of SynCon and STATCOM under the condition of zero reactive power injection will be presented. The two devices are integrated into a grid-connected type-4 wind farm to examine their effects on system stability. It is found that SynCon is capable of stability enhancement while STATCOM does not have such capability. To explain the difference, we measure the  $dq$ -frame admittance frequency-domain responses of the two devices using frequency scans. Vector fitting method is then utilized to convert the admittance frequency-domain measurements to an  $s$ -domain model.  $s$ -domain admittance-based eigenvalue analysis further confirms that SynCon is advantageous in stability enhancement. The

difference of SynCon and STATCOM can be summarized as SynCon providing a steady-state reactance while STATCOM acting as a current source at steady state.

Moreover, the controller interaction of STATCOM in type-4 wind farm system is also investigated. Reactive power and voltage control are implemented on STATCOM controller. The control loops are disconnected and a series of harmonic signals are injected into the system. With the frequency response data, a linear model can be derived using vector fitting method. Then, the stability analysis for different control parameters are carried out by root locus diagram. The proposed method is tested in a type-4 wind farm system, EMT simulation results verify the accuracy of the stability analysis.

## Chapter 1: Introduction

### 1.1 Background

The power grid around the world is undergoing a continuously transformation due to the growth shares of renewable energy, such as wind farm and solar photovoltaic. This change is partly supported by government in order to transfer current energy use to renewable energy. In December 2021, the Bide administration proposed an ambitious decarbonization plan that aims to 100 percent clean energy by 2030, and net-zero emissions from overall federal operations by 2050. Specifically, the U.S. Energy Information Administration (EIA) predicts that the share of renewable energy in the U.S. electricity generation mix will increase from 21% in 2020 to 42% in 2050, of most which come from wind and solar photovoltaic [1]. Fig. 1.1 shows the prediction of U.S. electricity generation.

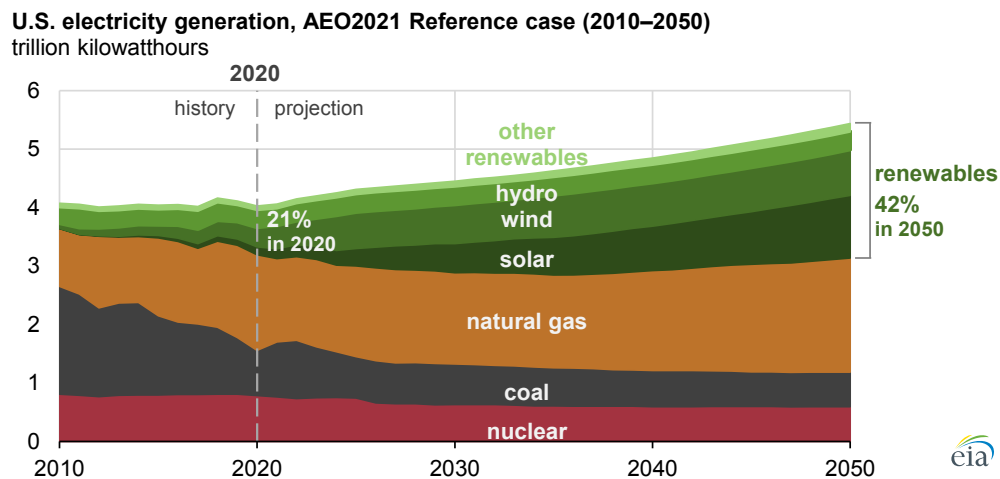


Figure 1.1: U.S. electricity generation prediction. This figure is from [1].

Since wind and solar energy are connected to grid with power electronic inverters, they can be referred as inverter-based resources (IBRs). The increasing penetration of IBRs changes

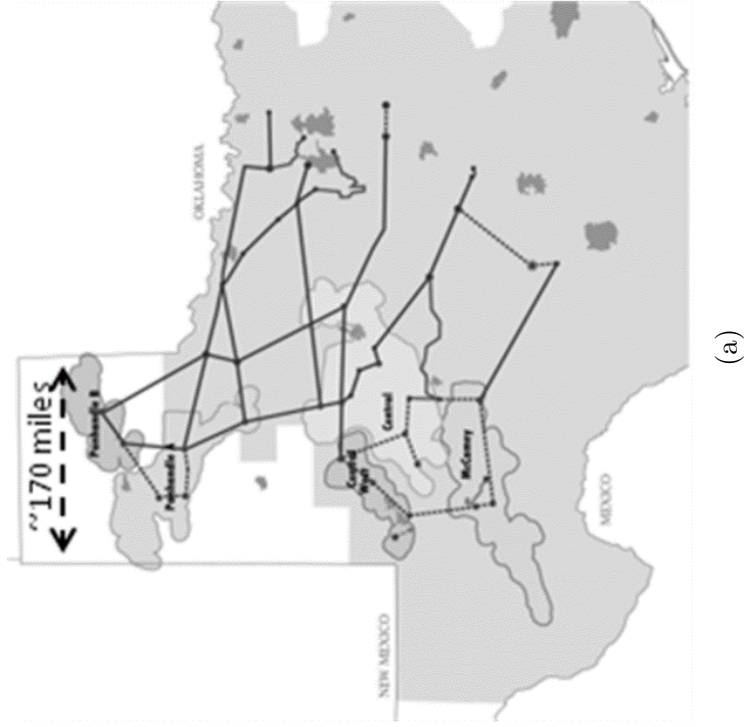
the traditional power system's properties. Synchronous generators dominate the traditional power system, which has large inertia and strong damping ability [2]. The system has a good stability performance against to common disturbances or oscillations. In contrast, the IBRs use voltage source converters (VSCs), which has low inertia and weak damping ability. Hence, dynamic stability becomes a major concern in maintaining the normal operation of power grids due to the increasing shares of IBRs. An oscillation may not be damped quickly and endanger the system operation.

In real-world operation, the IBRs related low-frequency oscillations have been observed. For example, in China, subsynchronous oscillations (SSO) events were observed in the Type-4 wind farm with a relatively weak transmission network [3]. In Texas, Electric Reliability Council of Texas (ERCOT) observed oscillations at 4 Hz in a wind power plant under weak grid condition. Fig. 1.2 shows the topology of transmission system and voltage oscillation waveform [4]. These instability issues happened due to the transferred power reaches to limit. The issue of low-frequency oscillation related to wind farm in weak grids has been studied in [5–8].

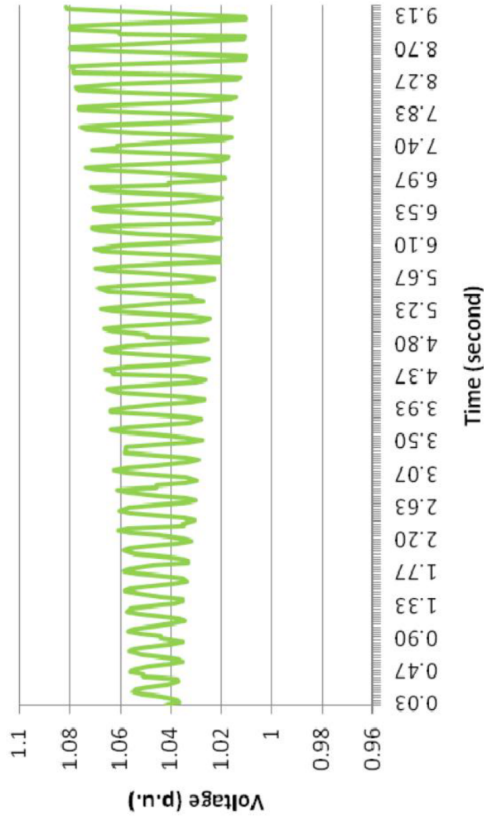
## 1.2 Stability Analysis of VSC Connected to Weak Grid

The application of power converters is increasing with the development in power electronics technology [9]. They are widely used in generation, transmission, and distribution system. For example, the renewable energy sources such as wind farms and solar photovoltaics employ large amount of power converters [10, 11]. Among these converters, three-phase VSCs serve as the interface of grid integration [12–14]. Indeed, VSCs have been key components in high-voltage direct-current (HVDC) transmission systems, machine drives, and flexible AC transmission systems (FACTS) [15, 16].

Currently, the majority of wind and solar adopts grid-following control strategy for the grid-connected VSCs. Operating in weak grids has been identified as a critical challenge for grid-following converter-interfaced IBRs by the grid industry worldwide. Specifically,



(a)



(b)

Figure 1.2: Texas low-frequency oscillation. (a) Competitive Renewable Energy Zone (CREZ) transmission system. (b) Recorded voltage measurement [4]. Permission is included in Appendix A.

weak grid oscillation is an issue that has been observed in real world. Several weak grid oscillation events in wind farms have been documented in IEEE PES TR-80 “Wind Energy Systems Subsynchronous Oscillations: Events and Modeling” [17]. IEEE IBR SSO Taskforce collected 19 events over the past decade, which are categorized as series capacitor SSO and weak grid SSO [18]. In addition, NERC has documented several wind farm and solar PV low-frequency oscillation events due to weak grid operation from 2010-2016 [19].

This issue of low-frequency oscillations due to IBR in weak grids has been studied by the senior authors, e.g., in [5–8]. While the senior authors have conducted preliminary research on mechanism and mitigation strategy of weak grid oscillations in grid-following converters in [5–8], the study scope focuses on grid-following converters with ac voltage control. Many other possible control structures, e.g., reactive power control mode, volt-var droop control, have not been considered in the prior research. In addition, results from hardware test beds are desired to provide an additional layer of verification.

A hardware test bed consisting of a SiC VSC, a 45-kW Chroma grid simulator, and passive components such as resistors, inductors, and capacitors, has been built to represent an IBR with weak grid interconnection. A corresponding EMT test bed is built in MATLAB/SimPowerSystems. This computer simulation test bed is developed to mirror the laboratory test bed except that the VSC assumes average model with 5000-Hz pulse width modulation switching sequence not modeled for computing efficiency.

Different control methods such as P/Q and P/V control are utilized to examine the active power limit and oscillation. Results show that the oscillation can be observed in a P/V control system regardless of the controller parameters. By contrast, the P/Q control system only has the oscillation under specific parameters.

The object of this section is to demonstrate weak grid low-frequency oscillations of a grid-connected VSC system with ac voltage control or var control in both hardware and simulation. This is the first step of an overall research goal that aims to develop a sta-

bility enhancement strategy and validate the strategy through hardware experiments for technology readiness.

### 1.3 Stability Enhancement

In order to enhance voltage stability, reactive power compensation is an effective method. This method can improve the stability of power system by increasing the maximum transferred power, and also help maintain a constant voltage profile [20]. SynCon and STATCOM are two major devices for reactive power compensation.

#### 1.3.1 SynCon and STATCOM

SynCon have been applied in power systems for a very long time. A reference in 1911 [21] presents the common applications of synchronous condenser at that time. Essentially, a synchronous condenser is a synchronous machine without a prime mover, working at motor operation. It is controlled by the excitation system to absorb or generate reactive power based on the requirement of power system. By the end of 2018, 90% of total generation capacity in Texas Panhandle area is wind generation. In order to enhance the stability and transmission efficiency, in April 2018, ERCOT installed two synchronous condensers with rated capacity as +175/-125 MVA at 345 kV substations in Panhandle, resulting in a 13% increase of power transfer compared that in of Year 2017 [22]. Reference [23] describes the project of installing four synchronous condensers with 13.8 kV at Vermont Electric Power Company (VELCO)'s Granite 230/115 kV station in Williamstown Vermont. This upgrade project improved the reliability and stability of the Vermont power grid.

In recent decades, STATCOMs also have been widely utilized with the development of switching devices such as IGBT and GTO [24]. A STATCOM consists of a voltage source converter and a capacitor, which is capable of regulating reactive power transfer to the power system and maintaining the voltage of network. Compared to a synchronous condenser, STATCOM does not involve a rotating machine. It becomes the major reactive



power device in the market. In May 2001, the VELCO commissioned a project involving a STATCOM-based compensation system, which has a rated capacity of +133/-41 MVA, at Essex 115 kV station [25].

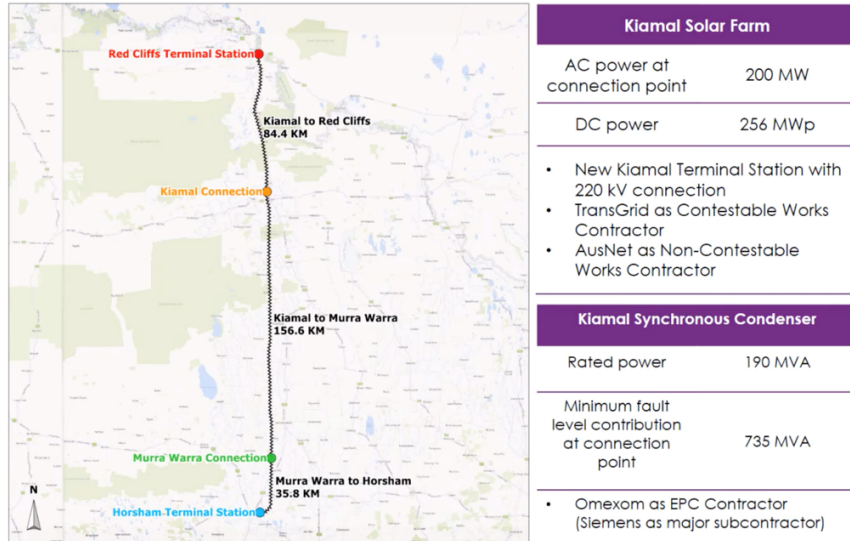
Even though both SynCon and STATCOMs are vastly installed by utility companies, SynCon is used more in islanded power grids, e.g., Kauai of Hawaii, as shown in [26], and in zones with low SCR, e.g., South Australia [27]. Fig. 1.3 illustrates the wind farm system and SynCon in Kiamal, South Australia. Apart from reactive power compensation, SynCon is used to enhance grid strength and provide inertia and fault currents.

### 1.3.2 STATCOM Controller Interaction

As a reactive power compensation device, STATCOM is popularly used to provide reactive power support. However, unwanted interaction of STATCOM controller and wind farm may occur. The controller interaction of STATCOM and wind farm may bring oscillation issues to the system. A STATCOM related oscillation is presented in [29], where different frequencies' oscillations are observed in real-world. It is found that this phenomenon is related to the number of online STATCOMs and grid strength, and the controller is not investigated. Thus, the objective of this paper is to investigate how STATCOM's controller affects the system's performance.

The study of controller interactions can be done using root locus analysis. A detailed linear model is necessary for the analysis, but it is difficult to derive the linear model because the system's parameters and control structure are confidential. Thus, harmonic injection, or frequency scanning, is an alternative method to obtain the small-signal frequency response. The detailed information of the system is not required, only inputs/outputs are used for observed. The results from harmonic injection can be fitted into a transfer function using vector fitting [30]. With the obtained linear model, root locus analysis will be carried out to investigate the stability condition under different PI controller gains.

## KIAMAL SOLAR FARM CONNECTION



(a)

## KIAMAL SYNCHRONOUS CONDENSER



(b)

Figure 1.3: The installation of SynCon in Kiamal, South Australia. (a) Solar farm connection. (b) SynCon construction [28].

Some previous literatures discussed the influence and selection of STATCOM PI controller gains. For example, in [31], the PI controller gains are adjusted in real time with an adaptive approach. In [32], the gains are designed based on a proposed fuzzy PI control method. However, these works focus on the PI controller tuning and need complicated calculation process. This paper investigates the impact of STATCOM PI controller gains on the system stability without the knowledge of system. It also provides a general approach for the stability analysis and can be used in other power system as well.

### 1.3.3 Study Approaches

Both electromagnetic transient (EMT) simulation and eigenvalue analysis are employed in this research to examine SynCon and STATCOM's performance for a type-4 wind farm with weak grid interconnection.

For eigenvalue analysis, we adopt  $s$ -domain admittance-based eigenvalue analysis. This method was proposed by Semleyn in 1999 [33] and has been found applications for inverter-based resource stability analysis recently [34]. The benefit of this approach is that we no longer need to derive a state-space model. Rather, we can obtain admittance model through measurements. This feature is especially useful for EMT simulation models. For example, the STATCOM model employed in this study is a 48-pulse GTO-based model. State-space modeling approach requires derivation of an average model in a  $dq$ -frame. On the other hand, this step is saved by utilizing measurements.

By applying a voltage harmonic disturbance at the device's terminal with a range of frequency and measuring the excited response at desired frequency, the frequency-domain measurements can be obtained. Then the vector-fitting method is carried out to derive the  $s$ -domain model representation of the targeted model. The vector fitting method is for rational approximation through finding poles and residues iteratively based on the measured points [30]. The Matlab toolbox of the method is available in public and this toolbox has been used by researchers to conduct data fitting of frequency-domain measurements, e.g., [35].

## 1.4 List of Publication

1. L. Bao, L. Fan and Z. Miao, *Wind farms in weak grids stability enhancement: SynCon or STATCOM?*, Electric Power Systems Research, vol. 202, p. 107623, 2022.
2. Z. Wang, L. Bao, L. Fan, Z. Miao, S. Shah, *From Event Data to Wind Power Plant DQ Admittance and Stability Risk Assessment*, IEEE Transactions on Power Systems, pages 1–1, 2022.
3. L. Bao, L. Fan, Z. Miao and Z. Wang, *Hardware Demonstration of Weak Grid Oscillations in Grid-Following Converters*, 2021 53rd North American Power Symposium (NAPS), 2021
4. L. Bao, L. Fan and Z. Miao, *Controller Interaction of STATCOM in Type-4 Wind Farm System*, accepted, 2022 IEEE Power Energy Society General Meeting (PESGM)
5. L. Bao, L. Fan and Z. Miao, *Comparison of Synchronous Condenser and STATCOM for Wind Farms in Weak Grids*, 2020 52nd North American Power Symposium (NAPS), 2021
6. L. Bao, L. Fan and Z. Miao, *Real-time simulation of electric vehicle battery charging systems*, 2018 North American Power Symposium (NAPS), pages 1–6, Sep. 2018.
7. L. Bao, L. Fan and Z. Miao, *Modeling and Analysis of Single-phase Boost Converter with Power Factor Correction Control*, 2020 52nd North American Power Symposium (NAPS), 2021
8. L. Bao, L. Fan and Z. Miao, *Real-Time Simulation of Level 1, Level 2, and Level 3 Electric Vehicle Charging Systems*, arXiv preprint arXiv:2111.02506, 2021
9. Yin Li, Lingling Fan, L. Bao and Z. Miao, *CHIL Testbed of Consensus Control-Based Battery Energy Storage Systems*, 2020 52nd North American Power Symposium (NAPS), 2021

10. M. Zhang, L. Bao, Z. Miao, L. Fan and P. Gomez *Measured Admittance Model for Dynamic Simulation of Inverter-Based Resources Using Numerical Laplace Transform*, 2021 53rd North American Power Symposium (NAPS), 2021

## 1.5 Outline of Dissertation

The dissertation is organized as follows.

Chapter 2 focuses on the modeling of a three-phase VSC to grid. System topology and control algorithm are presented. The EMT, hardware experiment and admittance-based model are built. Procedure of admittance-based modeling in MATLAB and PSCAD is well demonstrated.

Chapter 3 presents four case studies are carried out under different control methods and different parameters. Results from EMT model, hardware test bed and admittance-based model are compared and validated.

Chapter 4 shows the stability enhancement in a type-4 wind farm system and their controller interaction. Two VAR devices, STATCOM and SynCon, are introduced and compared under zero reactive power compensation. And  $dq$ -frame admittance models of the two devices are found through harmonic injection to illustrate their difference. The controller interaction of STATCOM and type-4 wind farm is investigated with linear model and root locus.

Chapter 5 concludes the dissertation and presents the future work of my research.

## Chapter 2: Methodology of Modeling and Analysis

This chapter demonstrates the modeling of a weak grid-connected VSC system in EMT, hardware and analytical model.

### 2.1 Description of System

The test system is a three-phase VSC connected to grid through a transmission line. The modeling of the power circuit and VSC's control system are presented in Fig. 2.1, where upper part shows circuit topology and lower part is vector control block. The power direction and corresponding variables are also illustrated in this figure.  $R_1$  and  $L_1$  represent the choke filter impedance,  $C_f$  is the filter capacitor,  $R_g$  and  $L_g$  are the grid transmission line impedance, P and Q are the active and reactive power from VSC to grid,  $v_a$ ,  $v_b$  and  $v_c$  represent the three-phase voltage of PCC bus. A PLL is used to synchronize the VSC by tracking the PCC voltage V. PLL uses the PCC bus three-phase instantaneous voltage as input, and generates the voltage's magnitude, frequency and phase angle. The control block is shown in Fig. 2.2.

The vector control system applies synchronous  $dq$ -frame, which converts time-variant three-phase variables into dc time-invariant values. Two cascaded loops are included in the control system based on the  $dq$ -variants. Inner loop controls currents in  $dq$ -frame and outer loop controls P and Q (or V). The PLL provides an angle  $\theta$  for the  $abc$  to  $dq$  conversion. PCC voltage is decoupled into  $v_d$  and  $v_q$  through PLL, at steady state,  $v_d$  is aligned to PCC voltage and  $v_q$  is kept as zero. The active power and reactive power can be expressed in (2.1).

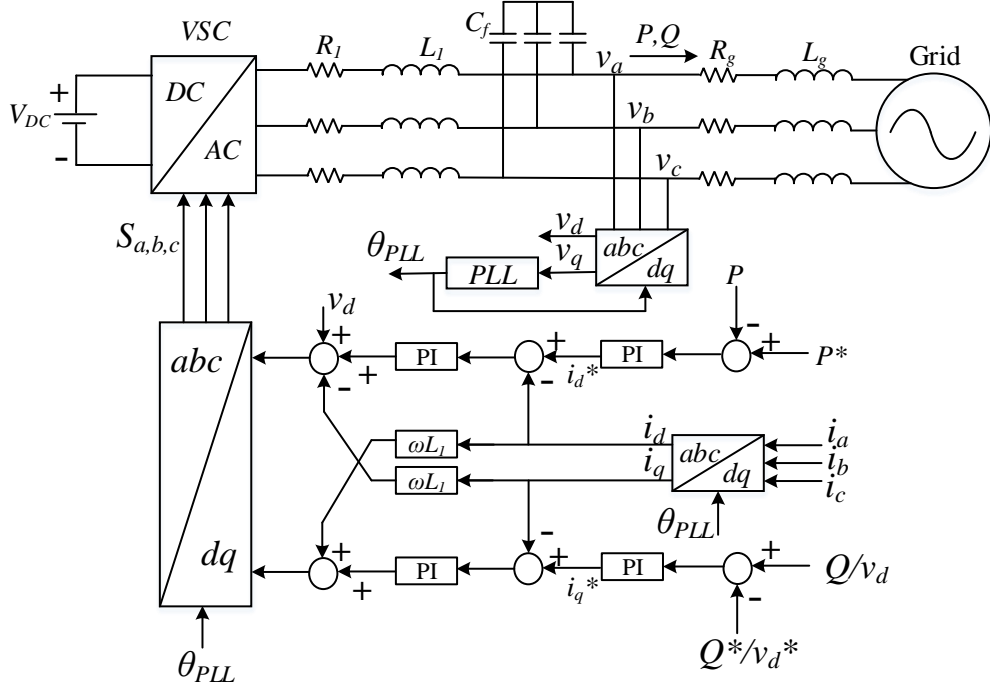


Figure 2.1: Configuration of grid-connected three-phase VSC and its control system.

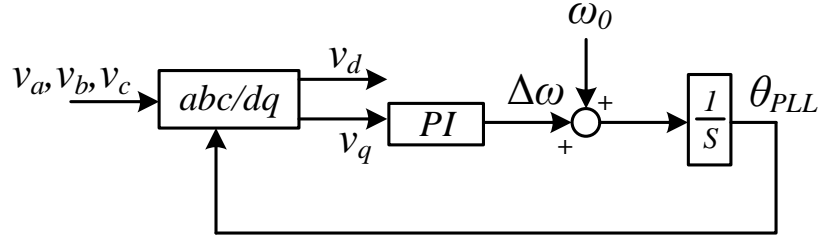


Figure 2.2: Block diagram of PLL.

$$P = v_d i_d + v_q i_q \quad (2.1)$$

$$Q = v_q i_d - v_d i_q$$

Since  $v_q$  is controlled as zero, it can be concluded that  $P$  and  $Q$  are directly proportional to  $i_d$  and  $i_q$ , respectively. Therefore, the inner-loop reference  $i_d^*$  and  $i_q^*$  are generated from outer-loop  $P$  control and  $Q$  control. Then (2.1) can be simplified as (2.2).

$$P = v_d i_d \quad (2.2)$$

$$Q = -v_d i_q$$

Hence, to regulate active power, the d-axis current can be adjusted, while the  $q$ -axis current can be adjusted for reactive power control. In addition, because of the relationship in (2.1), it can be seen that the active power related control should employ negative feedback control while the reactive power or ac voltage control should adopt positive feedback control.

Assuming that there is no converter power loss, the DC-link capacitor dynamics can be expressed in (2.3).

$$\frac{C_{dc}}{2} \frac{dV_{dc}^2}{dt} = P_{wind} - P \quad (2.3)$$

where  $P_{wind}$  is the total power injection from the wind turbine to the dc-link capacitor and the GSC.

Equation (2.3) illustrates the d-axis current order  $i_d^*$  can be generated by DC-link voltage control. Due to the DC-link voltage relationship and the active power  $P$ , its can be seen that a positive feedback should be employed for DC-link voltage control. The  $dq$ -axis current orders ( $i_{dq}^*$ ) for inner controller are from outputs of the dc and ac voltage controllers.

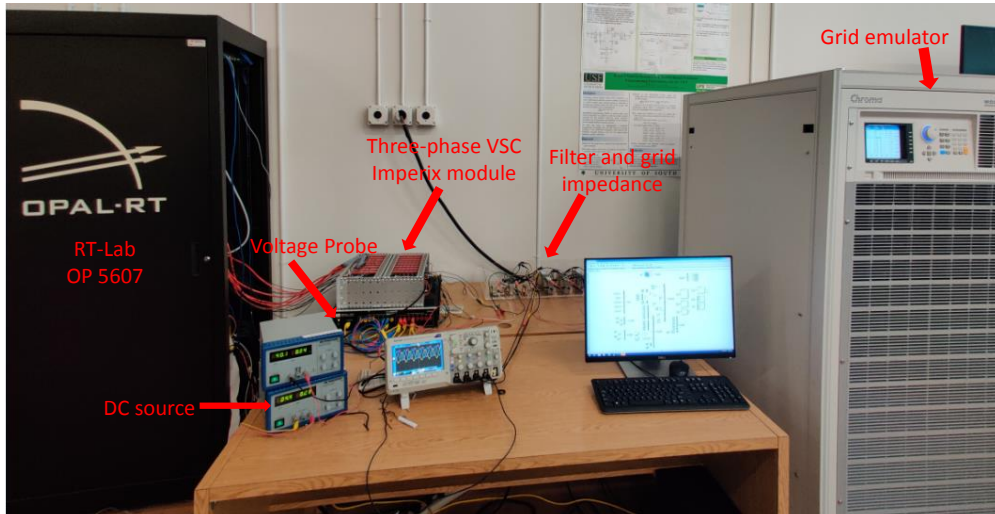
## 2.2 Hardware Test Bed Setup

The VSC system shown in Fig. 2.1 is setup in experimental test bed. The configuration is presented in Fig. 2.3. The grid is realized by a Chroma Grid Simulator 61845, three-phase VSC is composed by a three-pack Imperix PEB-8024 silicon carbide power module, and a BK Precision DC power supply is used as DC voltage source for VSC.

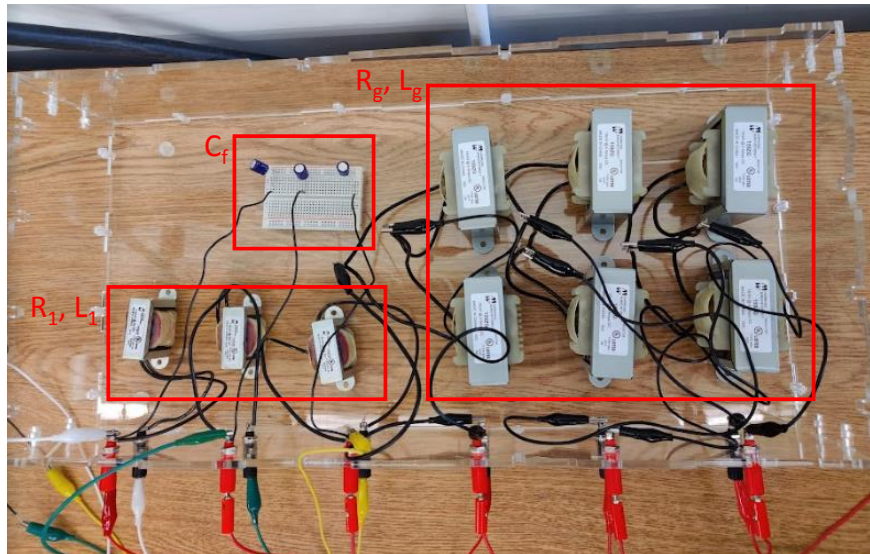
The PCC bus voltage is measured by an OPAL-RT OP8662 High Voltage Probe, measured signals are sent to RT-Lab OP5607 through its analog input ports. Current signals are collected by current sensors, which embedded in the Imperix module, and also sent to RT-Lab via RJ45 connectors.

The grid emulator Chroma 61845 is implemented with National Instruments LabVIEW Development System on a Windows Operation System. The necessary drivers are down-





(a)



(b)

Figure 2.3: Configuration of the hardware test bed. (a) Hardware test bed connection. (b) Filter and grid impedance.

loaded in chromausa official website, and a guide is found in [36]. The LabVIEW development system is shown in Fig. 2.4. Front panel includes measurement windows for voltage, current, real and reactive power. Moreover, the magnitude, frequency and phase sequence of voltage are also configured in front panel. In block diagram, a current limit with 10 A is used to protect the circuit.

These voltage and current measurements are received and processed by a Real-Time simulator RT-Lab OP5600, which will generate PWM signals to control VSC MOSFET gates. The data processing and control system are firstly built in MATLAB/SimPowerSystems environment, then RT-Lab will convert the model to C code automatically. A RT-Lab model typically consists of two subsystems as subsystem master (SM) and subsystem console (SC). During the converting, RT-Lab is able to detect SM and SC, and a CPU core will be assigned to an SM while SC does not occupy any calculation usage. Fig. 2.5 shows the RT-Lab structure and work.

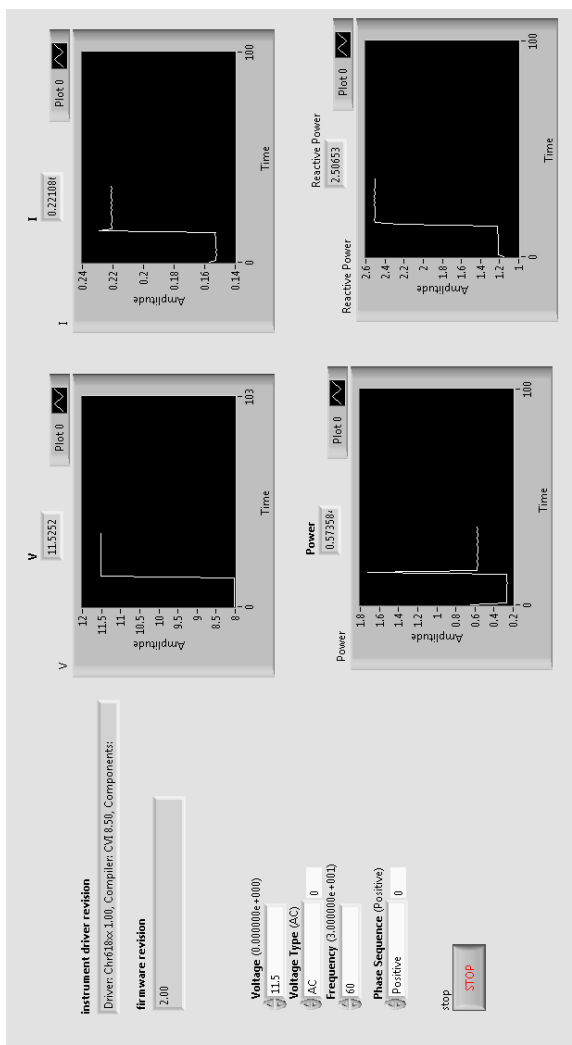
In this test bed, SM implements these functions as follows.

- Receive and filter the measured voltage and current signals.
- Convert the three-phase variables to  $dq$ -frame and generate control signals through the control system.
- Generate and output PWM signals.
- Read, record data and send to SC.

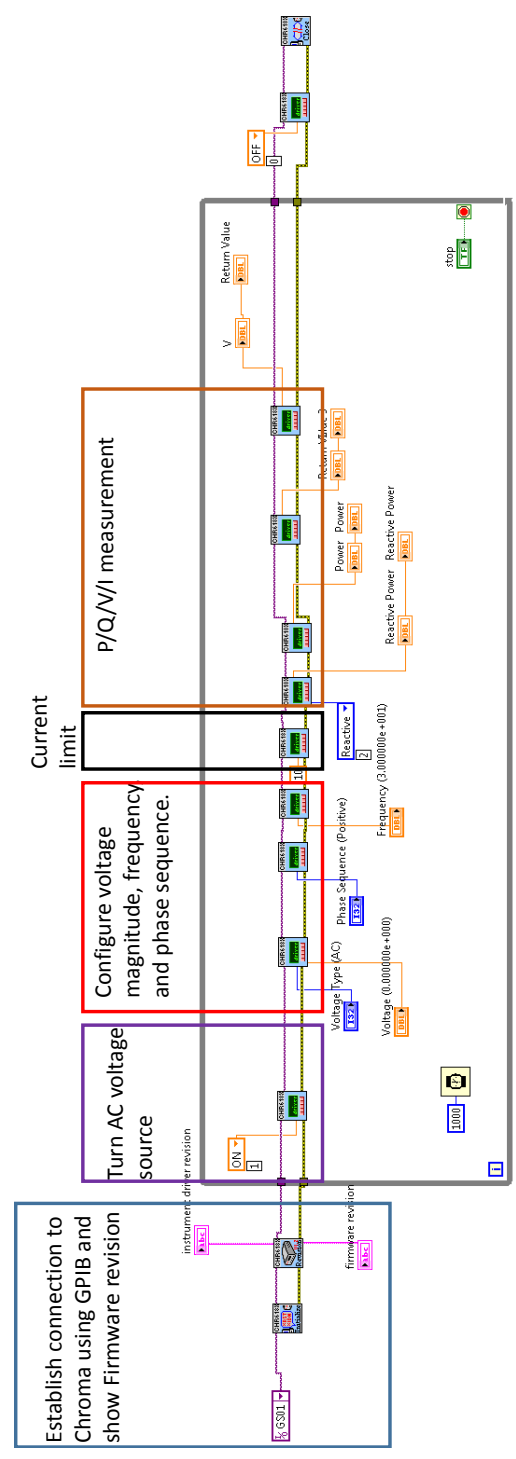
Meanwhile, SC implements these function as follows.

- Monitor circuit operation variables in scope.
- Manipulate the control system such as switch Q or V control, adjust P or Q/V reference, and change control parameters during operation.

After PWM signals are generated by RT-Lab, they will be transferred to Imperix module by optical fibers. The front side of RT-Lab, and its connection to Imperix modules are shown



(a)



(b)

Figure 2.4: LabVIEW development system. (a) Front panel. (b) Block diagram.

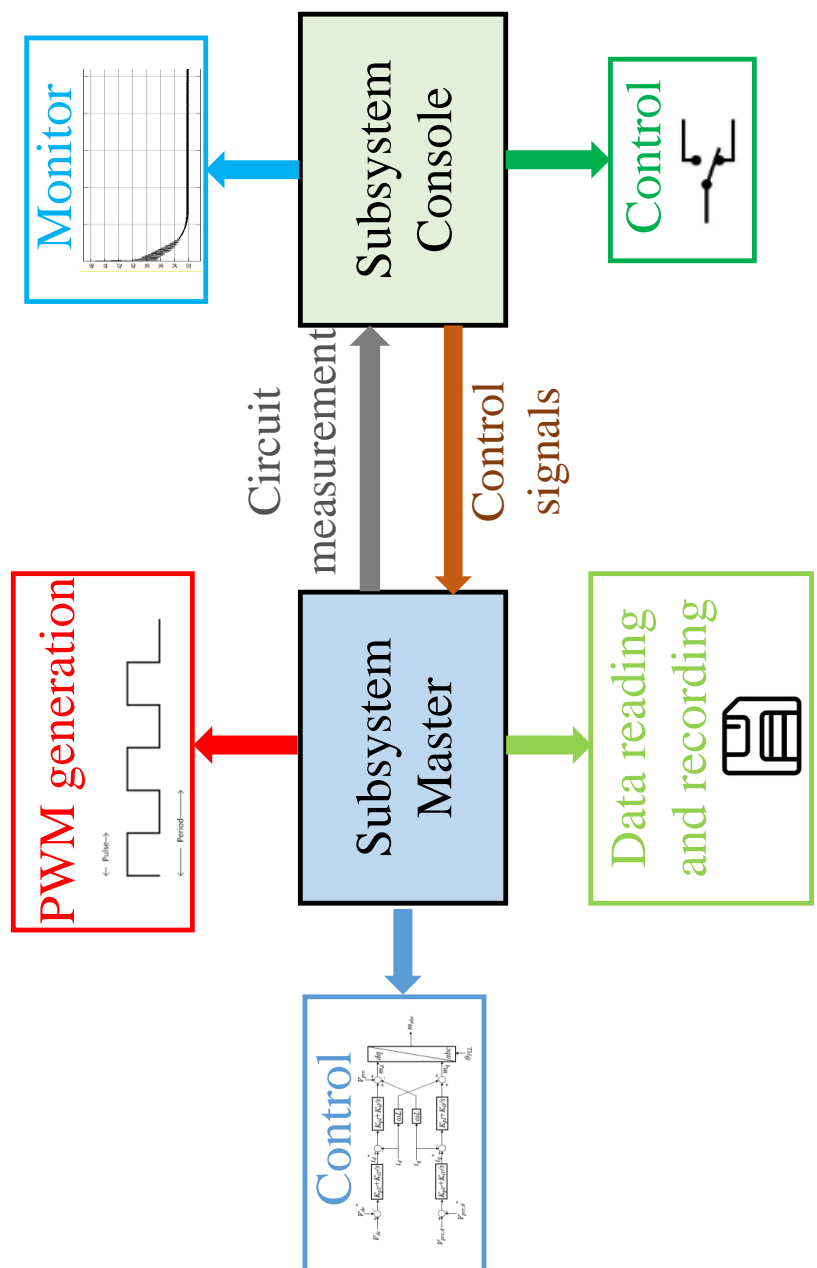


Figure 2.5: RT-Lab model structure.

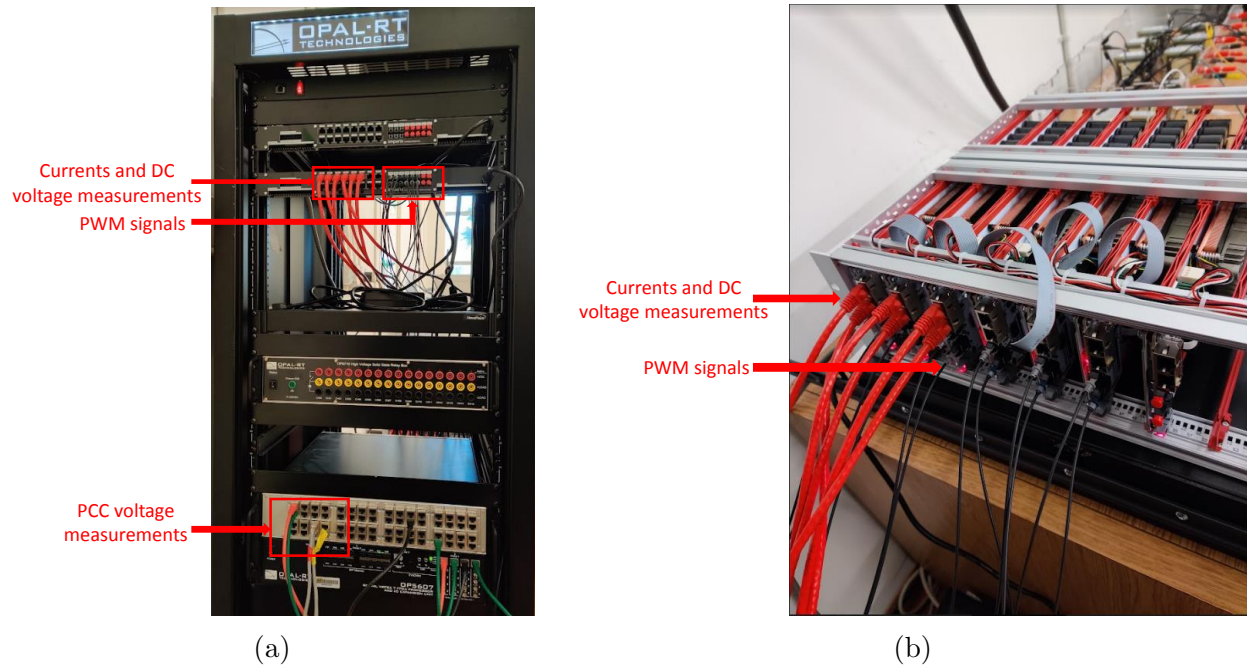


Figure 2.6: RT-Lab and Imperix module connection. (a) Front side of RT-Lab. (b) Imperix module connection for measurements and PWM signals.

in Fig. 2.6. A HIL simulation interface is installed on the top of RT-Lab, its purposes are listed as follows.

- Receive current measurements from Imperix modules through RJ45 connectors, and transfer to RT-Lab.
- Receive PWM signals from RT-Lab, and transfer to Imperix modules through optical fibers.

These devices are summarized and described in detail in Table. 2.1.

Table 2.1: Hardware test bed devices

Device name	Function	Description
Chroma 61845	Grid Emulator	Bidirectional single- or three-phase power supply Max. Power: 45 kVA
OPAL-RT OP5607	Record, generate and process data	16 analog inputs 48 digital outputs
Imperix PEB-8024 Power Module	Three-phase converter	Max. DC voltage: 850 V 1200 V/36 A SiC MOSFETs Max. switching frequency: 200 kHz Current sensor bandwidth: 280 kHz
OPAL-RT OP8662	Voltage Probe	Number of voltage channels: 8 Max. voltage: 600 Hz Bandwidth: 100 kHz
BK Precision 1666	DC voltage source	Max. output : 40 V/5 A
HIL Simulation Interface	Transfer measured and PWM signals	16 analog inputs with RJ45 connector 16 digital outputs with optical fibers

### 2.2.1 Hardware Test Bed Challenge

Benchmarking the computer simulation test bed and the hardware test bed is a time-consuming task. It requires attention to meticulous details. Three lessons have been learned in this process.

- Per-unit calculation for simulation and experiment requires attention. In this research, the grid-following converter control parameters, e.g., current control, outer controls, and PLL, are all in per unit values. This requires that the measurements are all converted to per unit values. In the computer simulation test bed, the per-unit calculation is realized automatically by the three-phase measurement block in the SimPowerSystems model, where the nominal voltage is the line-to-line RMS value as 20 V. On the other hand, in the hardware test bed, real-time three-phase voltage signals are measured and sent to RT-Lab for processing. Per unit calculation is followed. The base for the instantaneous voltage signals is different from the RMS value, rather, the per-phase peak value 16.3 V or  $\sqrt{\frac{2}{3}} \times 20$  V should be used.
- The value of an inductor's inductance should be carefully measured. The inductance has mismatch from the value in an inductor's label. In this research, the inductor's label shows it has inductance of 15 mH at 4 A. According to experimental results and steady-state calculation, the circuit current is about 2 A in this case. Moreover, since the inductance is too large for this system, two inductors are connected in parallel so the transmission line impedance is reduced, which means that the current through each inductor is also changed to half. Under this operation condition, the circuit current is lower than the rated current, this change also influences the inductance value. To find the accurate inductance, the Chroma 61485 grid simulator is connected to the inductor directly and operates at the desired operation condition. By measuring the voltage across the inductor and its current, the inductance can be calculated as about

9.7 mH (parallel connection) when working at this current. This value is then used in simulation for verification.

- PWM signals generation in the hardware test bed needs attention. The hardware test bed employs RT-Lab to implement control algorithm. The output PWM signals are defined by the duty ratio  $d$ , not PWM's modulation index  $m$ . On the other hand, the output of vector control system is the reference voltage  $u_{ref}$ . The equation to convert  $u_{ref}$  to  $d$  is as follows.

$$d = \frac{1}{2}(u_{ref} + 1).$$

### 2.3 Simulation Test Bed

The VSC system shown in Fig. 2.1 is simulated in MATLAB/SimPowerSystems software. Both control system and power circuit components are created using the blocks in the library. The VSC block is an average model, which uses a reference signal  $u_{ref}$  to represent the output terminal voltage  $v_{abc}$ , so the controlled signal of VSC block is a three-phase sinusoidal waveform instead of PWM signal. This model does not contain harmonics and has a faster simulation speed. A switch is used in  $q$ -axis outer loop to choose Q or V control manually. The time step is set as  $25 \mu s$ . Fig. 2.7 shows the simulation model. It should be noticed that the calculation process for P and Q, filter, and  $dq$ -axis decoupled process are not shown.

### 2.4 Admittance-Based Model

The admittance-based model is also implemented to represent the VSC system. Harmonic injection method and analytical model derivation are used to obtain the admittance-based model. The two methods are demonstrated as follows.



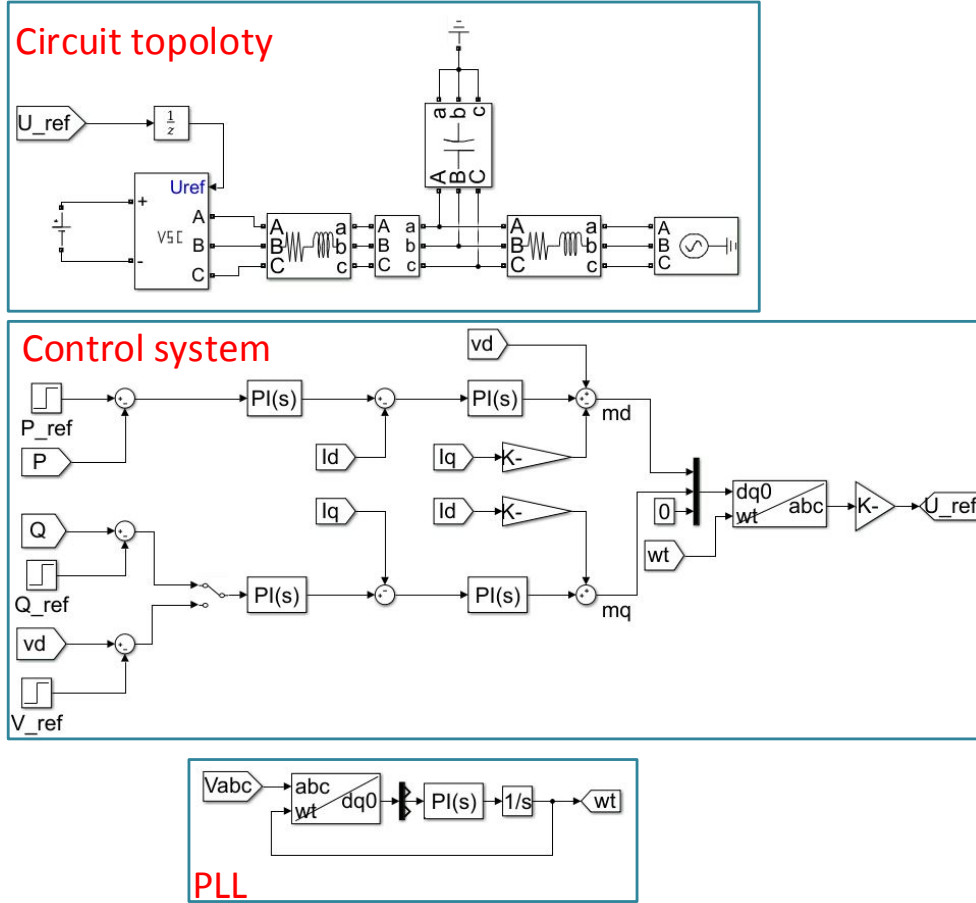


Figure 2.7: Configuration of EMT model.

### 2.4.1 Harmonic Injection Process

For example, harmonic injection is used in obtaining the system impedance in sequence domain by injecting a voltage or current harmonics [37,38]. Through extracting the output distortion and being processed in a range of frequency, the desired impedance model can be built. This method is widely used for analysis of subsynchronous resonance in power plants [39].

The authors in [40] have proposed the converter impedance model in the  $dq$ -domain, which is shown in (2.4). In this system, the voltage or current injection is required to be applied in the synchronous  $dq$ -reference frame. Since most of VSC employ controllers are based on  $dq$ -reference frame, the  $dq$ -domain impedance has a closer relationship with its control system

[41]. Furthermore, the  $dq$ -domain impedance transforms variables such as voltages and currents into DC components, the fundamental component does not impact measurements. Thus, the  $dq$ -domain impedance is applied to implement the harmonic analysis.

$$\begin{bmatrix} V_d(s) \\ V_q(s) \end{bmatrix} = \underbrace{\begin{bmatrix} Z_{dd}(s) & Z_{dq}(s) \\ Z_{qd}(s) & Z_{qq}(s) \end{bmatrix}}_{Z_{ddqq}} \begin{bmatrix} I_d(s) \\ I_q(s) \end{bmatrix} \quad (2.4)$$

where  $Z_{ddqq}$  is a two-by-two complex matrix related to frequency.

And the admittance  $Y_{dq}$  is derived through inverse the  $Z_{dq}$ , and can be expressed in (2.5).

$$\begin{bmatrix} I_d(s) \\ I_q(s) \end{bmatrix} = \underbrace{\begin{bmatrix} Y_{dd}(s) & Y_{dq}(s) \\ Y_{qd}(s) & Y_{qq}(s) \end{bmatrix}}_{Y_{ddqq}} \begin{bmatrix} V_d(s) \\ V_q(s) \end{bmatrix} \quad (2.5)$$

The  $dq$ -frame admittance can be built by injecting a set of voltage perturbation and measure the output current in the  $dq$ -frame. Based on the (2.5), the  $Y_{dd}$  and  $Y_{qd}$  are derived through perturbing  $v_d$  while  $v_q$  keeps zero. Similarly, when the perturbation is injected to  $v_q$  and  $v_d$  is set to zero, the  $Y_{dq}$  and  $Y_{qq}$  are measured. The algorithm is shown in (2.6).

$$\begin{aligned} Y_{dd}(s) &= \frac{I_d(s)}{V_d(s)}, & Y_{qd}(s) &= \frac{I_q(s)}{V_d(s)}, & V_q(s) &= 0 \\ Y_{dq}(s) &= \frac{I_d(s)}{V_q(s)}, & Y_{qq}(s) &= \frac{I_q(s)}{V_q(s)}, & V_d(s) &= 0 \end{aligned} \quad (2.6)$$

Another analysis approach of VSC is the sequence admittance model. It is widely used in stability and harmonic analysis. This model can be represented as positive and negative admittance in (2.7).

$$\begin{bmatrix} I_p(s) \\ I_n(s) \end{bmatrix} = \underbrace{\begin{bmatrix} Y_{pp}(s) & Y_{pn}(s) \\ Y_{np}(s) & Y_{nn}(s) \end{bmatrix}}_{Y_{ppnn}} \begin{bmatrix} V_p(s) \\ V_n(s) \end{bmatrix} \quad (2.7)$$

where subscript  $p$  and  $n$  represent positive and negative sequence, respectively.

According to the double fourier-series theory, when the three-phase VSC is disturbed from its steady-state by a three-phase voltage injection at frequency  $f_1$ , two current harmonic components appear at frequencies  $f_1$  and  $2f_0 - f_1$ , where the  $f_0$  is the fundamental frequency. The sequence domain impedance is calculated from the injected voltage and generated current harmonic components.

For an injected voltage harmonic  $V_p$  at frequency  $\omega_1$ , the  $Y_{pp}$  and  $Y_{np}$  are derived in (2.8).

$$Y_{pp} = \frac{\bar{I}_1}{V_p}, \quad Y_{np} = \frac{\bar{I}_2}{V_p^*} \quad (2.8)$$

where  $\bar{I}_1$  is current harmonic at frequency  $\omega_1$  and  $\bar{I}_2$  at  $2\omega_0 - \omega_1$ .

Then the injected voltage harmonic  $V_n$  frequency changes to  $\omega'_1$ , the  $Y_{pn}$  and  $Y_{nn}$  are derived in (2.9).

$$Y_{pn} = \frac{\bar{I}'_2}{V_n^*}, \quad Y_{nn} = \frac{\bar{I}'_1}{V_n} \quad (2.9)$$

where  $\omega'_1 = 2\omega_0 - \omega_1$ ,  $\bar{I}'_2$  is current harmonic at frequency  $\omega_1$  and  $\bar{I}'_1$  at  $\omega'_1$ .

The relation of  $dq$ -domain and sequence admittance is given in (2.10).

$$\begin{bmatrix} Y_{dd} & Y_{dq} \\ Y_{qd} & Y_{qq} \end{bmatrix} = \frac{1}{2} \begin{bmatrix} 1 & 1 \\ -j & j \end{bmatrix} \begin{bmatrix} Y_{pp} & Y_{pn} \\ Y_{np}^* & Y_{nn}^* \end{bmatrix} \begin{bmatrix} 1 & j \\ 1 & -j \end{bmatrix} \quad (2.10)$$

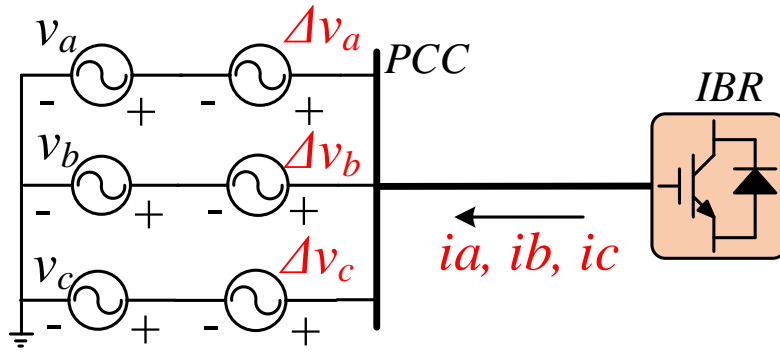
It should be noted that if the  $\omega_1$  is larger than  $2\omega_0$ , the  $\omega'_1$  will be negative. An injected voltage with negative frequency means the voltage is negative sequence, where phase b leading phase a by  $120^\circ$  and lagging phase c by  $120^\circ$ .

In order to derive the impedance model of the VSC system, a three-phase voltage harmonic is injected to the system [42]. By obtaining the current and voltage phasor at desired frequency through FFT analysis, positive and negative admittance are calculated by (2.8) and (2.9). Then the  $dq$ -domain admittance can be transformed from the sequence admittance. The system is shown in Fig 2.8a. In  $dq$  injection approach, the voltage source is decomposed into  $dq$ -reference frame. A perturbation is injected into d-axis voltage while q-axis voltage has no injection, and vice versa. Converting three-phase current into  $dq$ -reference frame and related to injected voltage, the  $dq$ -domain impedance also can be derived. This method is shown in Fig. 2.8b. In this chapter, only  $dq$  injection approach will be implemented.

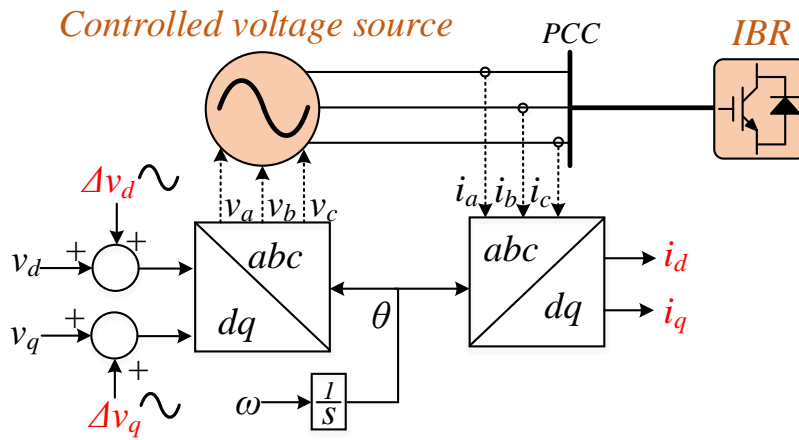
The harmonic injection technique is employed to measure the admittance frequency-domain responses. The currents and voltages in  $dq$ -domain are recorded after injecting a small-signal perturbation at the terminal. The obtained data are used to calculate admittance model.

As Fig. 2.8b shows, the controllable voltage source is connected to the wind farm at the interconnection point of 220 kV. Two perturbation voltages are superimposed into the voltage source, respectively.

The voltages are defined in the  $dq$ -frame and converted to the  $abc$ -frame to form a three-phase voltage source. The resulting currents are recorded at the PCC bus. They are converted to  $dq$ -frame variables  $i_{dq}$ . Fast Fourier transform (FFT) is implemented to extract the phasor form of  $v_{dq}$  and  $i_{dq}$  at the frequency of the injected perturbation. It should be noted that the injected perturbation needs to be small enough so it has no influence on the system operation.



(a)



(b)

Figure 2.8: Block diagram of injection system. (a) Three-phase voltage injection. (b) dq-voltage injection.

The admittance at every frequency point is calculated in (2.11).

$$\begin{aligned} Y_{dd}(f_i) &= \frac{i_d^{(1)}(f_i)}{v_d^{(1)}(f_i)}, & Y_{dq}(f_i) &= \frac{i_d^{(2)}(f_i)}{v_q^{(2)}(f_i)} \\ Y_{qd}(f_i) &= \frac{i_q^{(1)}(f_i)}{v_d^{(1)}(f_i)}, & Y_{qq}(f_i) &= \frac{i_q^{(2)}(f_i)}{v_q^{(2)}(f_i)} \end{aligned} \quad (2.11)$$

where superscripts (1) and (2) are related to voltage perturbation in  $d$ - and  $q$ -axes, respectively;  $f_i$  is the injected frequency.

Similarly, a real, reactive power vs. terminal voltage phasor (PQ/V $\theta$ ) model is built to represent the relationship of power and voltage phasor, can be expressed in (2.12).

$$\begin{bmatrix} P(s) \\ Q(s) \end{bmatrix} = \underbrace{\begin{bmatrix} G_{11}(s) & G_{12}(s) \\ G_{21}(s) & G_{22}(s) \end{bmatrix}}_{G_{PV}} \begin{bmatrix} V(s) \\ \theta(s) \end{bmatrix} \quad (2.12)$$

The configuration of injection system for PQ/V $\theta$  model is shown in Fig. 2.9.

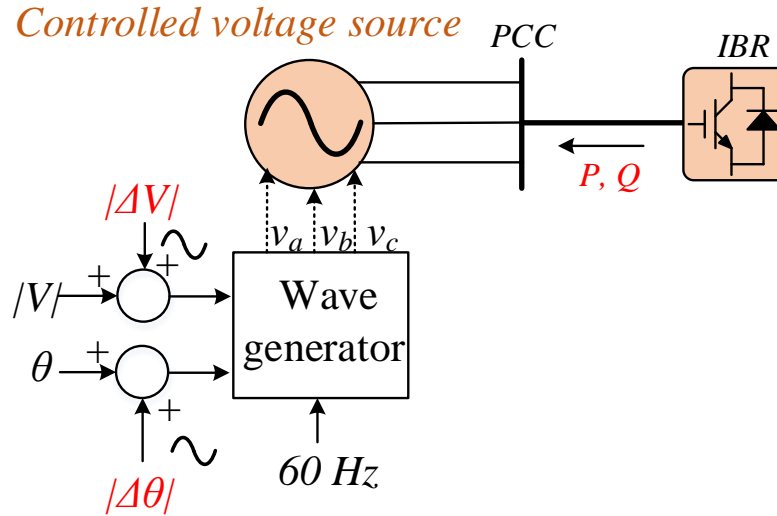


Figure 2.9: Block diagram of PQ/V $\theta$  injection system.

This model is calculated as follows.

$$\begin{aligned} G_{11}(f_i) &= \frac{P^{(1)}(f_i)}{V^{(1)}(f_i)}, & G_{12}(f_i) &= \frac{P^{(2)}(f_i)}{\theta^{(2)}(f_i)} \\ G_{12}(f_i) &= \frac{Q^{(1)}(f_i)}{V^{(1)}(f_i)}, & G_{22}(f_i) &= \frac{Q^{(2)}(f_i)}{\theta^{(2)}(f_i)} \end{aligned} \quad (2.13)$$

where superscripts (1) and (2) are related to voltage perturbation in  $V$  and  $\theta$ , respectively.

#### 2.4.1.1 Harmonic Injection in MATLAB Test Bed

An example system used for harmonic injection in MATLAB test bed is shown in Fig. 2.10. A three-phase grid voltage source is replaced by three controlled voltage sources to represent  $v_a$ ,  $v_b$ , and  $v_c$ , separately. The three voltage signals are generated from dq/abc transformation, and two signals are superimposed to  $dq$ -input. Three-phase current  $I_{abc}$  is converted to  $dq$ -frame  $I_d$  and  $I_q$ .

For each injected frequency,  $d$ - and  $q$ -axis harmonic are imposed separately. Thus, only one column of  $dq$ -domain admittance can be obtained for each injection process. The frequency is preset in MATLAB script. A loop is used in MATLAB script to run the simulation test bed. Fig. 2.12 shows the harmonic injection results.

#### 2.4.1.2 Harmonic Injection with MATLAB Script

Harmonic injection may have accurate results for admittance model, but it's time consuming and requires lots of coding work. Another method is applied using a MATLAB tool. The process is demonstrated as follows.

As shown in Fig. 2.10, the block name of  $d$ -axis injected signal is 'Sine Wave1', the  $q$ -axis is 'Sine Wave2', while output currents  $I_d$  and  $I_q$  are from block 'Demux5'. So the inputs and outputs are defined as follows.

```
%Define input ports
io(1)=linio('TestSystem/Sine Wave1',1,'input');
```

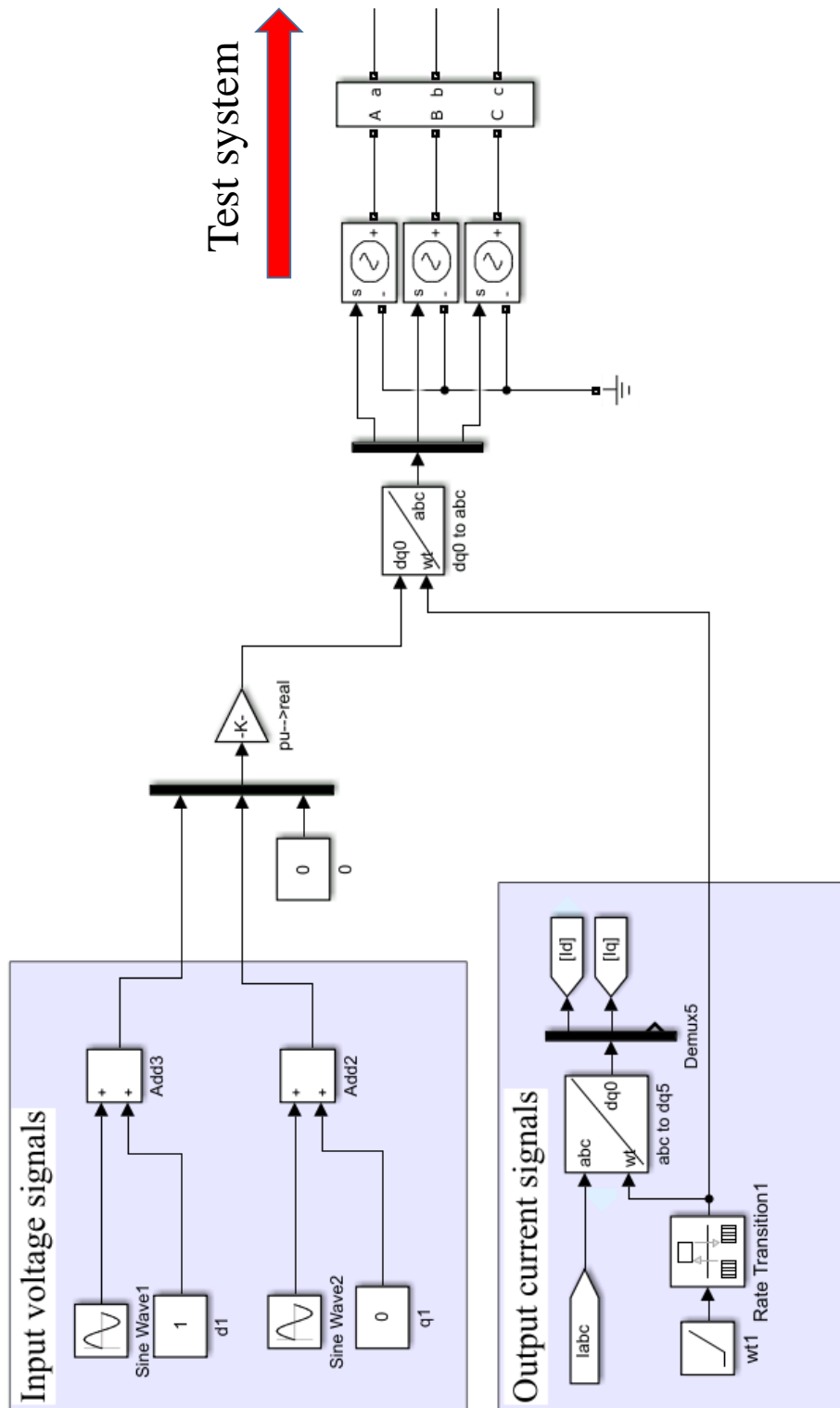


Figure 2.10: Model setup for harmonic injection.



```
io(2)=linio('TestSystem/Sine Wave2',1,'input');
```

```
%Define output ports
```

```
io(3)=linio('TestSystem/Demux5',1,'output');
```

```
io(4)=linio('TestSystem/Demux5',2,'output');
```

A MATLAB command '*frest.createFixedTsSinestream*' is used to generate sinusoidal waveform continuously. If the step size of system is  $50 \mu s$ , and injected frequency ranges from 1 Hz to 200 Hz, magnitude is 0.1, then the waveform is defined as follows.

```
%Define injected signals
```

```
input = frest.createFixedTsSinestream(5e-5,{2*pi*1 2*pi*200});
```

```
input.Amplitude=0.1;
```

The injected signals are shown in Fig. 2.11. It can be seen that d- and q-axis voltage perturbation signals are injected separately. There are only four periods for each injected frequency.

Last, the frequency response estimation are achieved as follows.

```
%Start injection
```

```
model = 'TestSystem';
```

```
syssest = frestimate(model,io,input);
```

Fig. 2.12 shows the comparison of harmonic injection and MATLAB command '*frest*' in a test system. For harmonic injection, the injected frequency is from 1 Hz to 200 Hz, and interval is 1 Hz. For '*frest*' command, 30 frequencies logarithmically spaced between 1 Hz to 200 Hz. Compared with harmonic injection method, '*frest*' is easier to implement, but only 30 frequencies are swept.

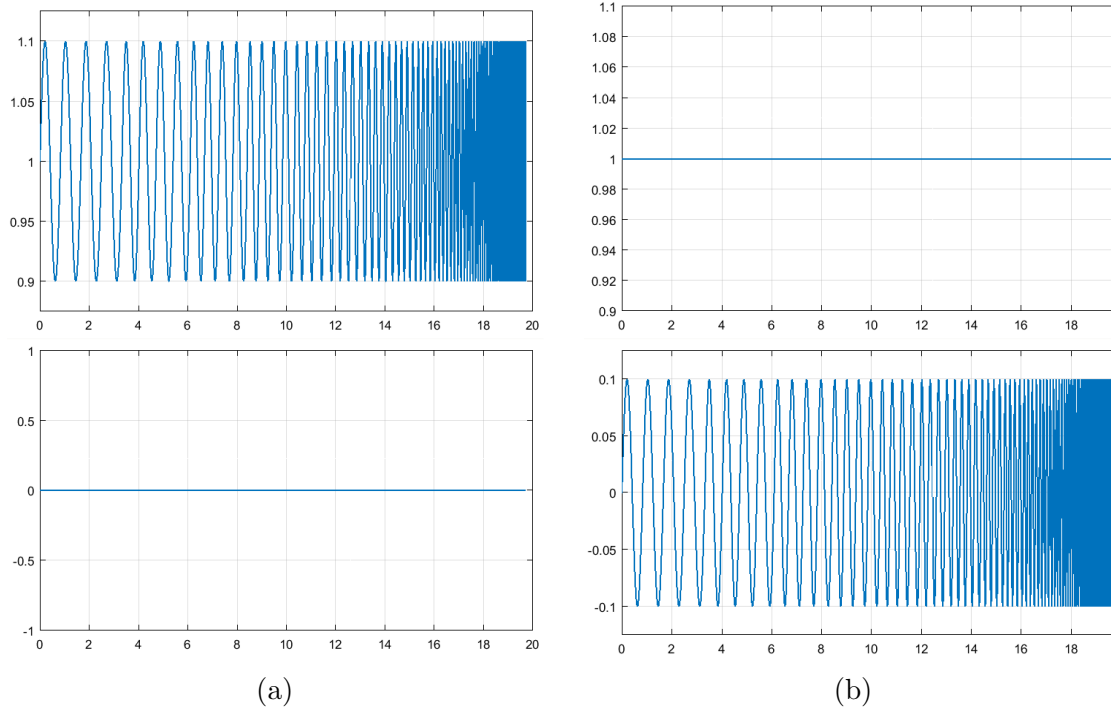


Figure 2.11: Dq-axis injected signals. (a) D-axis voltage. (b) Q-axis voltage.

### 2.4.1.3 Harmonic Injection in PSCAD

For a MATLAB/SimPowerSystems model, MATLAB script '*sim*' is able to run the target model repeatedly. The model's parameters are initialized in MATLAB 'InitFcn', and data will be saved and processed with each injected frequency. In PSCAD model, Python script is used to call PSCAD model, and data is saved as *.cfg* file. Then the data is read and processed by MATLAB script. The injection procedure is demonstrated as follows.

Fig. 2.13 shows a grid-connected Type-4 wind farm in PSCAD model, where grid is replaced by a controlled three-phase voltage source.

Fig. 2.14 shows the blocks of *dq*-transformation and injected signals generation. The controlled voltage source's signals are  $v_{ma}$ ,  $v_{mb}$ , and  $v_{mc}$ , which is converted from *dq*-frame transformation.  $v_d$  and  $v_q$  are sum of a constant value and a small disturbance. The two disturbances are generated from '*Sin*' block, where phase is zero, magnitude is a relatively small value, usually less than 10% of nominal voltage, frequency is the controlled variable in Python loop programming, and a switch is used to start the injection.

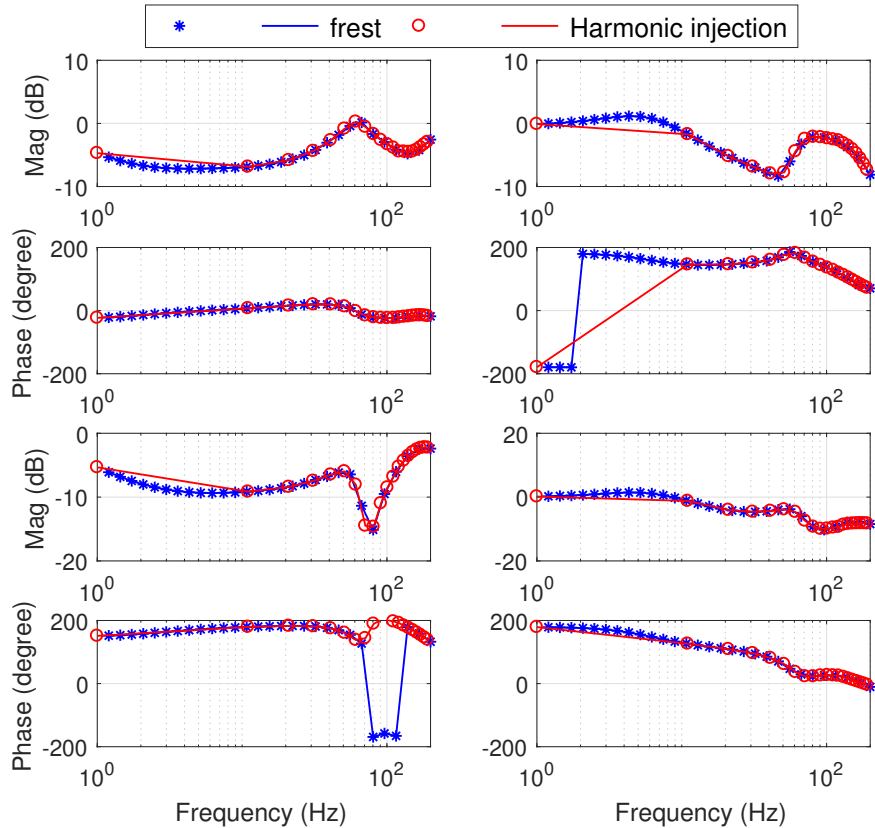


Figure 2.12: Admittance comparison of harmonic injection and frest.

In PSACD model, each component has a unique identifier number. By right clicking the component and this identifier number can be found in the attribute bar. Fig. 2.15 shows the identifier number for d- and q-axis harmonic signals in red box.

After running this model, data of  $v_{dq}$  and  $i_{dq}$  are saved through RTP/COMTRADE Recorder. And the identifier name for data name is also found in Fig. 2.16.

With the known identifier numbers of these variables, the injection process can be started. Firstly, Python compiler will search for the project name in the working directory.

```
project_name = 'Type4_RLC_SSR_short_dq'
# Source and destination folders for output data
src_folder = working_dir + project_name + fortran_ext
dst_folder = working_dir + "dinj_output"
```

Then define the  $dq$ -frame injected signals and saved date file name.



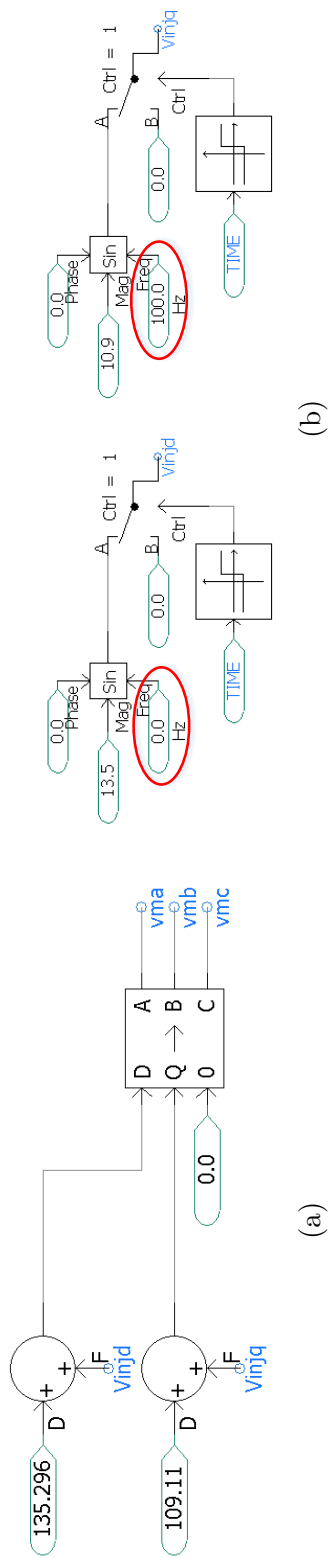
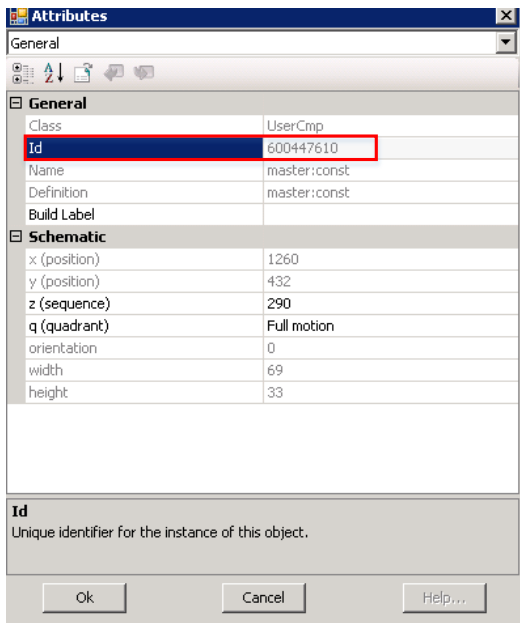
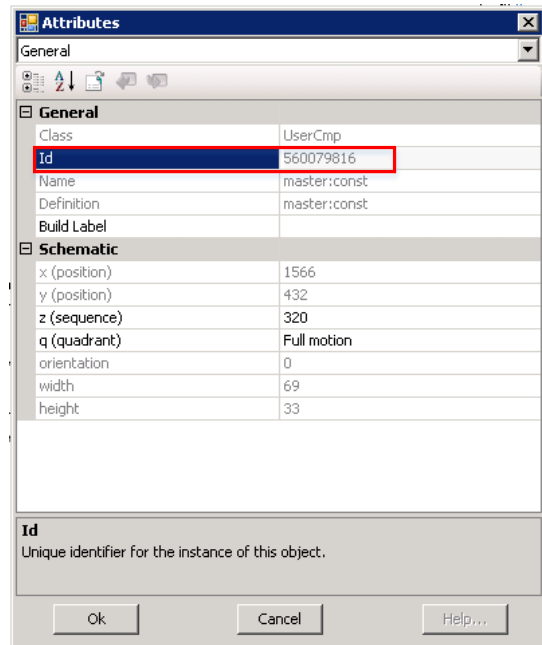


Figure 2.14: (a) Three-phase voltage signals generation. (b) Injected harmonic signals generation.

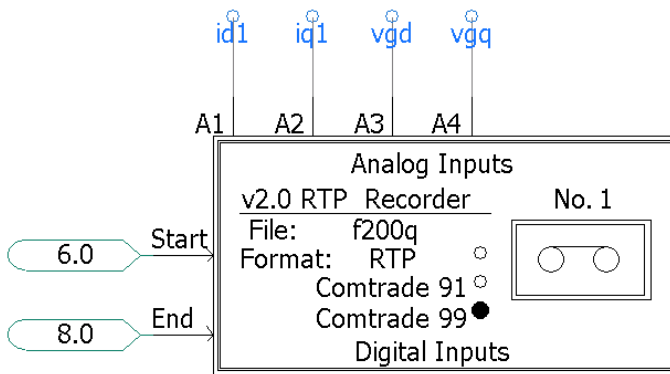


(a)

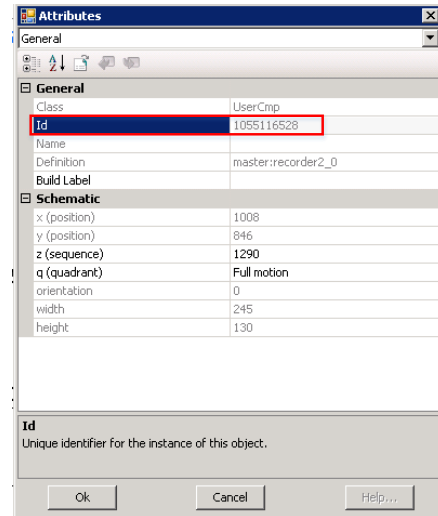


(b)

Figure 2.15: Identifier number for (a) d-axis voltage harmonic signal. (b) q-axis voltage harmonic signal.



(a)



(b)

Figure 2.16: (a) RTP/COMTRADE Recorder block. (b) Identifier number of saved data file.

```

freq_injd = main.user_cmp(600447610)
freq_injq = main.user_cmp(560079816)
data_log = main.user_cmp(1055116528)

```

Next step is to setup the loop parameters. If injection frequency is from 1 Hz to 100 Hz, then PSCAD model will run 200 times. The first 100 times are d-axis injection and rests 100 are q-axis injection. Data generated from each loop are also defined. The code for loop and name define are posted as follows.

```

j=1
while j<201:
    if j<101:
        freq_injd.set_parameters(Value=j)
        freq_injq.set_parameters(Value=0)
        data_log.set_parameters(FName="f"+str(j)+"d")
        project.run()
    else:
        freq_injd.set_parameters(Value=0)
        freq_injq.set_parameters(Value=j-100)
        data_log.set_parameters(FName="f"+str(j)+"q")
        project.run()
    j+=1

```

After the injection process finished, all data will be saved in a folder, as shown in Fig. 2.17.

Each file represents a *d*- or *q*-axis injected voltage for this model. And program code for the COMTRADE reader is used to extract the data and calculate the admittance.

Fig. 2.18 shows the flowchart for harmonic injection in a PSCAD model.

Name	Date modified ^	Type	Size
f1d.cfg	3/31/2021 8:35 PM	CFG File	1 KB
f1d	3/31/2021 8:35 PM	Data File in DAT For...	1,993 KB
f1d.hdr	3/31/2021 8:35 PM	HDR File	1 KB
f2d.cfg	3/31/2021 8:35 PM	CFG File	1 KB
f2d	3/31/2021 8:35 PM	Data File in DAT For...	1,993 KB
f2d.hdr	3/31/2021 8:35 PM	HDR File	1 KB
f3d.cfg	3/31/2021 8:36 PM	CFG File	1 KB
f3d	3/31/2021 8:36 PM	Data File in DAT For...	1,993 KB
f3d.hdr	3/31/2021 8:36 PM	HDR File	1 KB
f4d.cfg	3/31/2021 8:36 PM	CFG File	1 KB
f4d	3/31/2021 8:36 PM	Data File in DAT For...	1,993 KB
f4d.hdr	3/31/2021 8:36 PM	HDR File	1 KB
f5d.cfg	3/31/2021 8:37 PM	CFG File	1 KB
f5d	3/31/2021 8:37 PM	Data File in DAT For...	1,993 KB
f5d.hdr	3/31/2021 8:37 PM	HDR File	1 KB
f6d.cfg	3/31/2021 8:37 PM	CFG File	1 KB
f6d.hdr	3/31/2021 8:37 PM	HDR File	1 KB
f6d	3/31/2021 8:37 PM	Data File in DAT For...	1,993 KB
f7d.cfg	3/31/2021 8:37 PM	CFG File	1 KB
f7d.hdr	3/31/2021 8:37 PM	HDR File	1 KB
f7d	3/31/2021 8:37 PM	Data File in DAT For...	1,993 KB
f8d.cfg	3/31/2021 8:38 PM	CFG File	1 KB
f8d	3/31/2021 8:38 PM	Data File in DAT For...	1,993 KB
f8d.hdr	3/31/2021 8:38 PM	HDR File	1 KB
f9d.cfg	3/31/2021 8:39 PM	CFG File	1 KB
f9d.hdr	3/31/2021 8:39 PM	HDR File	1 KB
f9d	3/31/2021 8:39 PM	Data File in DAT For...	1,993 KB
f10d.cfg	3/31/2021 8:39 PM	CFG File	1 KB
f10d	3/31/2021 8:39 PM	Data File in DAT For...	1,993 KB
f10d.hdr	3/31/2021 8:39 PM	HDR File	1 KB
f11d.cfg	3/31/2021 8:40 PM	CFG File	1 KB
f11d	3/31/2021 8:40 PM	Data File in DAT For...	1,993 KB

Figure 2.17: PSCAD harmonic injection data in folder.

## 2.4.2 Analytical Model

An analytical model is built to reflect the three-phase VSC system, which includes outer loop control, inner loop control, PLL, and grid dynamics. The system is operated in  $dq$ -



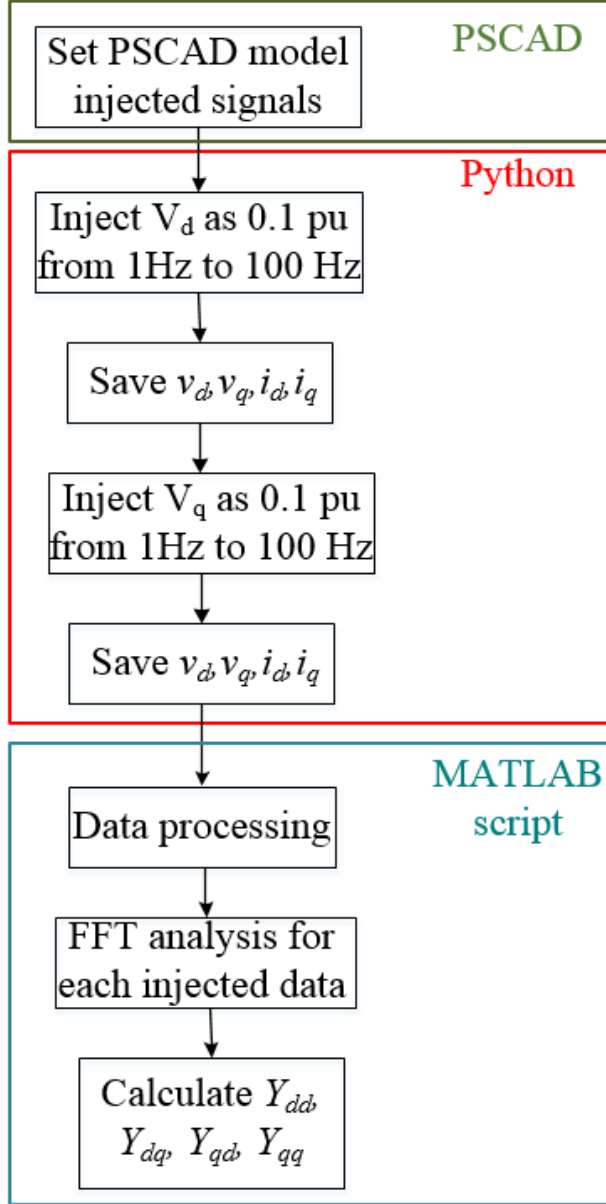


Figure 2.18: Flowchart for harmonic injection in PSCAD model.

frame, thus, all variable are constant at steady state. Compared with EMT detailed model, the grid dynamics are represented as a series of differential equations as follows.

$$\begin{aligned}
 L_1 \frac{d\vec{i}_1}{dt} + R_1 \vec{i}_1 &= \vec{V}_1 - \vec{V}_{pcc} \\
 L_g \frac{d\vec{i}_2}{dt} + R_g \vec{i}_g &= \vec{V}_{pcc} - \vec{V}_g \\
 C_f \frac{d\vec{V}_{pcc}}{dt} &= \vec{i}_1 - \vec{i}_g
 \end{aligned} \tag{2.14}$$

The current space vector can be transformed to  $dq$ -frame in (2.15):

$$\vec{i}_1 = (i_d + ji_q)e^{\varepsilon(t)} \quad (2.15)$$

where  $\varepsilon(t) = j\omega_0 t + \theta_0$ .

Similarly, substituting other variables in (2.14) by  $dq$ -components, we can deduce the differential equations in  $dq$ -frame.

$$\begin{aligned} \frac{di_{1d}}{dt} &= \frac{1}{L_1}(v_d - v_{pcc,d} - R_1 i_{1d} + \omega_0 L_1 i_{1q}) \\ \frac{di_{1q}}{dt} &= \frac{1}{L_1}(v_q - v_{pcc,q} - R_1 i_{1q} - \omega_0 L_1 i_{1d}) \\ \frac{di_{2d}}{dt} &= \frac{1}{L_2}(v_{pcc,d} - v_g - R_g i_{2d} + \omega_0 L_g i_{2q}) \\ \frac{di_{2q}}{dt} &= \frac{1}{L_2}(v_{pcc,q} - R_g i_{2q} - \omega_0 L_g i_{2d}) \\ \frac{dv_{pcc,d}}{dt} &= \frac{1}{C_f}(i_{1d} - i_{2d} + \omega_0 C_f v_{pcc,q}) \\ \frac{dv_{pcc,q}}{dt} &= \frac{1}{C_f}(i_{1q} - i_{2q} - \omega_0 C_f v_{pcc,d}) \end{aligned} \quad (2.16)$$

Fig. 2.19 shows the analytical model, the control loops and PLL are well illustrated in previous descriptions. In this model,  $\dot{x} = [\frac{di_{1d}}{dt}; \frac{di_{1q}}{dt}; \frac{di_{2d}}{dt}; \frac{di_{2q}}{dt}; \frac{dv_{pcc,d}}{dt}; \frac{dv_{pcc,q}}{dt}]$ .

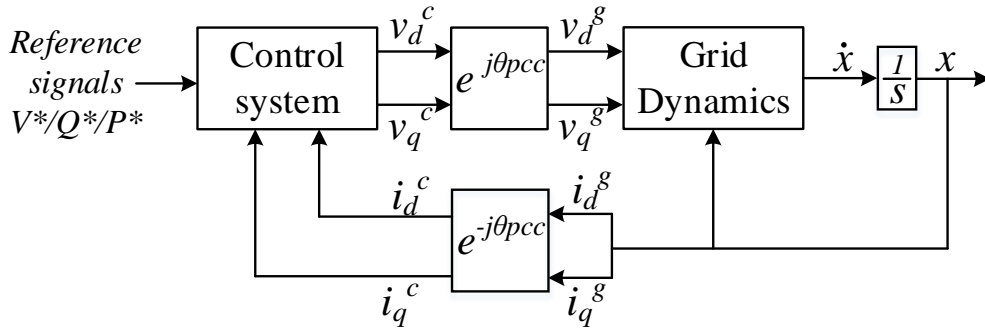


Figure 2.19: Configuration of analytical model.

It should be mentioned that the  $dq$ -frame in this model has two reference frames as converter frame (denoted by superscript ' $c$ ') and grid frame (denoted by superscript ' $g$ ').

Thus, the transformation of the two reference frames require the angle of PCC voltage ( $\theta_{pcc}$ ), which is tracked by PLL to synchronize the converter voltage with grid voltage. The relationship between the  $dq$ -frame voltage and current in converter frame with grid frame is expressed in (2.17).

$$\begin{aligned} v_d^c + jv_q^c &= (v_d^g + jv_q^g)e^{j\theta_{pcc}} = (v_d^g + jv_q^g)(\cos \theta_{pcc} + j \sin \theta_{pcc}) \\ i_d^g + ji_q^g &= (i_d^c + ji_q^c)e^{-j\theta_{pcc}} = (i_d^c + ji_q^c)(\cos \theta_{pcc} - j \sin \theta_{pcc}) \end{aligned} \quad (2.17)$$

#### 2.4.2.1 Eigenvalue Analysis

This model is a twelfth-order system, where six state variables are related to grid dynamics, four state variables are related to control system and two related to PLL. Each state variable is required to be linearized to compute a linear state-space model. Since this model is built in MATLAB/Simulink with ordinary differential equations, the linear model can be found through a command '*linmod*'. The obtained state-space model is shown as in (2.18).

$$\begin{aligned} \dot{x} &= Ax + Bu \\ y &= Cx + Du \end{aligned} \quad (2.18)$$

where  $A, B, C, D$  describe the linearize input-output relationship. If input and output are not specified,  $B, C, D$  are zero.

With matrix  $A$ , eigenvalues of the system can be calculate by another command *eig*( $A$ ).

#### 2.4.2.2 Bode Response Model

Bode response is to describe the gain and phase of a system with a function of frequency graphically. Magnitude and phase angle are presented on separately windows, where x-axis is logarithmic frequency scale and y-axis is represented as  $20\log_{10}[A(\omega)]$  [43]. Inputs and outputs of the model are defined by '*inport*' and '*outport*' blocks in Simulink model.

The Bode plot is obtained in MATLAB in the following step. (1) Build a model with integrator  $\frac{1}{s}$  in Simulink environment and specify inputs and outputs. (2) Calculate the linear model with transfer function, and (3) plot the Bode diagram.

In this work, the response models will be used for stability analysis.

## 2.5 System Parameters

The circuit parameters are listed in Table. 2.2.

Table 2.2: Parameters of the circuit

Description	Parameters	Values
Power base	$S_b$	50 W (1 pu)
System frequency	$f$	60 Hz
Voltage base (L-L RMS)	$V_b$	20 V (1 pu)
Grid voltage (Phase RMS)	$V_s$	11.5 V
DC voltage	$V_{dc}$	40 V
Switching frequency	$f_s$	5 kHz
Converter filter	$R_1$	0.27 Ohm (0.034 pu)
	$L_1 (X_1)$	1.5 mH (0.0707 pu)
Transmission line	$R_g$	0.76 Ohm (0.09 pu)
	$L_g (X_g)$	9.7 mH (0.46 pu)
PLL	$k_{pPLL}, k_{iPLL}$	60, 1400

The parameters of control system are listed in Table 2.3, two groups of parameters with different bandwidth will be investigated.

Table 2.3: Parameters of the controller

	Control loop	Parameters
Parameters I	Current control	$k_{pi}=1, k_{ii}=10$
	P control	$k_{pp}=0.25, k_{ip}=25$
	Q or V control	$k_{pq}=0.25, k_{iq}=25$
Parameters II	Current control	$k_{pi}=0.4758, k_{ii}=3.28$
	P control	$k_{pp}=1.1, k_{ip}=137.5$
	Q or V control	$k_{pq}=0.25, k_{iq}=25$

## Chapter 3: Investigation of Weak Grid Oscillations

### 3.1 Introduction

<sup>1</sup>In order to investigate the oscillation characteristics, four case studies are presented. All case studies are first conducted in the hardware test bed, then benchmarked in the simulation test bed. Different control strategies and parameters are examined and compared. For each case, active power is given a step change to reach marginal stability condition. P, Q from VSC and PCC bus V are presented. The experimental data are collected from RT-Lab and plotted by MATLAB. Both simulations and hardware experiments have the same parameters. Results from two models are compared for verification.

### 3.2 P/Q Control with Parameters I

In this case, the VSC is operated in P/Q control mode with parameters listed in TABLE 2.3. Both experimental model and simulation are working at steady-state when P is set as 1.65 pu.

Fig. 3.1 shows the P, Q from VSC and PCC bus voltage. The Q is regulated as 0.2 pu, and when P increased to 1.68 pu, the experimental model is collapsed, while the limit is 1.7 pu for simulation model.

Before the step change of P, the PCC bus voltages are 1 pu for both models, which demonstrates a good agreement.

---

<sup>1</sup>This chapter was published in IEEE 2021 North American Power Symposium (NAPS) [44]. Permission is included in Appendix A

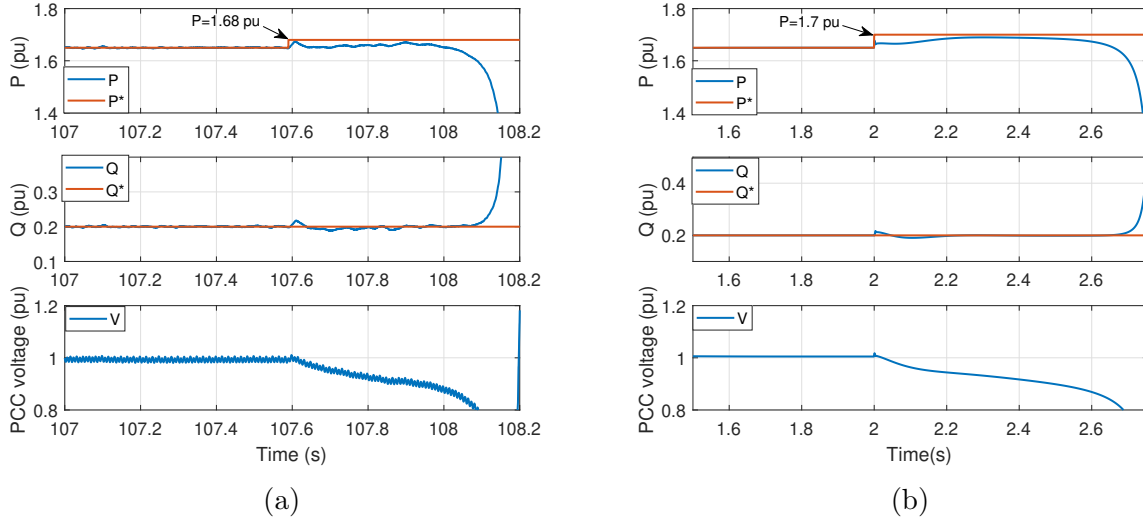


Figure 3.1: Response of  $P$ ,  $Q$  and PCC voltage under  $P/Q$  control with Parameters I when  $P$  is given a step change from 1.65 pu. (a) Experimental results. (b) Simulation results.

### 3.3 $P/Q$ Control with Parameters II

In previous case, the system is collapsed without any oscillation when  $P$  increases to marginal stability condition. But, the oscillation can be observed with specific control parameters. Fig. 3.2 shows the oscillation when the system becomes unstable.

In this case,  $Q$  is still controlled as 0.2 pu, and  $P$  is 1.58 pu at steady-state. When  $P$  is increased to 1.61 pu in experimental model, an undamped 3 Hz oscillation appears. In simulation model, a 3 Hz oscillation is also observed when  $P$  increases to 1.65 pu. At steady-state, since  $P$  and  $Q$  are controlled at the same level, PCC voltages of the two models are compared and found to be same as 1.05 pu.

### 3.4 $P/V$ Control with Parameters I

Under the  $P/V$  control, the PCC voltage is kept as 1 pu. The dynamic responses are shown in Fig. 3.3. The initial value of power is 1.92 pu for both models. It can be seen that when  $P$  reaches 1.94 pu, the experimental model becomes unstable and the frequency of

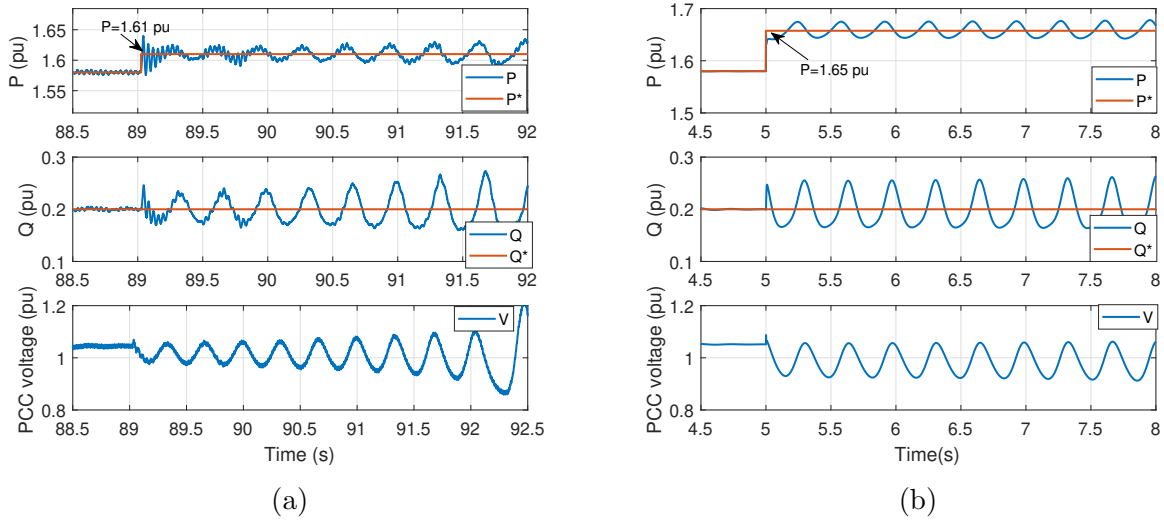


Figure 3.2: Response of P, Q and PCC voltage under P/Q control with Parameters II when P is given a step change from 1.58 pu. (a) Experimental results. (b) Simulation results.

oscillation is 2.8 Hz. In simulation model, a 2.8 Hz oscillation also appears when P changes to 1.97 pu.

At steady-state before step change, the reactive power for both models are 0.42 pu.

### 3.5 P/V Control with Parameter II

In this case, the VSC applies P/V control with the Parameters II. The results are shown in Fig. 3.4. P has a step change from 1.53 pu, and V is kept as 1 pu. Experimental model has a 3.3 Hz oscillation when P increases to 1.57 pu. In simulation model, the limit is 1.59 pu, and the oscillation frequency is also around 3.3 Hz. Before the step change, the Q in two models are about 0.19 pu.

### 3.6 Analytical Model Validation

The validation of analytical model are in two aspects: 1) steady-state operation condition, and 2) marginal stability condition. Fig. 3.5 shows the steady-state values of real power, reactive power and PCC voltage under P/V and P/Q control. P reference is increased so

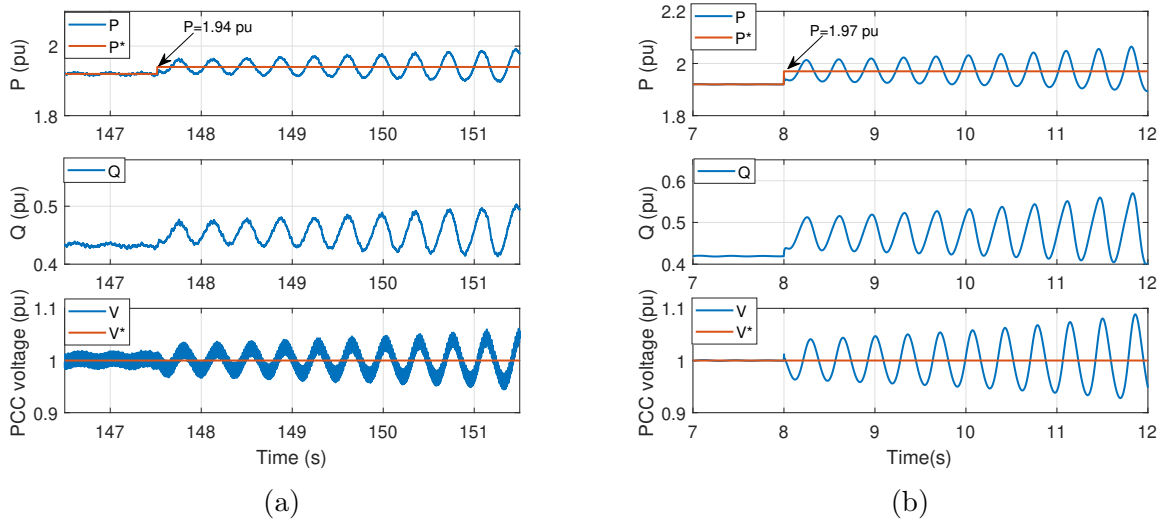


Figure 3.3: Response of P, Q and PCC voltage under P/V control with Parameters I when P is given a step change from 1.92 pu. (a) Experimental results. (b) Simulation results.

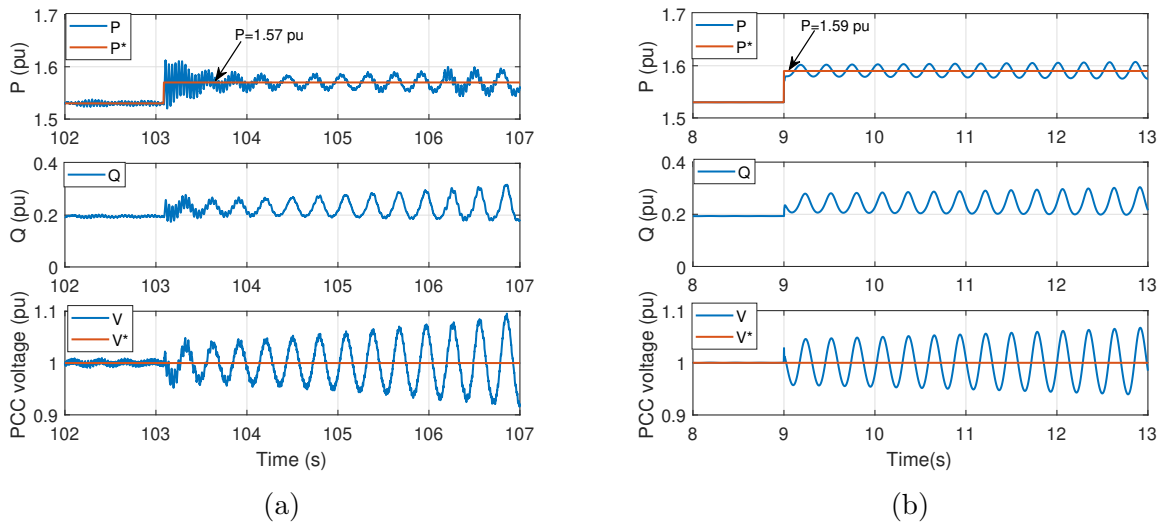


Figure 3.4: Response of P, Q and PCC voltage under P/V control with Parameters II when P is given a step change from 1.53 pu. (a) Experimental results. (b) Simulation results.



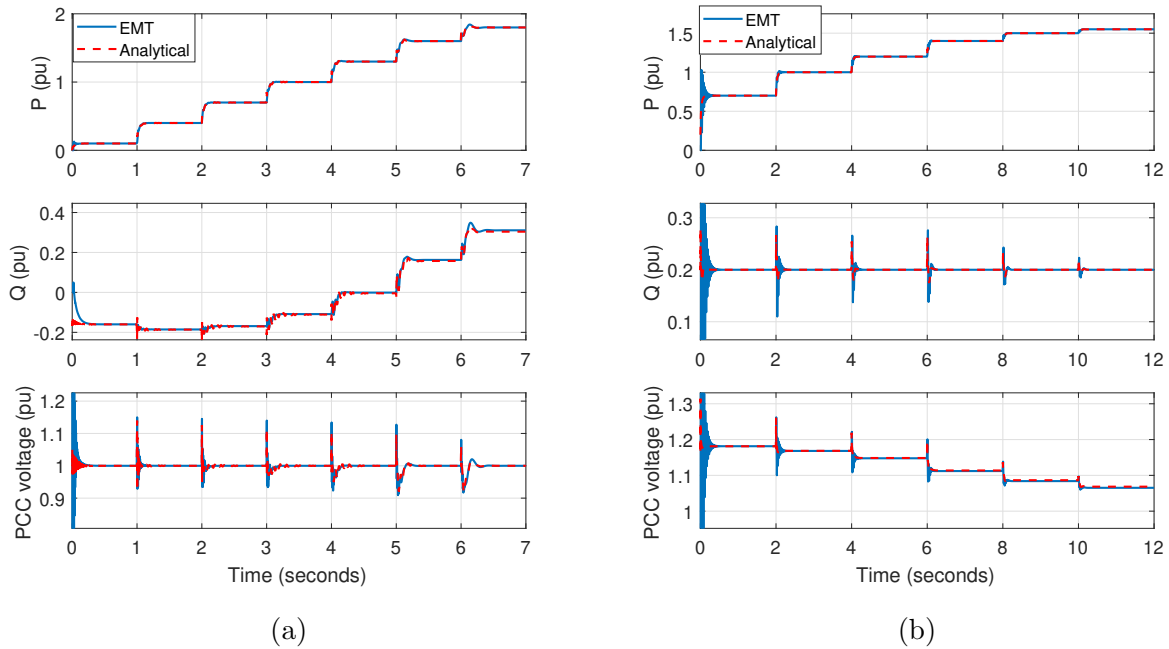


Figure 3.5: Steady-state operation condition comparison of EMT model and analytical model under (a) P/V control, (b) P/Q control.

different operation conditions can be compared. The highly similarity of the steady-state values illustrates the accuracy of analytical model.

Next, marginal stability condition is examined. A MATLAB command *'linmod'* is able to obtain the state-space linear model of the analytical model, and the eigenvalues of *'A'* matrix are also the eigenvalues of system. Fig. 3.6 shows the eigen loci of the four cases with increasing  $P$ . For P/Q control with parameters I, there is no oscillation in EMT simulation when  $P$  increase to 1.68 pu. In this eigen loci analysis, the power limit is  $P=1.68$  pu, if  $P$  continues to increase, then there is no solution for the analytical model's differential equations. For P/Q control with parameters II, an eigenvalue crosses imaginary axis when  $P$  is 1.68 pu, and frequency is about 3 Hz. For P/V control with parameter I, the marginal stability is  $P=1.98$  pu, oscillation frequency is about 2.8 Hz. For P/V control with parameter II, limit  $P$  is 1.66 pu, and frequency is around 3.3 Hz. These analytical analysis is very close to the simulation or hardware results.

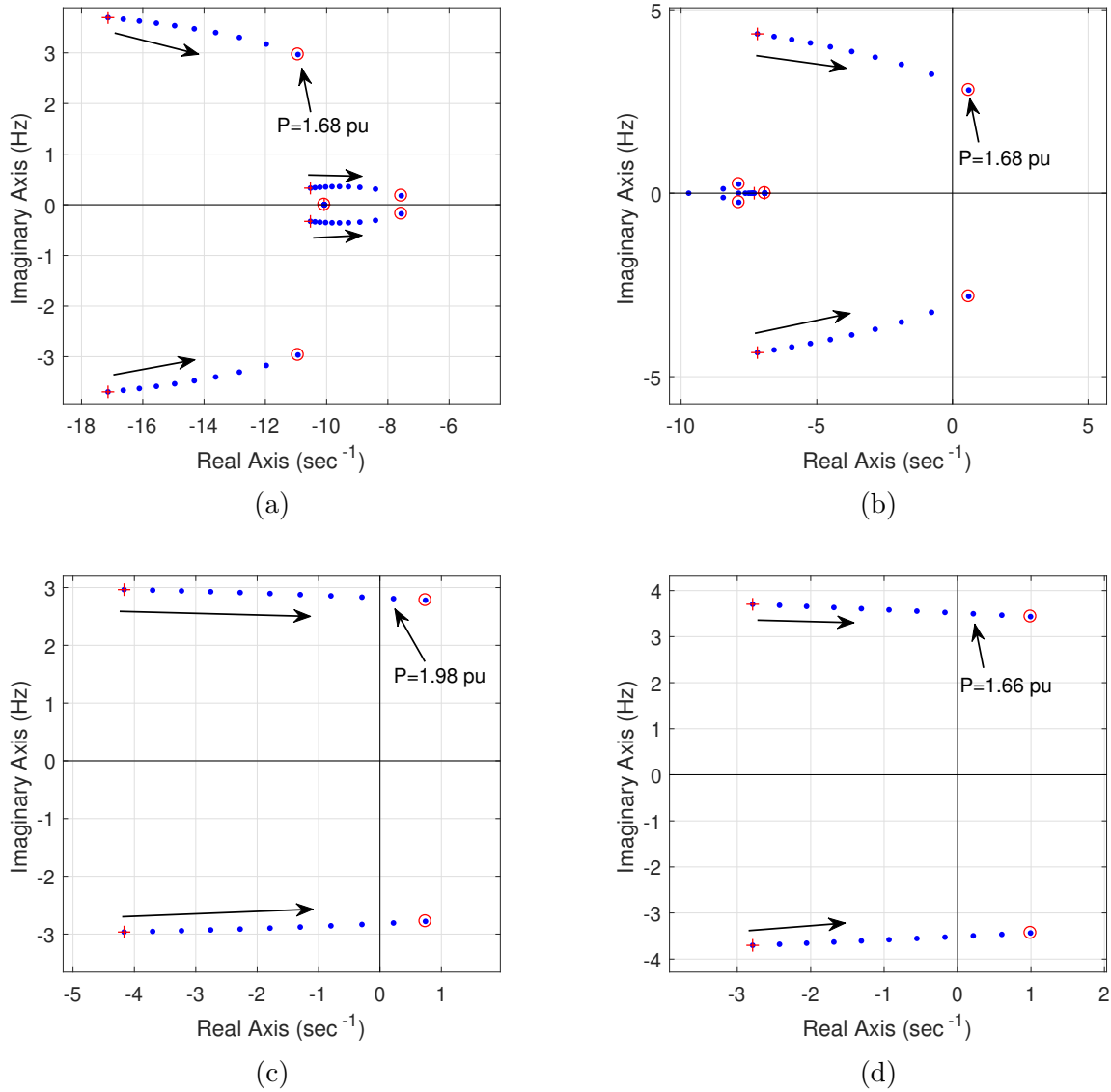


Figure 3.6: Eigen loci for different cases, interval for each point is 0.02 pu. Red plus is starting point, and red circle is ending point. (a) P/Q control with Parameter I, starting condition is P=1.5 pu. (b) P/Q control with Parameter II, starting condition is P=1.5 pu. (c) P/V control with Parameter I, starting condition is P=1.8 pu. (d) P/V control with Parameter II, starting condition is P=1.5 pu.

Table 3.1: Results comparison

Case studies	Test bed	Power limit (pu)	Oscillation frequency (Hz)	Values before event		
				P (pu)	Q (pu)	V (pu)
P/Q control with Para. I	Simulation	1.68	-	1.65	0.2	1
	Experiment	1.70	-	1.65	0.2	1
P/Q control with Para. II	Simulation	1.61	3	1.58	0.2	1.05
	Experiment	1.65	3	1.58	0.2	1.05
P/V control with Para. I	Simulation	1.94	2.8	1.92	0.42	1
	Experiment	1.97	2.8	1.92	0.42	1
P/V control with Para. II	Simulation	1.59	3.3	1.53	0.19	1
	Experiment	1.57	3.3	1.58	0.19	1

### 3.7 Summary

Since the laboratory experiment is benchmarked with simulation model built in MATLAB/SimPowerSystems, and operating at the same condition, dynamic simulation results and steady-state values can be used to compare for the same event: a step change in P. Table 3.1 summarize these results in digital for a better comparison, which shows excellent matching with only slight difference on the marginal power limits.

## Chapter 4: IBR System with VAR Devices

### 4.1 Comparison of SynCon and STATCOM

#### 4.1.1 Model Description

##### 4.1.1.1 *Wind Farm*

<sup>2</sup>The investigated system is a type-4 wind farm connected to a grid through a transmission line. Fig. 4.1 presents the structure of the system. The terminal voltage of wind farm is 575 V, and it is increased to 220 kV via two step-up transformers. The reactive power devices are connected to the grid through a 22 kV/220 kV transformer. The grid transmission network is comprised of two parallel impedance lines. A circuit breaker is shown and on/off of the breaker changes the total transmission network impedance.

The type-4 wind farm is constituted by a synchronous machine, a machine side converter (MSC) and a grid side converter (GSC), which is connected to PCC through a choke filter. The GSC consists of an inner current control loop and outer voltage control loops is shown in Fig. 4.2. This kind of control is well illustrated in Chapter. 2. And the parameters of the wind farm and controllers are listed Table 4.1

##### 4.1.1.2 *STATCOM*

STATCOM is widely adopted in power system to maintain voltage profile and enhance voltage stability by offering additional reactive power. It consists of a DC capacitor and a

---

<sup>2</sup>This chapter was published in Electric Power Systems Research [45] and has been accepted in 2022 IEEE PES General Meeting [46]. Permission is included in Appendix A

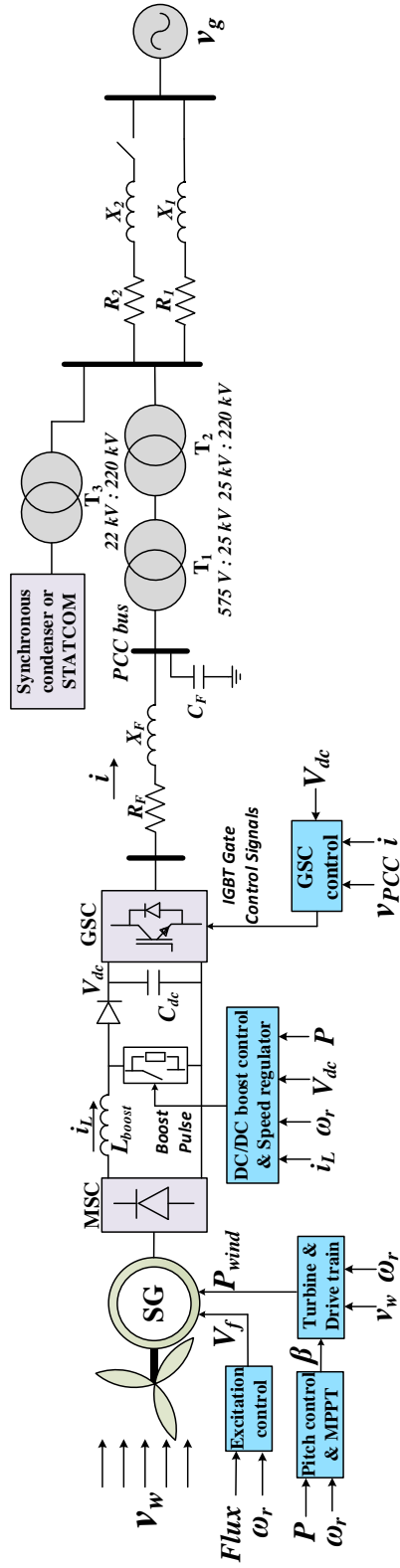


Figure 4.1: EMT test bed structure of a type-4 wind farm with reactive power devices.

voltage source converter, which is connected to a grid through a transformer, as shown in Fig. 4.4a.

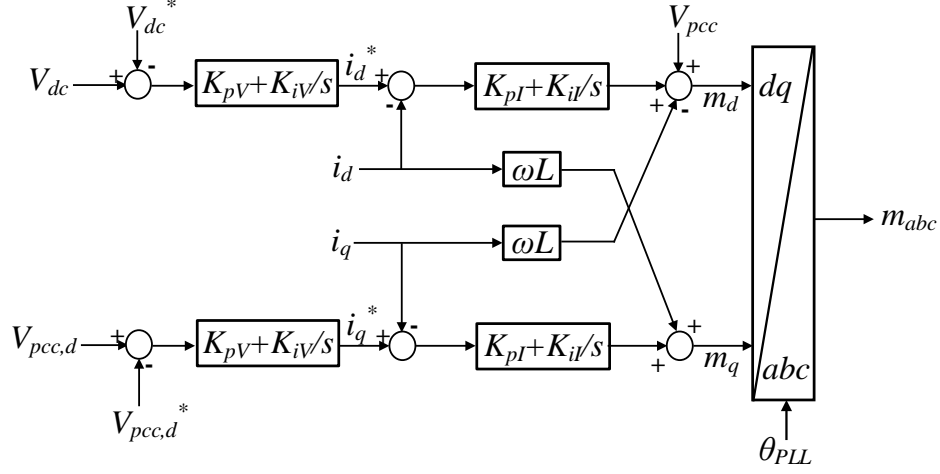
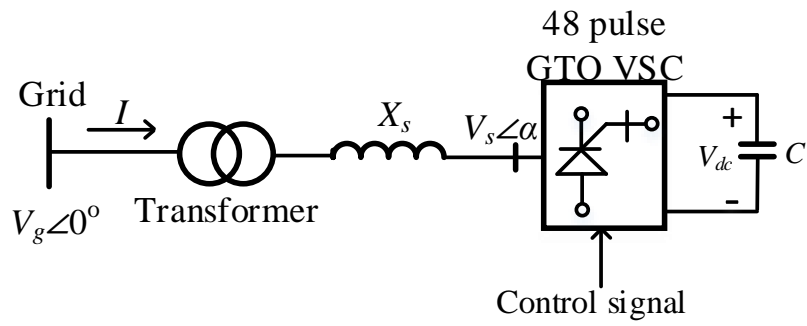


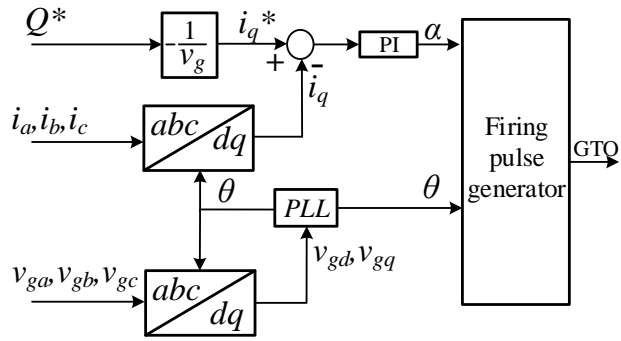
Figure 4.2: GSC control structure. The dc and ac voltage references are set at 1 pu.

Table 4.1: Parameters of the type-4 wind farm

Description	Parameters	Value (SI)
Rated Power	$P_{Rated}$	100 MW
Rated voltage	$V_{Rated}$	575 V
Nominal freq.	$f_{nom}$	60 Hz
DC-link voltage	$V_{DC}$	1100 V
Converter filter	$L_1, R_1$	0.06 mH, 0.45 m $\Omega$
Shunt capacitor	$C$	90 mF
Stator winding reactance	$R_s, X_{ls}$	1.44 m $\Omega$ , 40.8 m $\Omega$
Synchronous reactances	$X_d, X_q$	313 m $\Omega$ , 114 m $\Omega$
Transient reactance	$X'_d$	71 m $\Omega$
Subtransient reactances	$X''_d, X''_q$	60.5 m $\Omega$ , 58.3 m $\Omega$
Open-circuit time constant	$T'_{do}, T''_{do}$	4.49 s, 0.0681 s
Short-circuit time constant	$T''_q$	0.0513 s
Inertia constant, poles	H, p	0.62, 2
Friction factors	F	0.01
Current PI controller	$k_{pi}, k_{ii}$	0.4, 48
DC voltage PI controller	$k_{p,dc}, k_{i,dc}$	1, 100
AC voltage PI controller	$k_{p,ac}, k_{i,ac}$	0.25, 25
PLL	$k_{p,PLL}, k_{i,PLL}$	60, 4480



(a)



(b)

Figure 4.3: STATCOM circuit and control. (a) Single-line diagram circuit of STATCOM. (b) Reactive power control block diagram of STATCOM.

The transferred active power ( $P$ ) and reactive power ( $Q$ ) from the grid to the STATCOM are controlled by adjusting the output voltage of the converter.  $P$  and  $Q$  can be represented in (4.1).

$$\begin{aligned} Q &= \frac{|V_g|(|V_g| - |V_s| \cos \alpha)}{X_s} \\ P &= |V_g||V_s| \frac{\sin(-\alpha)}{X_s} \end{aligned} \quad (4.1)$$

where  $V_g$  is grid voltage amplitude at 1 p.u. and the phase angle is  $0^\circ$ ,  $|V_s|$  and  $\alpha$  are the amplitude and phase angle of STATCOM's terminal voltage.

According to (4.1), it can be concluded that the amount of transferred  $Q$  is controlled by adjusting the magnitude of the STATCOM terminal voltage and  $P$  is controlled by adjusting the phase angle. Since the STATCOM is used to offer reactive power, the phase angle between sending and receiving end is zero at steady state. Hence, when the STATCOM voltage is lower than grid side, the grid sends reactive power to the STATCOM. Otherwise, the STATCOM sends reactive power to the grid. Fig. 4.4 shows the STATCOM operation by phasor diagrams.

The STATCOM tested in this paper uses a voltage source converter built of four 12-pulse three-level GTO inverters. Its detailed model is available in the demo of MATLAB/SimScape [47]. This model is developed by P. Giroux and G. Sybille of Hydro-Quebec. Fig. 4.5(f) shows the multi-stepped output line-to-line voltage of the 48-pulse STATCOM. The zigzag phase-shifting transformers are connected to the VSC terminals. A simplified block diagram of the reactive power control is shown in Fig. 4.4b [48]. The instantaneous three-phase terminal voltage is used to generate the reference angle  $\theta$  through a PLL. Line current  $i$  is decomposed into real and reactive current, and the reactive current  $i_q$  is compared with the reference reactive current  $i_q^*$  to produce an angle  $\alpha$ , which defines the phase shift between converter output voltage and grid side voltage. Since the PLL aligns the grid voltage to  $d$ -axis,  $v_q$  is kept as 0, then  $Q = -i_q V_g$ . The reference reactive current can be generated from reference reactive power  $Q^*$ .



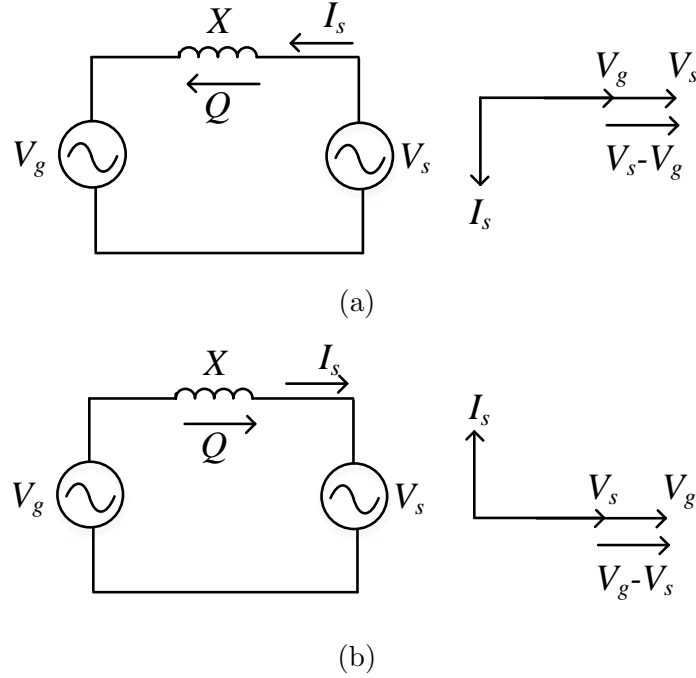


Figure 4.4: STATCOM operation. (a) Capacitive operation. (b) Inductive operation.

The magnitude and phase angle of the converter voltage determine the real and reactive power transferred between grid and STATCOM. If the STATCOM is only used for reactive power compensation, then the phase angle is kept as 0, and reactive power is controlled by the voltage magnitude, which is directly proportional to capacitor voltage  $V_{dc}$ .

If the STATCOM aims to increase its reactive power to the grid, or the grid aims to decrease its reactive power to the STATCOM,  $V_{dc}$  should increase and the phase angle  $\alpha$  should reduce to allow real power flowing from the grid to the STATCOM to charge the DC-link capacitor. The control logic in Fig. 4.4b shows that increasing  $Q^*$  causes a reduced  $i_q^*$  and  $\alpha$  will be subject to reduction initially.

Fig. 4.5 presents the dynamic performance of the STATCOM during operation. At  $t = 2$  s, the STATCOM increases its reactive power supply to the grid from 0 pu to 0.4 pu. This change causes the angle of STATCOM voltage  $\alpha$  to have a drop so that real power can be injected to the STATCOM to increase the capacitor voltage  $V_{dc}$ . The increased  $V_{dc}$  leads to a higher STATCOM output voltage  $V_s$  to realize reactive power generation. At  $t = 4$  s, the

STATCOM reverses its reactive power command to absorb 0.4 pu reactive power from grid. In turn, its dc-link voltage and ac voltage reduce. The phase angle  $\alpha$  is subject to change during transients but remains at 0 at steady state.

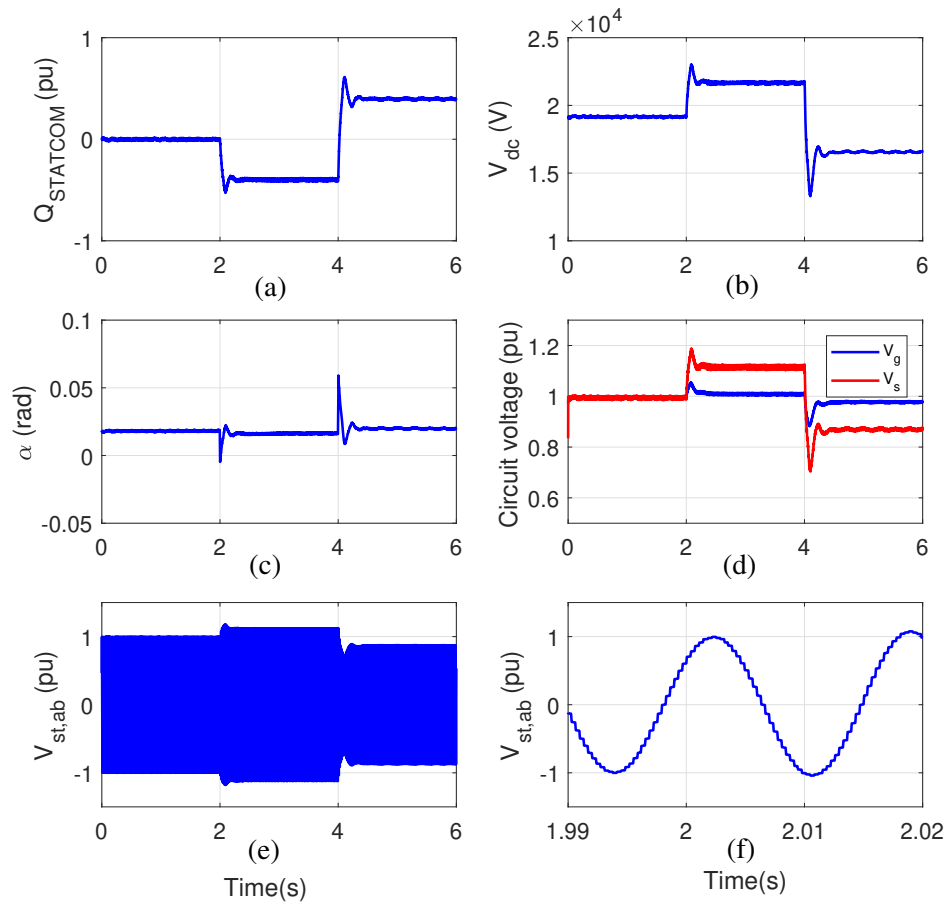


Figure 4.5: STATCOM dynamic performance analysis. (a) Reactive power from the grid to the STATCOM. (b) STATCOM capacitor voltage. (c) STATCOM terminal voltage angle. (d) Terminal voltages of STATCOM and grid. (e) STATCOM line-to-line voltage. (f) Zoom-in STATCOM line-to-line voltage.

Since STATCOM only provides reactive power support and does not generate or absorb any active power, the phase angle  $\alpha$  should be zero according to 4.1. But it can be seen in this figure that  $\alpha$  is not kept as zero even there is no active power transferred between the grid and STATCOM. In order to find the voltage angle difference between STATCOM and grid, we need to measure the STATCOM converter output voltage. The STATCOM system used in this paper is from MATLAB/SimPowerSystems block. It includes a 48-pulse

VSC, which consists of four identical 12-pulse GTO converters connected in series with four Zigzag transformers. Fig. 4.6 depicts the 48-pulse VSC-GTO converter model. So the phase-A voltage of the STATCOM terminal is sum of each transformer secondary side phase A voltage, which can be calculated in (4.2).

$$V_{ST,A} = V_{an\_Tr1Y} + V_{an\_Tr1D} * \frac{1}{\sqrt{3}} + V_{an\_Tr2Y} + V_{an\_Tr2D} * \frac{1}{\sqrt{3}} \quad (4.2)$$

Since the secondary and fourth transformers are Delta connection, a factor  $\frac{1}{\sqrt{3}}$  is used to convert L-L voltage to per-phase voltage.

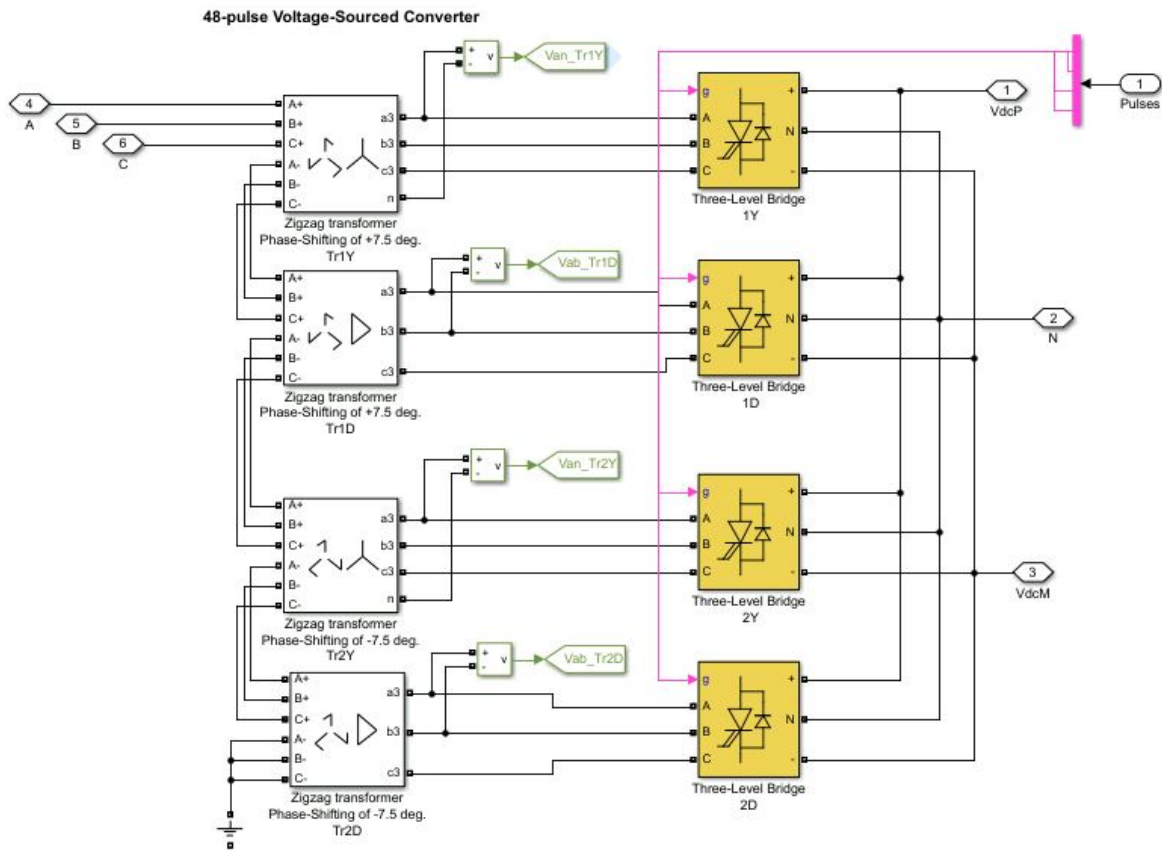


Figure 4.6: System configuration of 48-pulse GTO-VSC based STATCOM.

The grid side phase-A voltage can be measured directly, and is denoted as  $V_{g,a}$ , so the voltage difference is in (4.3).

$$\theta_v = \angle V_{ST,A} - \angle V_{g,A} \quad (4.3)$$

The simulation results comparison of  $\theta$  and  $\theta_v$  is shown in Fig. 4.7. The voltage angle between the STATCOM and grid voltage is kept as zero, but the angle from STATCOM controller is about 0.017 rad (1 degree).

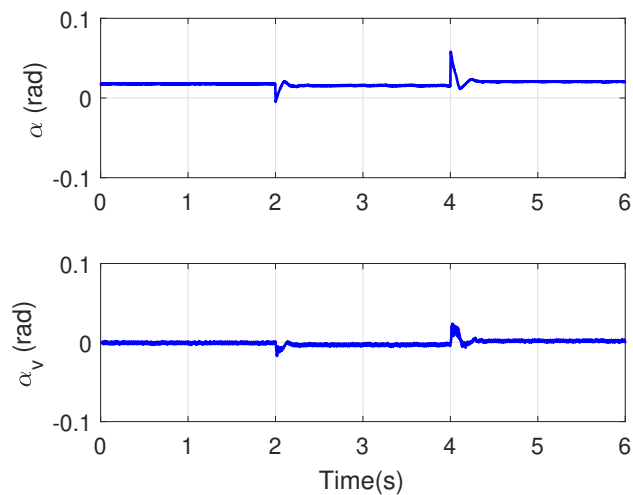


Figure 4.7: Comparison of  $\alpha$  and  $\alpha_v$

According to the MATLAB documentation for STATCOM (detailed model) [47], 0.5 degrees of  $\alpha$  steady state value is required to maintain a small active power flow for transformer and converter losses. In this paper, the parameters of STATCOM model are modified to accommodate the Type-4 wind farm system. Compared to MATLAB STATCOM demo, the impedance of transformer is decreased, and power rating and voltage level of STATCOM are also changed. So we think the  $\alpha$  of 1 degree is for converter losses and is reasonable in this case.

Besides the reactive power control, the terminal voltage control is also applied in the STATCOM as shown in Fig. 4.8. Grid side three-phase voltage  $v_{ga}$ ,  $v_{gb}$  and  $v_{gc}$  are converted into  $dq$ -frame, and its magnitude is calculated as follows.

$$V_g = \sqrt{V_{gd}^2 + V_{gq}^2} \quad (4.4)$$

The error of  $V_g$  and reference  $V^*$  goes to a PI controller, which generates reference  $q$ -axis current  $i_q^*$ . The inner loop has the same control structure with reactive power control. Two voltage PI controller parameters are used to compare the dynamic performance.

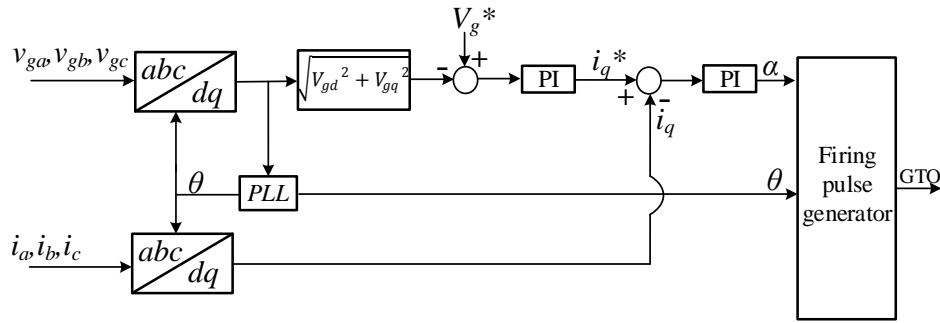


Figure 4.8: Voltage control block diagram of STATCOM.

The parameters of the STATCOM and its controller are listed in Table 4.2.

Table 4.2: Parameters of STATCOM

Parameters	Value (SI)
Rated Power	100 MW
Rated voltage	22 kV
Nominal freq.	60 Hz
DC capacitor	2000 $\mu$ F
$I_q$ PI controller	$5 + \frac{40}{s}$
V PI controller	Para I: $12 + \frac{250}{s}$ Para II: $12 + \frac{100}{s}$
PLL	$60 + \frac{1400}{s}$

### 4.1.1.3 SynCon

Compared to a STATCOM, a SynCon is a traditional device of reactive power generation for reactive power generation and absorption through electromagnetic field instead of power electronics converters. For a system with limited short-circuit power capacity, SynCons are usually installed near the generation units to absorb or generate reactive power and maintain a stable network voltage through excitation control.

A SynCon essentially is a synchronous machine working under no-load without real power output. An excitation system is used to provide excitation current and regulate the terminal voltage for the machine. According to IEEE standard, there are three different groups of excitation systems: DC type, AC type, and Static Excitation System (type ST).

In this model, the SynCon is equipped with a DC2A excitation system as shown in Fig. 4.9 [49]. At steady-state, both power system stabilizer voltage  $V_s$  and feedback signal  $V_F$  are zero, which means only motor terminal voltage  $V_C$  is controlled.  $T_B$  and  $T_C$  are the time constants. The parameters are listed in Table 4.3.

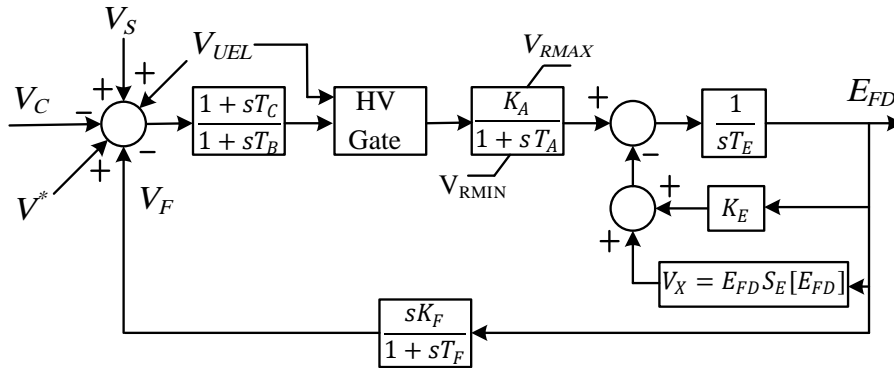


Figure 4.9: Synchronous condenser exciter model.

Table 4.3: Parameters of synchronous condenser

Parameters	Value (SI)
Rated Power	20 MW
Rated voltage	22 kV
Nominal freq.	60 Hz
$X_d, X'_d, X''_d$	654.4 m $\Omega$ , 99 m $\Omega$ , 79 m $\Omega$
$X_q, X''_q$	629.6 m $\Omega$ , 79.2 m $\Omega$
$R_s, X_{ls}$	1.8 m $\Omega$ , 55.4 m $\Omega$
$T'_{do}, T''_{do}$	4.5 s, 0.04 s
$T'_q, T''_q$	0.67 s, 0.09 s
Inertia constant, pols	0.6, 2
Friction factors	0.6
DC capacitor	2000 $\mu$ F
$T_C, T_B$	1, 1
$K_A$	300
$T_E, K_E$	0.01, 2
$K_F$	0.01

#### 4.1.2 EMT Simulation Results

##### 4.1.2.1 Wind Farm Only

For the 100 MW wind farm grid integration system without any reactive power devices, a dynamic event is created by tripping of a transmission line through a breaker switching. With a closed breaker, the impedance of the grid is denoted in (4.5).

$$Z_g = (R_1 + jX_1) || (R_2 + jX_2) \quad (4.5)$$

If the breaker is switched off, the line impedance will be increased.

$$Z_g = R_1 + jX_1 \quad (4.6)$$

Then, the grid becomes weaker through the breaker's action.

The wind farm simulation results of the PCC voltage are presented in Fig. 4.10. It can be observed that the system becomes unstable when  $X_g$  increases to 0.42 pu from 0.2 pu,

while it keeps as stable when  $X_g$  increases to 0.41 pu. Furthermore, the oscillation frequency of the unstable condition is about 9 Hz.

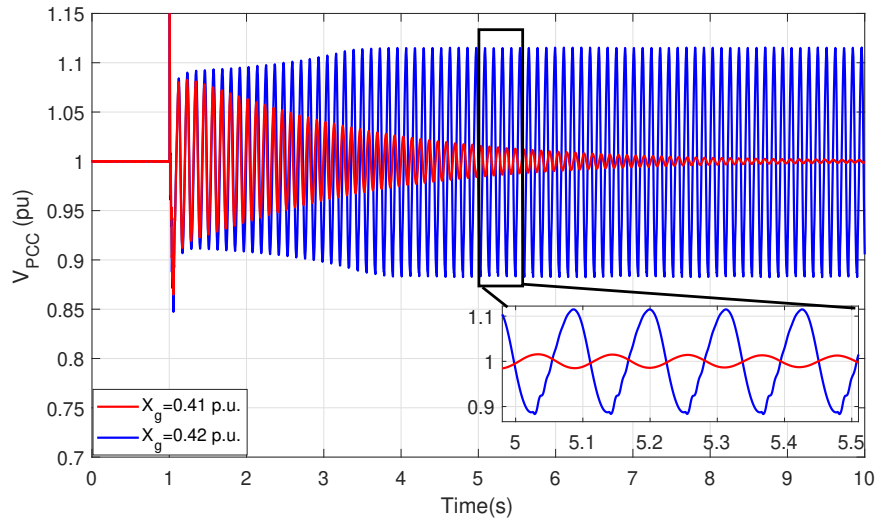


Figure 4.10: Voltage at PCC bus in wind farm system. The line impedance changes at 1 second.

#### 4.1.2.2 Wind Farm with STATCOM

To check the effect of STATCOM, the STATCOM is connected to the 22-kV bus. Two cases are simulated. In the first case, there is no active and reactive power transferred between the STATCOM and the power system. Fig. 4.11 presents the waveform of the PCC voltage and STATCOM reactive power. It can be noted that the system collapses when  $X_g$  changes from 0.2 pu to 0.42 pu due to line tripping. As illustrated in the sole wind farm case study, the wind farm marginal stability condition is at  $X_g = 0.41$  pu, which means the STATCOM cannot improve the system stability performance when there is no reactive power compensation under this control strategy and this set of control parameters.

As a comparison, another case is conducted when the STATCOM injects reactive power into the system. Fig. 4.11b shows that the oscillations are suppressed if the STATCOM injects 0.1 pu reactive power into the system.



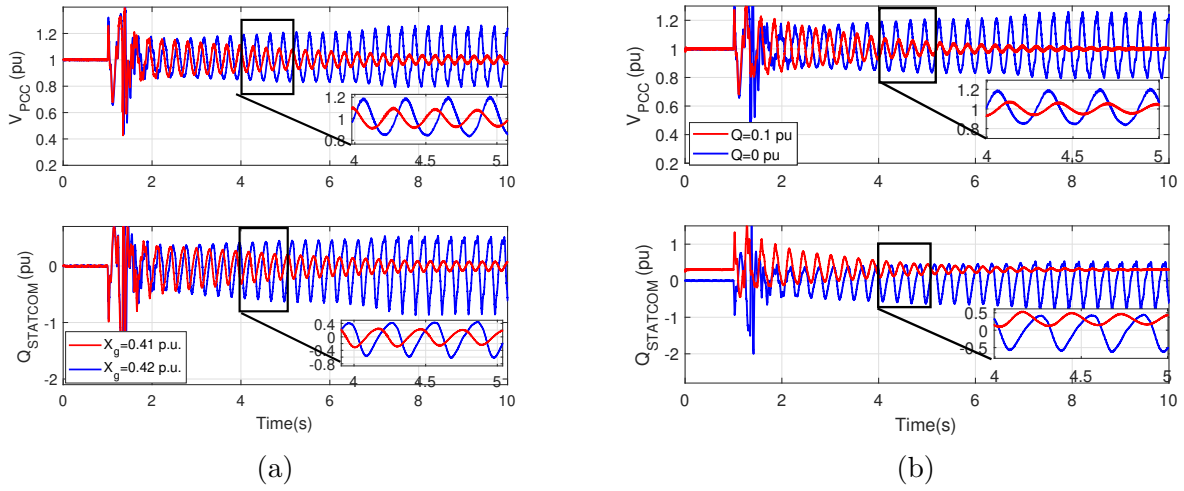


Figure 4.11: (a) Voltage at PCC bus and reactive power from STATCOM. (b) Voltage at PCC bus in wind farm system with STATCOM when  $X_g$  changes to 0.42 pu at 1 second, STATCOM injects 0 or 0.1 pu reactive power to system.

Different PI controller parameters are also examined in this control system. The dynamic performance comparison is shown in Fig. 4.12a. At 1 second, the  $X_g$  increases to 0.42 pu, the larger PI parameter has a better stability performance, and the smaller parameters may worsen the oscillation. Fig. 4.12b demonstrate the larger PI parameters could increase the marginal stability condition to 0.46 pu.

If the reactive power control is removed and the system is working with open loop control as shown in Fig. 4.13, the control signal  $\alpha$  is set as a constant to ensure reactive power from STATCOM be zero during operation.

Fig. 4.14a shows the system becomes stable when  $X_g$  increases to 0.42 pu with open loop control. Fig. 4.14b shows the open loop control is able to increase the marginal  $X_g$  to 0.48 pu. When  $X_g$  changes 0.49 pu, the system becomes unstable and oscillation frequency is about 17 Hz.

When STATCOM is operated with voltage control, its reference voltage is tuned to maintain  $Q$  from STATCOM as zero. Two voltage controller parameters are implemented and the rest of parameters are the same with current control system. Fig. 4.15a shows the simulation results when  $X_g$  increases to 0.41 pu and 0.42 pu with Para I. It can be seen

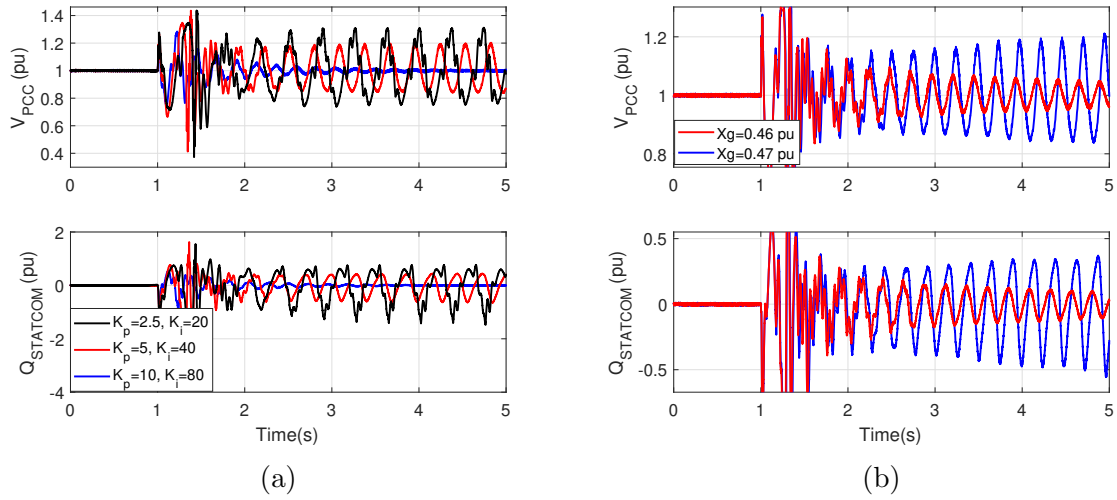


Figure 4.12: (a) System dynamic performance comparison of different PI controller when  $X_g$  increases to 0.42 pu. (b)  $X_g$  increases to 0.46 pu and 0.47 pu with the PI controller parameters as  $k_p = 10$ ,  $k_i = 80$ .

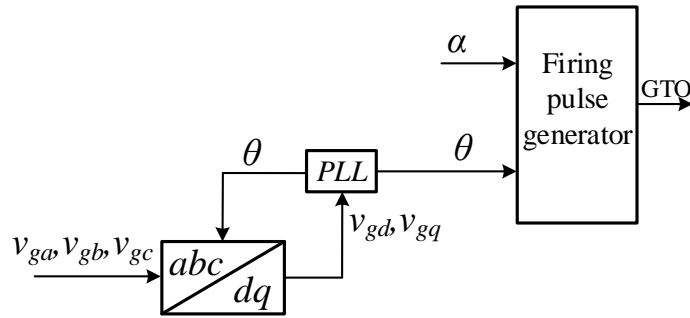


Figure 4.13: STATCOM open loop control system.

that the system stability performance is the same with reactive power control. But if the parameters change to Para II, the system will be stable when  $X_g$  changes to 0.42 pu as shown in Fig. 4.15b. Fig. 4.16 illustrates the system with Para II could increase the marginal stability condition to 0.49 pu. The oscillation frequency when  $X_g$  changes to 0.50 pu is about 18 Hz.

These cases indicate that the STATCOM only has limited capacity to improve the system stability performance under the zero reactive condition.

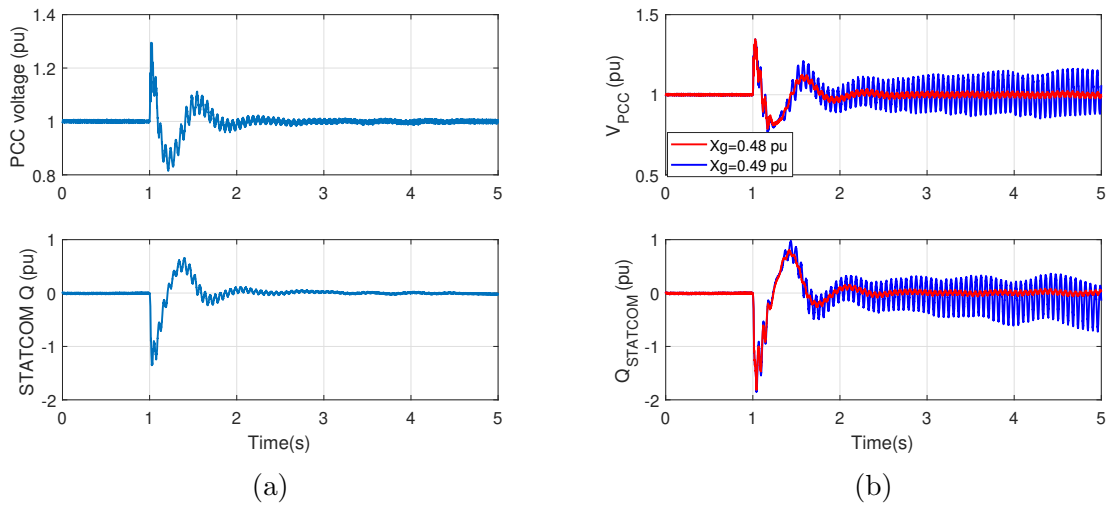


Figure 4.14: With open loop control, voltage at PCC bus and the reactive power from the STATCOM when (a)  $X_g$  increases to 0.42 pu. (b)  $X_g$  increases to 0.48 pu and 0.49 pu.

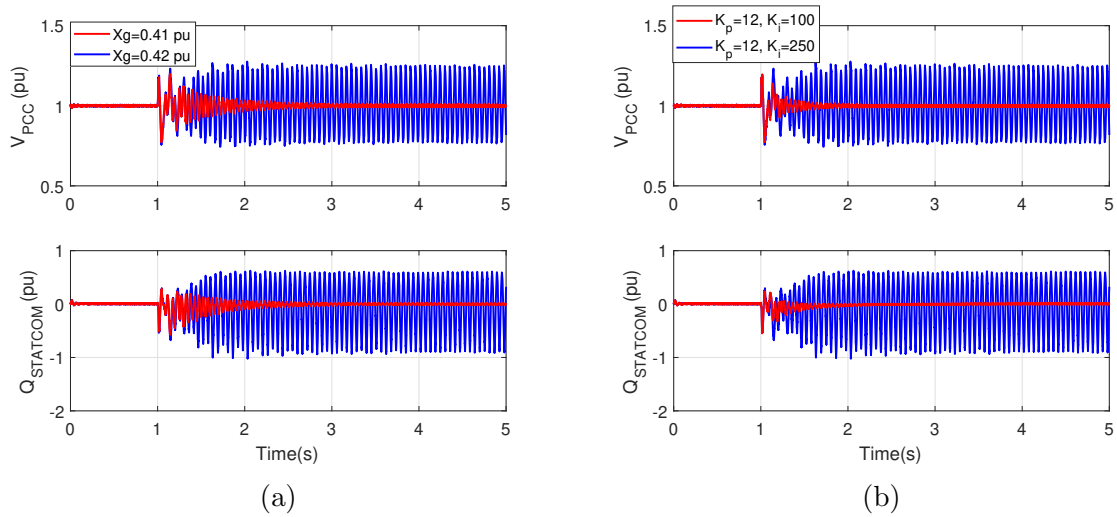


Figure 4.15: Voltage at PCC bus and the reactive power from the STATCOM when (a)  $X_g$  increases to 0.41 pu and 0.42 pu with Para I. (b)  $X_g$  increases to 0.42 pu with Para I and Para II.

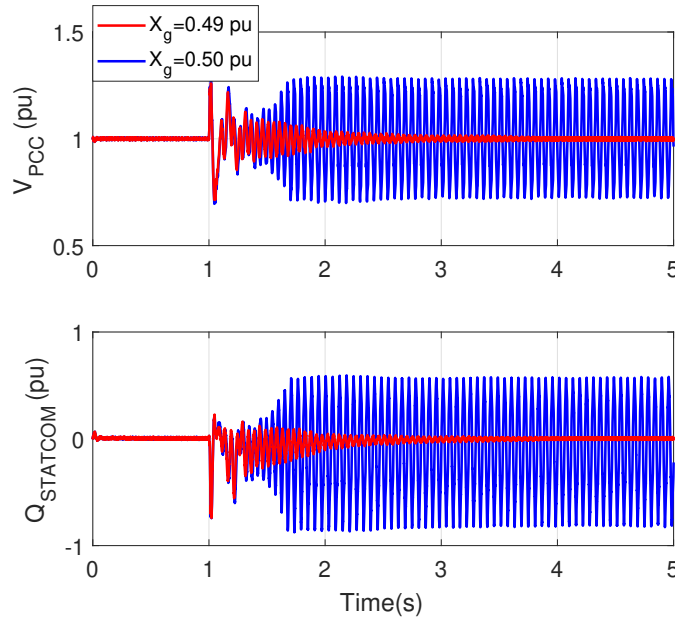


Figure 4.16: Voltage at PCC bus and the reactive power from the STATCOM when  $X_g$  increases to 0.49 pu and 0.50 pu with Para II.

#### 4.1.2.3 Wind Farm with SynCon

Finally, the SynCon replaces the STATCOM and operates in parallel with the wind farm. Its generated power and reactive power are regulated by an excitation system. In this case, the synchronous condenser is operated under no power condition.

Fig. 4.17(a) shows the PCC bus voltage and reactive power from the SynCon when  $X_g$  changes from 0.2 pu to 0.42 pu. After a short period of oscillations, the system recovers to stability. To find out the marginal stability condition, the transmission line impedance is adjusted. Fig. 4.17b shows the reactive power when  $X_g$  increases to 0.67 and 0.68 pu, which demonstrates the marginal stability condition is  $X_g = 0.67$  pu. The cases illustrate that the SynCon can improve the stability performance significantly even without reactive power compensation.

Although both STATCOM and SynCon have the capability providing reactive power and improving stability performance due to reactive power supply, SynCon has advantage over STATCOM at zero reactive power condition.

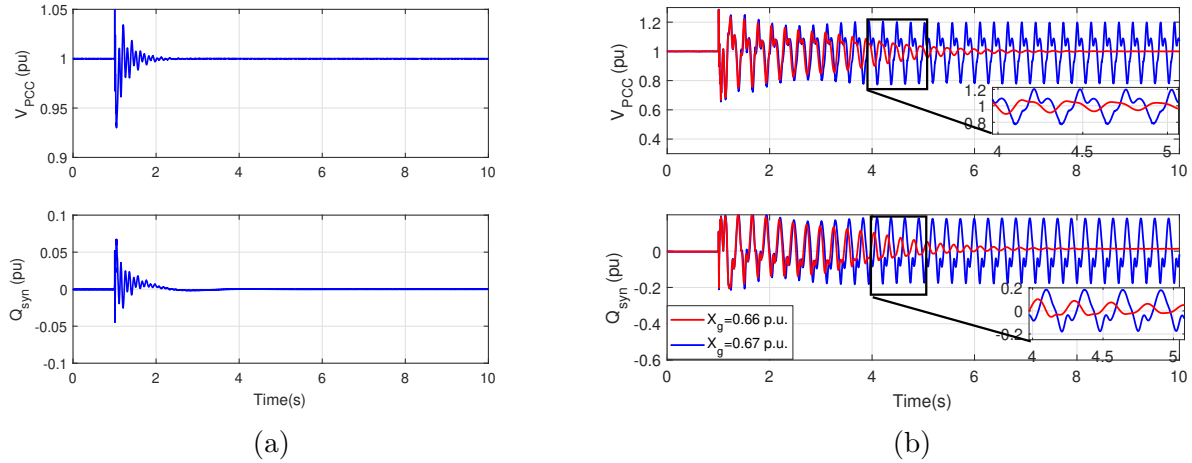


Figure 4.17: (a) Voltage at PCC bus and synchronous condenser reactive power in wind farm system when  $X_g$  changes from 0.20 to 0.42 pu. (b) Voltage at PCC bus and the reactive power from the SynCon for two additional cases:  $X_g$  changes from 0.20 pu to 0.66 pu and 0.67 pu, respectively.

#### 4.1.3 Admittance Model Extraction

There are number of approaches to establish the impedance models by simplifying the power systems. These methods always decompose models into two equivalent parts as load and source [13], [50], as Fig. 4.18 shows. The disturbance is injected into the grid or load subsystem.

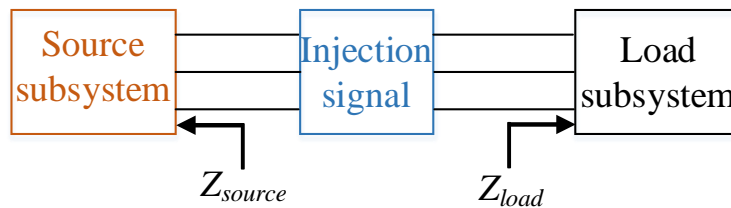


Figure 4.18: Simplified system diagram using harmonic injection.

The detailed harmonic injection process is demonstrated in Chapter 2. In this model, the injection frequencies are swept from 1 to 100 Hz with 1 Hz interval.  $Dq$ -frame voltages and currents are recorded and processed. FFT window is long enough to reduce the impact of spectral analysis. Fig. 4.19 shows the wind farm admittance model. Each red plus sign means an injected voltage point.

The measurements can be fitted to an s-domain transfer function matrix via the vector fitting toolbox [30]. Vector fitting treats a system as a transfer function matrix, and each transfer function consists of a polynomials numerator and denominator. This method evaluates the coefficients of both numerator and denominator by iterated least-squares estimation. The order is firstly to set as 13 for each admittance of  $Y_{dd}$ ,  $Y_{dq}$ ,  $Y_{qd}$  and  $Y_{qq}$ . Fig. 4.19 illustrates the comparison of the Bode plot from estimated model (blue line) and measurement data (red crosses) from harmonic injection. The estimation matches the measurements very well.

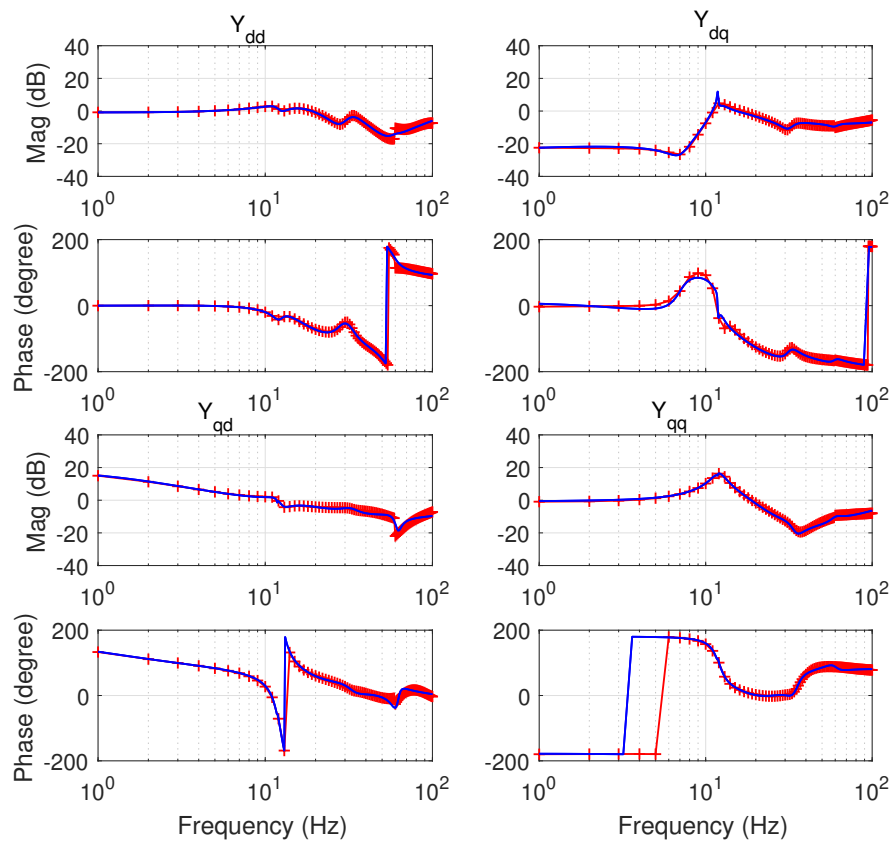


Figure 4.19: Comparison of the wind farm admittance model from vector fitting and harmonic injection measurement points.

#### 4.1.4 Stability Analysis

This section presents  $s$ -domain admittance based eigenvalue analysis. The wind farm is represented by a Norton equivalent circuit consisting of a current source  $i_{\text{wind}}$  connected with an admittance  $Y_{\text{wind}}$  in parallel. The grid side is also converted to a Norton equivalent circuit with a current source  $i_s$  and line admittance  $Y_{\text{grid}}$ . Thus, from the view of the PCC bus, there are two parallel-connected shunt admittance. At steady state, the system operation condition point is transferred to  $dq$ -frame by using Park transformation. The voltage and current variables in  $dq$ -frame are related as follows.

$$\begin{bmatrix} i_d \\ i_q \end{bmatrix} = \underbrace{(Y_{\text{wind}} + Y_{\text{grid}})}_Y \begin{bmatrix} v_d \\ v_q \end{bmatrix} \quad (4.7)$$

The  $Y_{\text{wind}}$  and  $Y_{\text{grid}}$  can be represented as follows.

$$Y_{\text{wind}} = \begin{bmatrix} Y_{dd} & Y_{dq} \\ Y_{qd} & Y_{qq} \end{bmatrix}, \quad Y_{\text{grid}} = \begin{bmatrix} R_g + sL_g & -\omega_o L_g \\ \omega_o L_g & R_g + sL_g \end{bmatrix}$$

where  $\omega_o$  is the nominal frequency.

If the system is regarded as an input/output system, where the injected current and the PCC voltage are denoted as the input and the output, respectively, then the transfer function  $G(s)$  for the multi-input multi-output (MIMO) system is  $Y^{-1}$ .

The poles of  $G(s)$  are the zeros of the determinant of  $Y(s)$ , where  $Y(s)$  is the inverse of  $G(s)$ . This statement can be elaborated as follows.

First, the poles of a closed-loop transfer function  $G(s)$  are the eigenvalues of the system matrix  $A$ , where  $A, B, C, D$  are the minimal state-space realization of  $G(s)$ . This definition can be found in well-known control textbooks, e.g., [51].

$$\dot{x} = Ax + Bu, \quad y = Cx + Du \quad (4.8)$$

The closed-loop system's transfer function  $G(s)$  has the following relationship with  $A, B, C, D$ .

$$G(s) = C(sI - A)^{-1}B = \frac{1}{\phi(s)}Cadj(sI - A)B + D \quad (4.9)$$

where  $\phi(s)$  is the characteristics function of  $G(s)$ .

$$\phi(s) \triangleq \det(sI - A) = \prod_{i=1}^n (s - \lambda_i) \quad (4.10)$$

It can be seen that the poles of  $G(s)$  are the roots of the characteristic function  $\phi(s)$ . Pole of  $G(s)$  are also the eigenvalues of the system matrix  $A$ .

If we derive  $G(s)$ 's expression from its inverse  $Y(s)$ , then we found that  $G(s)$  is associated with the determinant of  $Y(s)$  in the following way.

$$G(s) = Y^{-1}(s) = \frac{1}{\det(Y(s))}adj(Y(s)) \quad (4.11)$$

Thus, it can be seen that  $\phi(s)$  is the numerator of the determinant of  $Y(s)$ . Therefore, the system eigenvalues are the zeros of  $\det(Y(s))$ .

The same statement can be found in a 1999 paper by Prof. A. Semleyn of University of Toronto [33] on finding closed-loop system eigenvalues through computing the zeros of the network admittance matrix, though the reasoning is different. Semlyen started from the voltage and current relationship as follows.

$$Y(s)v = 0 \quad (4.12)$$

where  $v$  is the union of the nodal voltage and the total current into a node is zero.

To find a non-trivial solution  $v$ ,  $Y(s)$  has to be singular. This means that  $s$  will make the determinant of  $Y(s)$  zero:  $\det(Y(s)) = 0$  and  $s$  is an eigenvalue of the system.



With the admittance of the wind farm being identified from measurements, the eigenvalues of the entire system can be found if the transmission line parameters are known.

Furthermore, when a reactive power device is employed in the system, then the overall admittance is in (4.13).

$$Y = Y_{\text{wind}} + Y_{\text{grid}} + Y_{\text{shunt}} \quad (4.13)$$

where  $Y_{\text{shunt}}$  is the admittance model of the SynCon or STATCOM.

The  $s$ -domain model from vector fitting can be used for eigenvalue analysis.

#### 4.1.4.1 Wind Farm Only

According to (4.13), the eigenvalue loci are plotted in Fig. 4.27a with known  $Y_{\text{wind}}$ , and  $Y_{\text{grid}}$  has an increment of 0.01 pu from 0.3 pu to 0.5 pu.

It can be observed that there is one pair of complex conjugate mode affected by the varying impedance. When  $X_g$  is 0.42 pu, the oscillation mode at 9 Hz moves to right half plane (RHP), which corroborates with the simulation results shown in Fig. 4.10.

#### 4.1.4.2 Wind Farm with STATCOM

The STATCOM model is identified using harmonic injection method when it is operated in reactive power control with default parameters. The frequency is swept from 1 to 200 Hz with an interval of 1 Hz. Afterwards, the  $dq$ -admittance measurements of 200 points are obtained and processed by vector-fitting algorithm to arrive at the linear model  $Y_{\text{STATCOM}}$  in  $s$ -domain.

Fig. 4.27b shows the movements of the dominant zeros of  $Y_{\text{STATCOM}} + Y_{\text{wind}} + Y_{\text{grid}}$ , as  $X_g$  varying from 0.3 pu to 0.5 pu. It is evident that one pair of eigenvalues crosses the imaginary axis when  $X_g$  increases to 0.42 pu, which corroborates the EMT simulation results of Fig. 4.11.

#### 4.1.4.3 Wind Farm with SynCon

Similar to the STATCOM, the SynCon is also measured for its admittance model  $Y_{\text{syn}}$  in range of 1 to 200 Hz. Fig. 4.20c shows the Eigen Loci of the overall system when  $X_g$  is changed from 0.6 to 0.8 pu. It can be observed that a pair of eigenvalues move to the RHP when  $X_g$  reaches 0.67 pu. This analytical analysis corroborates the EMT simulation results.

#### 4.1.5 Comparison of Admittance of STATCOM and SynCon

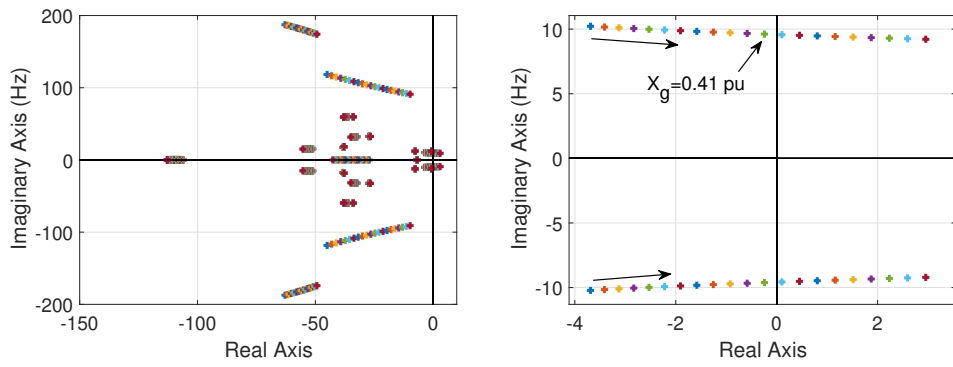
Fig. 4.21 presents the  $dq$ -domain admittance models of the SynCon and STATCOM. It should be mentioned that both the two models have the same operating condition in the wind farm system.

To have a better understanding, we resort to a different domain. The admittance model can be expressed in different domains, e.g., sequence domain or  $dq$ -frame. The two types of models are related as follows [52].

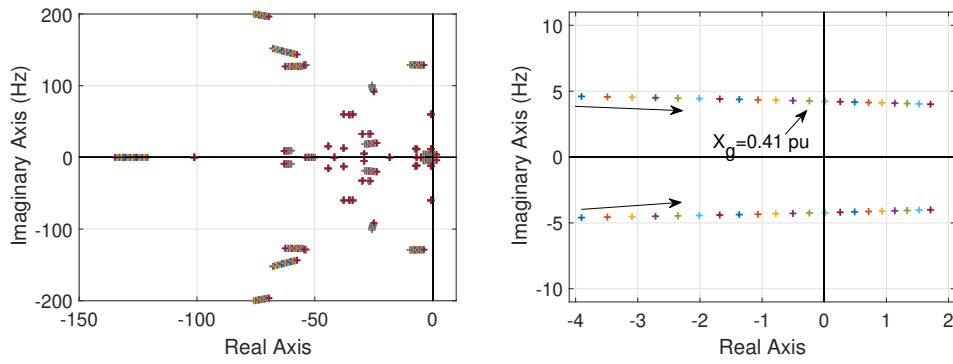
$$\begin{bmatrix} Y_{pp} & Y_{pn} \\ Y_{np} & Y_{nn} \end{bmatrix} = \frac{1}{2} \begin{bmatrix} 1 & j \\ 1 & -j \end{bmatrix} \begin{bmatrix} Y_{dd} & Y_{dq} \\ Y_{qd} & Y_{qq} \end{bmatrix} \begin{bmatrix} 1 & 1 \\ -j & j \end{bmatrix} \quad (4.14)$$

The sequence-domain admittance associates the two current phasors and two voltage phasors. The two voltage (current) phasors are referred to the phasors at positive-sequence at frequency  $\omega_p + \omega_1$  and negative-sequence at frequency  $\omega_p - \omega_1$ , where  $\omega_1$  is the nominal frequency of 60 Hz.

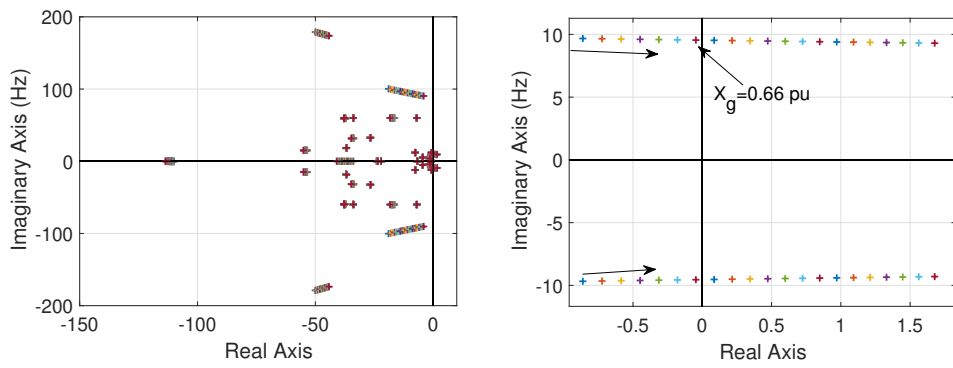
$$\begin{bmatrix} \bar{I}_p(j(\omega_p + \omega_1)) \\ \bar{I}_n(j(\omega_p - \omega_1)) \end{bmatrix} = \begin{bmatrix} Y_{pp}(j\omega_p) & Y_{pn}(j\omega_p) \\ Y_{np}(j\omega_p) & Y_{nn}(j\omega_p) \end{bmatrix} \begin{bmatrix} \bar{V}_p(j(\omega_p + \omega_1)) \\ \bar{V}_n(j(\omega_p - \omega_1)) \end{bmatrix} \quad (4.15)$$



(a)



(b)



(c)

Figure 4.20: Eigen loci for varying line impedance  $X_g$  for (a) wind farm, (b) wind farm with STATCOM, and (c) wind farm with SynCon. The right plots are the zoom-in of the left plots at critical mode.

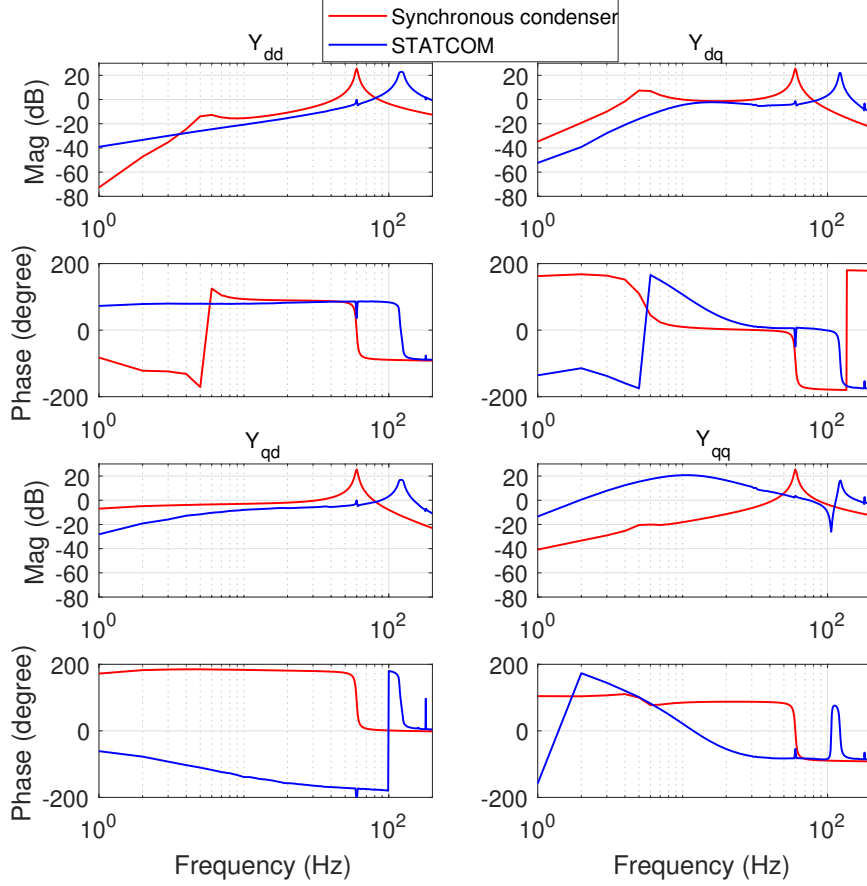


Figure 4.21:  $Dq$ -domain admittance comparison of synchronous condenser and STATCOM.

Combining (4.14) and (4.15), the sequence-based current is related to voltage through  $dq$ -admittance as follows.

$$\begin{bmatrix} \bar{I}_p \\ \bar{I}_n \end{bmatrix} = \frac{1}{2} \begin{bmatrix} 1 & j \\ 1 & -j \end{bmatrix} \begin{bmatrix} Y_{dd} & Y_{dq} \\ Y_{qd} & Y_{qq} \end{bmatrix} \begin{bmatrix} 1 & 1 \\ -j & j \end{bmatrix} \begin{bmatrix} \bar{V}_p \\ \bar{V}_n \end{bmatrix} \quad (4.16)$$

At steady-state, the operation condition is at 60 Hz, so the  $dq$ -domain admittance at 0 Hz will be analyzed. From the Bode plot, it can be observed that the steady-state admittance is at the leftmost frequency range.

The Bode plot indicates that the magnitude of  $Y_{dd}$ ,  $Y_{dq}$  and  $Y_{qq}$  in synchronous condenser are relatively small compared to  $Y_{qd}$  at steady state, thus they can be approximated to zero. The magnitude of  $Y_{qd}$  is found as -6 dB or 0.5 pu. Similarly, the magnitude of  $Y_{dd}$ ,  $Y_{dq}$  and

$Y_{qd}$  in STATCOM are treated as zero and  $Y_{qq}$  is -10 dB or 0.3 pu. Then we can conclude the  $dq$ -domain admittance models at steady-state as follows.

$$\mathbf{Y}_{\text{syn,dq}} = \begin{bmatrix} 0 & 0 \\ -0.5 & 0 \end{bmatrix}, \quad \mathbf{Y}_{\text{st,dq}} = \begin{bmatrix} 0 & 0 \\ 0 & -0.3 \end{bmatrix} \quad (4.17)$$

Assuming the system is balanced, positive and negative-sequence voltage are  $1\angle 0^\circ$  and 0, respectively.

For SynCon, the only non-zero element is  $Y_{qd}$  at 0 Hz, so the current can be calculated as follows.

$$\begin{bmatrix} \bar{I}_p \\ \bar{I}_n \end{bmatrix} = \frac{jY_{qd}}{2} \begin{bmatrix} 1 & 1 \\ -1 & -1 \end{bmatrix} \begin{bmatrix} \bar{V}_p \\ \bar{V}_n \end{bmatrix} \quad (4.18)$$

$$\Rightarrow \bar{I} = \bar{I}_p + \bar{I}_n^* = jY_{qd}\bar{V}_p = -j0.5\bar{V}_p = \frac{1}{j2}\bar{V}_p \quad (4.19)$$

Hence, the SynCon can be regarded as an impedance connected in parallel with PCC bus. As shown in Fig. 4.22, by adding a parallel branch, the impedance after PCC bus will be reduced and the grid strength is improved. This is the reason why SynCon can improve stability even without injecting any reactive power.

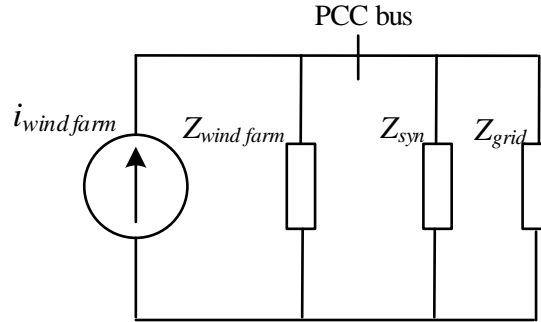


Figure 4.22: Equivalent circuit model of a wind farm connected with a SynCon.

Similarly, for the STATCOM, the sequence-domain admittance is expressed as follows.

$$\begin{bmatrix} \bar{I}_p \\ \bar{I}_n \end{bmatrix} = \frac{1}{2} \begin{bmatrix} Y_{qq} & -Y_{qq} \\ -Y_{qq} & Y_{qq} \end{bmatrix} \begin{bmatrix} \bar{V}_p \\ \bar{V}_n \end{bmatrix} \quad (4.20)$$

$$\Rightarrow \bar{I} = \bar{I}_p + \bar{I}_n^* = \left( \frac{1}{2}Y_{qq} - \frac{1}{2}Y_{qq} \right) \bar{V}_p = 0 \cdot \bar{V}_p \quad (4.21)$$

This result implies that the STATCOM does not provide an impedance in the circuit and acts as a current source at steady state or low-frequency range. Thus, the grid impedance remains the same and the stability is not improved.

Through examining  $dq$ -frame admittances of a SynCon and a STATCOM, it is found that the two differ in providing (or not providing) a reactance at steady state. This difference causes the difference in stability enhancement.

## 4.2 Controller Interaction of STATCOM in Type-4 Wind Farm System

When STATCOM is integrated to a type-4 wind farm system, its controller may interact with wind farm's controller. This interaction is studied by using linear model and root locus analysis.

### 4.2.1 STATCOM on Type-4 Wind Farm

As illustrated in previous section, a STATCOM is connected in a type-4 wind farm system, the circuit topology is shown in Fig. 4.1.

In order to investigate the effects of STATCOM on this power system's stability, a sole type-4 wind farm system is firstly simulated while the STATCOM is not equipped. Fig. 4.10. presents the simulation results of PCC bus voltage. When  $X_g$  increases to 0.42 pu from 0.2 pu, the system becomes unstable and exhibits undamped oscillation. If the  $X_g$  increases to 0.41 pu, the oscillations are suppressed. The simulation case illustrates the marginal stability condition of the type-4 wind farm is when  $X_g=0.42$  pu.

The same cases are implemented when a STATCOM is connected to the system. Fig. 4.23 shows the PCC bus voltage and reactive power from STATCOM under reactive power control and voltage control. The STATCOM is tuned to neither absorbs nor generates any reactive power. It can be observed that the system has the same marginal stability condition, which means the STATCOM can not improve the stability performance under this condition.

To eliminate the impact of STATCOM's controllers, the control loop is disabled, and the firing angle  $\alpha$  is set as a constant to ensure  $Q$  from STATCOM as 0. As shown in Fig. 4.24, the fixed firing angle control can increase the marginal stability condition to 0.49 pu, while the oscillation frequency is about 17 Hz.

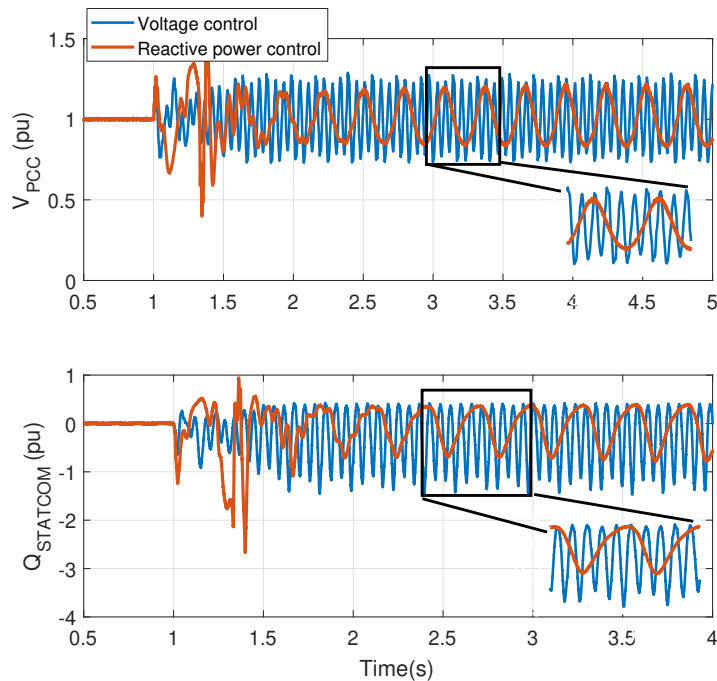


Figure 4.23: PCC bus voltage and reactive power from STATCOM under voltage and reactive power control.  $X_g$  increases to 0.42 pu at 1 second.

These case studies illustrate that the STATCOM's controller has a large impact on the system's stability performance. The detailed analysis will be carried out by using linear model and root locus diagram in next section.

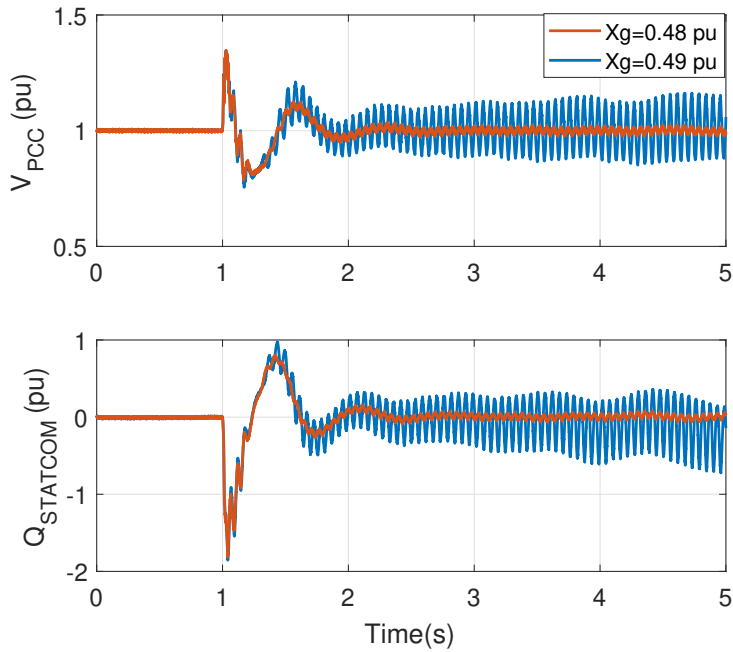


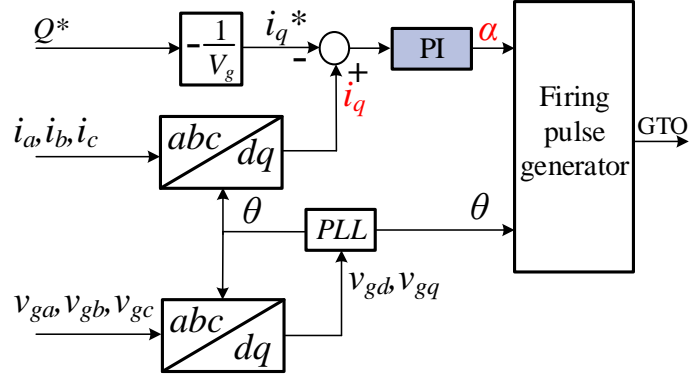
Figure 4.24: PCC bus voltage and reactive power from STATCOM with fixed firing angle control.  $X_g$  increases to 0.48 pu and 0.49 pu at 1 second.

#### 4.2.2 Linear System Identification

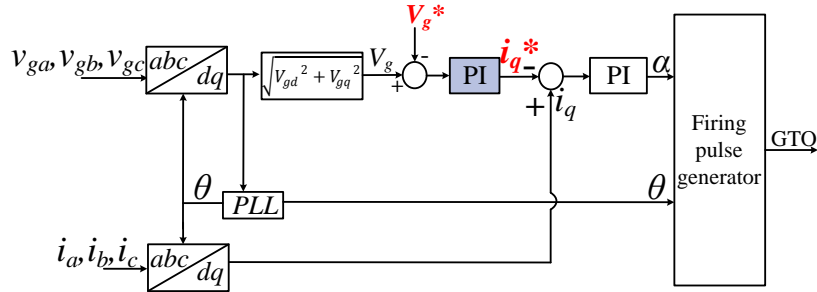
The root locus analysis requires the linear model of the system. However, manufacturers usually do not provide all detail parameters or controller structure to clients. Thus, the system is a black-box model and it is impossible to derive an accurate linear model. Therefore, harmonic injection is an alternative method, which is done by recording the frequency response of the system while injecting a series small disturbances with a certain frequency range. After obtaining the response data, vector fitting is used for the linear system identification.

In reactive power control, the feedback loop is disconnected,  $\alpha$  is set as a constant to ensure there is no power transferred between STATCOM and grid, and a series sinusoidal signals are superimposed on  $\alpha$ , then reactive current  $i_q$  is recorded. Fast Fourier transform (FFT) is applied to extract the component of  $i_q$  at the frequency of injected signals. Similarly, in voltage control, feedback loop is also disconnected, and perturbed signals are added into  $i_q^*$ . In this case,  $V$  is recorded. The injection signals, output measurements and disabled PI





(a)



(b)

Figure 4.25: Block diagram of STATCOM control systems. (a) Reactive power control.(b) Voltage control.

controllers are highlighted in Fig. 4.25. Fig. 4.26 shows the injection circuit block diagram, the plant models are simplified as  $G_i(s)$  and  $G_v(s)$ , and investigated PI controllers are also highlighted with color background. It should be noted that since the reactive power control is unstable when  $X_g$  is 0.42 pu, in order to achieve a stable condition for injection,  $PI_i$  parameter is doubled.

The linear models of the two control systems are defined as follows.

$$G_i(f_i) = \frac{i_q(f_i)}{\alpha(f_i)} \quad (4.22)$$

$$G_v(f_i) = \frac{V(f_i)}{i_q^*(f_i)} \quad (4.23)$$

where  $f_i$  is the injected frequency,  $i_q(f_i)$ ,  $\alpha(f_i)$ ,  $V_g(f_i)$  and  $i_q^*(f_i)$  are the corresponded frequency-domain quantities of signals shown in Fig. 4.26.

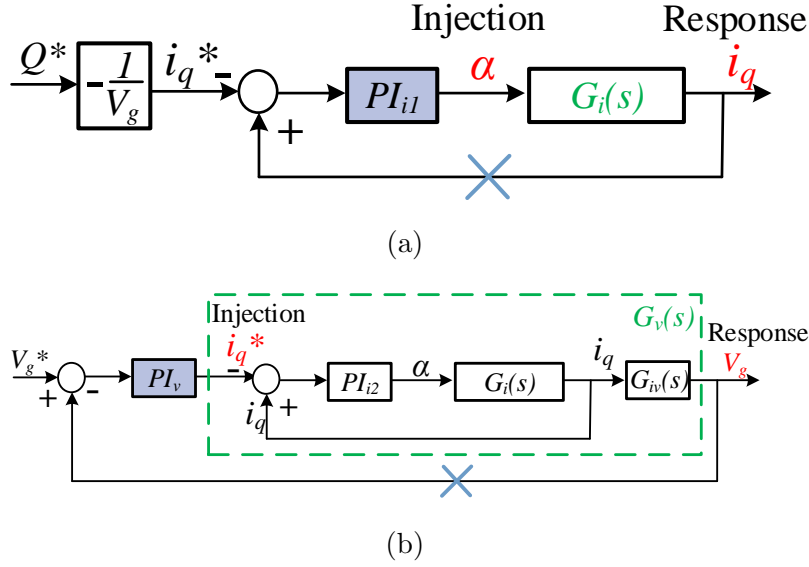
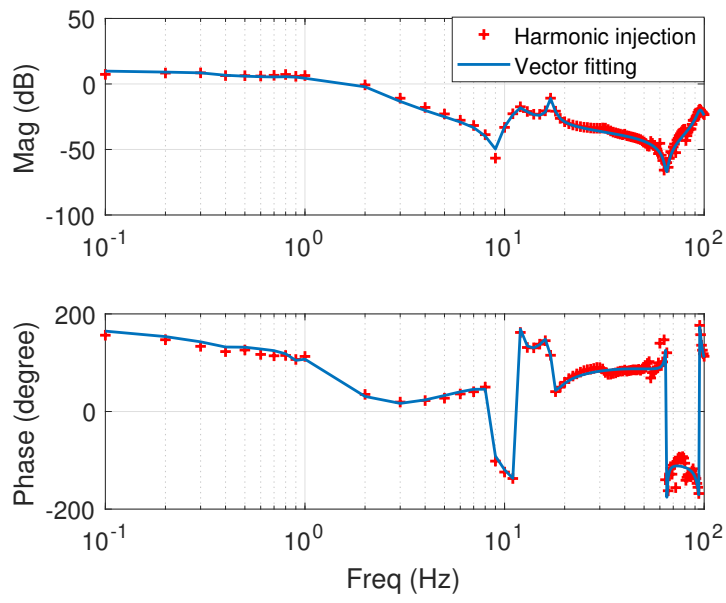


Figure 4.26: Signal injection for obtaining frequency response. (a) Reactive power control,  $PI_{i1}$  is  $5 + \frac{40}{s}$ . (b) Voltage control,  $PI_v$  is  $12 + \frac{300}{s}$ ,  $PI_{i2}$  is  $10 + \frac{80}{s}$ .

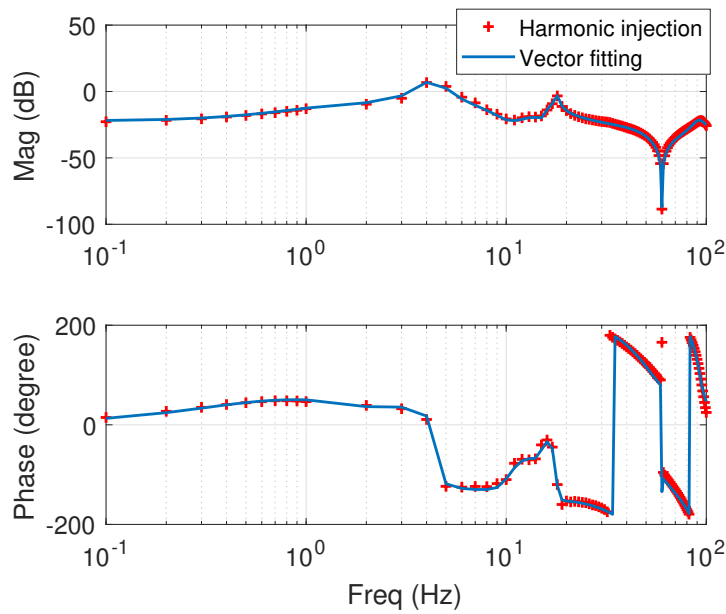
Moreover, the amplitude of injected signals should be chosen such that the disturbance does not influence the normal operation of the power system, and ensures the excited signals have larger magnitude than other frequency's harmonic. Therefore, the amplitudes of injected signals for reactive power and voltage control are 0.03 degree and 0.1 pu, respectively. The injected frequency is 0.1 Hz to 100 Hz, where interval is 0.1 Hz between 0.1 Hz to 0.9 Hz and 1 Hz between 1 Hz to 100 Hz. Fig. 4.27 shows the harmonic injection results, each red cross represents an injected frequency.

With the obtained frequency response measurements, the vector fitting toolbox is used to find their transfer functions. The order of reactive power and voltage control are set as 20 and 21. Comparison of the measurements and transfer function's Bode plot are shown in Fig. 4.27, which illustrates a close matching.

The linear models can be validated through comparing their output responses when subjecting a step change to input. In the open loop control models, feedback loop is disconnected, then  $\alpha$  and  $i_q^*$  are given a step change, respectively. Since large change may cause the instability of system, the amplitude of step changes are chosen as 0.05 degree and 0.05 pu.



(a)



(b)

Figure 4.27: Comparison of the linear model from vector fitting and harmonic injection for (a) reactive power control, (b) voltage control.

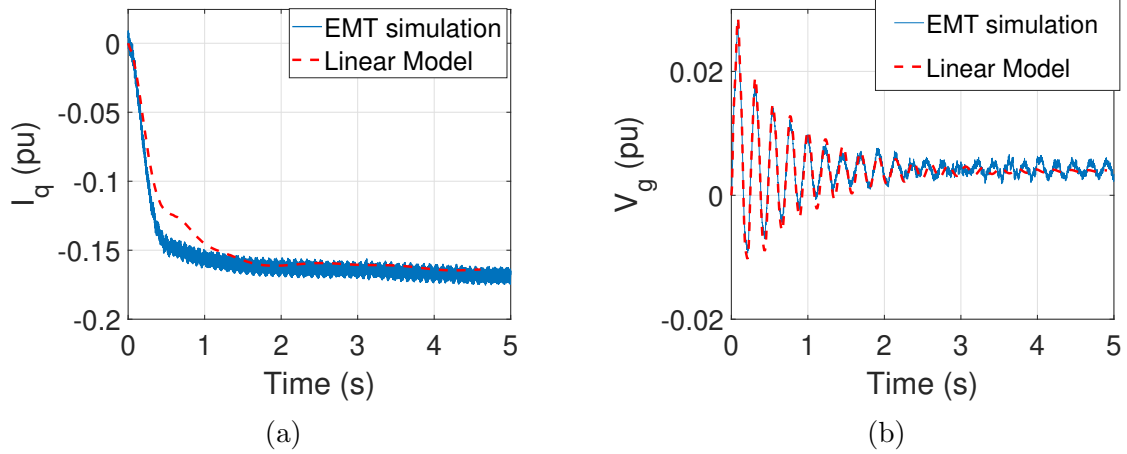


Figure 4.28: Comparison of step change responses. (a)  $\alpha$  has a step change,  $I_q$  is measured. Linear model is  $G_i(s)$ . (b)  $I_q^*$  has a step change,  $V_g$  is measured. Linear model is  $G_v(s)$ .

On the other hand, the step change response of linear models is realized by using MATLAB command '*step*'. The two responses shown in Fig. 4.28 indicates a high similarity between EMT simulation and linear model.

After the accuracy of the linear model is validated by a step change test, the linear models will be applied for stability analysis, as discussed below.

### 4.2.3 Impact of STATCOM Controller on System's Stability

With the obtained linear model, root locus diagrams are plotted to investigate the impact of controller on system stability. As shown in Fig. 4.25, controller signal  $\alpha$  is generated from the PI controller, and its parameter  $5 + \frac{40}{s}$  is regarded as a base case, which means gain is 1 for this case, the root locus diagram is shown in Fig. 4.29. With an increasing gain, a pair of poles will move to right half plane (RHP) to approach an instability condition. But if the gain continues to increase, the poles will move back the LHP, and system becomes stable again.

Three points are selected from the root locus diagram around the y-axis for validation. When the gains are 0.15, 0.6 and 1.5, their poles are  $-0.39 + 11.9i$ ,  $0.454 + 18.3i$  and  $-0.585 + 25.1i$ , respectively. Fig. 4.30 shows the simulation results with the three gains.

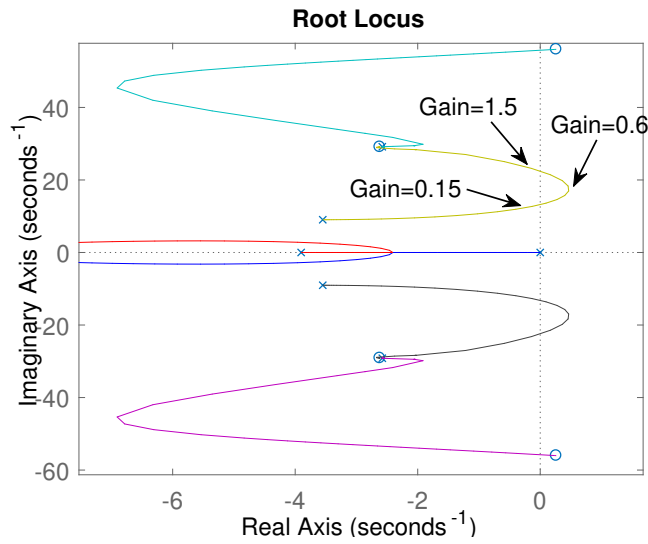


Figure 4.29: Root locus diagram for reactive power control.

At 1 second,  $X_g$  increases to 0.42 pu, the system becomes unstable when gain is 0.6. For the other cases, the system recovers to stability after a period of oscillations. Moreover, the oscillation frequencies are 1.9 Hz, 3 Hz and 4 Hz, which are corresponded to the imaginary parts of these poles.

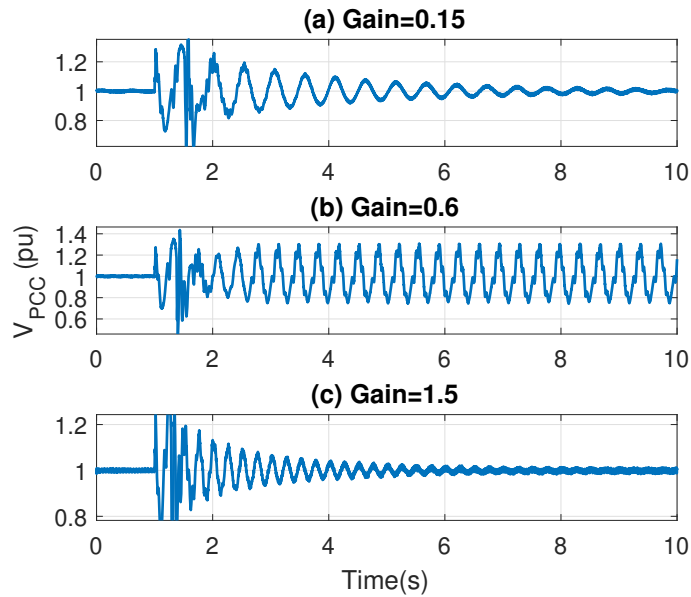


Figure 4.30: PCC bus voltage when  $X_g$  increases to 0.42 pu at 1 second. The STATCOM is under reactive power control with different gains.

The root locus diagram of voltage control is shown in Fig. 4.31. The base value of voltage controller parameter is  $12 + \frac{300}{s}$ . An increasing gain will move a pair of poles to RHP. When gain reaches around 1.1, the system is under marginal stability condition. So two points are chosen, as gains are 1 and 1.2. The pole is  $2.47 + 195i$  when gain is 1.2.

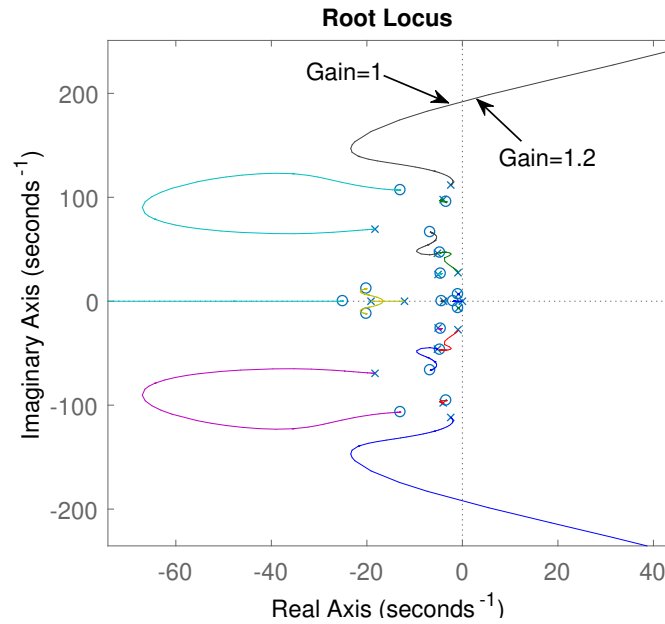


Figure 4.31: Root locus diagram for voltage control.

The simulation results are presented in Fig. 4.32. When  $X_g$  increases to 0.42 pu at 1 second, the system with larger gain becomes unstable, and oscillation is about 31 Hz. The results corroborate the linear model analysis.

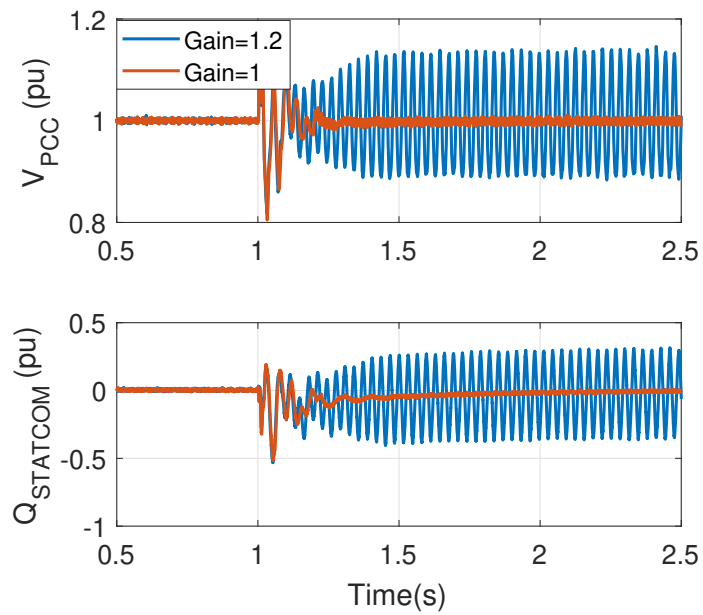


Figure 4.32: PCC bus voltage and reactive power from STATCOM under voltage control with different gains.  $X_g$  increases to 0.42 pu at 1 second.

## Chapter 5: Conclusion and Future Work

### 5.1 Conclusion

This dissertation investigates the stability and interaction of IBRs in power grids. A weak grid-connected three-phase VSC is built as EMT, hardware, and admittance-based test bed. The weak grid oscillation is replicated, and the marginal stability condition and steady-state operation condition of the three test beds are compared and analyzed. Then, the reactive compensation in a type-4 wind farm is presented. Two VAR devices, STATCOM and synchronous condenser, are integrated to the system, and their dynamic performances and admittance models are compared. Moreover, the controller interaction of STATCOM and type-4 wind farm are investigated by using linear model. These areas are concluded in the following paragraphs.

Chapter 2 focuses the modeling and analysis of a grid-following VSC system. The VSC system is implemented in a hardware test bed, admittance-based model and a computer simulation test bed in MATLAB/SimPowerSystems. Since the admittance-based model is obtained from harmonic injection, the procedure is well demonstrated in both MATLAB and PSCAD.

Chapter 3 presents four case studies are carried out under different control methods and different parameters. With the grid-following control, active power is controlled and increased to marginal stability condition. For P/Q control, the oscillation can only be observed with specific parameters. On the other hand, the system with P/V control shows oscillations at marginal stability condition regardless of controller parameters. The response of active power, reactive power and PCC voltage from experiment and simulation are provided and



compared. The good agreement of active power limit, oscillation frequency and steady state variables before events demonstrates the accuracy of the computer simulation test bed.

Chapter 4 presents the stability enhancement and controller interaction for an IBR system. Two VAR devices, STATCOM and SynCon, are examined in a type-4 wind farm system. It has been shown that the SynCon can improve the system stability performance without reactive power compensation, whereas STATCOM only enhances the system by injecting reactive power. This chapter gives an explanation of this phenomenon based on their frequency-domain admittance models. The frequency-domain measurements are obtained from harmonic injection, and the measurement data are fitted into  $s$ -domain models through vector fitting method. Eigenvalue analysis results confirm the observation from the EMT simulation. It is found that SynCon and STATCOM differ in  $dq$ -frame admittance at low-frequency range significantly. The difference also demonstrates as SynCon providing a shunt reactance at steady state while STATCOM providing zero impedance at steady state. This equivalent impedance provided by SynCon helps increase the grid strength to allow more transferred power and enhanced stability. Moreover, this chapter also demonstrates the impact of STATCOM control parameters on system's stability performance. Reactive power control and voltage control are examined. The control loops are disconnected and a series of harmonic signals are injected into the system to generate measurement data. With the frequency response data, a linear plant model can be derived using vector fitting method. Root locus analysis is carried out on the open-loop system to find the gains at marginal stability conditions. Simulation results validate the analysis through stability marginal and oscillation frequency comparison.

## 5.2 Future Work

### 5.2.1 Eigenvalue Analysis for PQ/ $V\theta$ Model

In Chapter 4, stability analysis is realized by using grid side and IBR system's  $dq$ -frame admittance models. The zeros of sum of the two admittance models are the eigenvalue of

whole model. Besides the ad-admittance model, the PQ/V $\theta$  model can also be utilized for stability analysis. Since this PQ/V $\theta$  model of VSC is obtained through harmonic injection, then the grid side's model is required to derived.

Fig. 5.1 shows a transmission line impedance, which consists of a resistor and an inductor,  $V_g$  is grid voltage as  $1\angle 0^\circ$ .

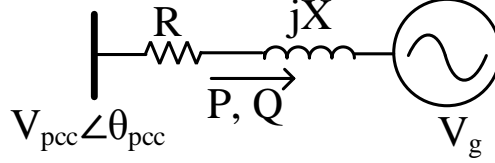


Figure 5.1: A transmission line impedance.

In a power the real and reactive power to grid are written in (5.1) [53].

$$\begin{aligned}
 P_i &= \sum_{k=1}^n |V_i||V_k|[G_{ik} \cos(\theta_i - \theta_k) + B_{ik} \sin(\theta_i - \theta_k)] & i = 1, 2, 3, \dots, n \\
 Q_i &= \sum_{k=1}^n |V_i||V_k|[G_{ik} \sin(\theta_i - \theta_k) - B_{ik} \cos(\theta_i - \theta_k)] & i = 1, 2, 3, \dots, n
 \end{aligned} \tag{5.1}$$

The impedance  $Z$  of the RL circuit is shown in (5.2).

$$Z = \frac{1}{R + sL + j\omega L} \tag{5.2}$$

And  $G$  is conductance and  $B$  is susceptance.

$$\begin{aligned}
 G &= \frac{R + sL}{(R + sL)^2 + (\omega L)^2} \\
 B &= \frac{\omega L}{(R + sL)^2 + (\omega L)^2}
 \end{aligned} \tag{5.3}$$

Put (5.3) into (5.1), the power flow can be written as follows.

$$\begin{aligned}
 P &= |V_{pcc}|^2 G - |V_{pcc}||V_g|(G \cos \theta_{pcc} - B \sin \theta_{pcc}) \\
 Q &= |V_{pcc}|^2 B - |V_{pcc}||V_g|(G \sin \theta_{pcc} + B \cos \theta_{pcc})
 \end{aligned} \tag{5.4}$$

Thus, the PQ/V $\theta$  model is written as a Jacobian matrix.

$$\begin{bmatrix} \Delta P \\ \Delta Q \end{bmatrix} = \underbrace{\begin{bmatrix} G_{11} & G_{12} \\ G_{21} & G_{22} \end{bmatrix}}_{G_{grid}} \begin{bmatrix} \Delta V \\ \Delta \theta \end{bmatrix} \quad (5.5)$$

Each element is calculated as follows.

$$\begin{aligned} G_{11} &= \frac{\partial P}{\partial V_{pcc}} = 2|V_{pcc}|G - |V_g|(G \cos \theta_{pcc} - B \sin \theta_{pcc}) \\ G_{12} &= \frac{\partial P}{\partial \theta_{pcc}} = -|V_{pcc}||V_g|(G \sin \theta_{pcc} + B \cos \theta_{pcc}) \\ G_{21} &= \frac{\partial Q}{\partial V_{pcc}} = 2|V_{pcc}|B - |V_g|(G \sin \theta_{pcc} + B \cos \theta_{pcc}) \\ G_{22} &= \frac{\partial Q}{\partial \theta_{pcc}} = |V_{pcc}||V_g|(G \cos \theta_{pcc} - B \sin \theta_{pcc}) \end{aligned} \quad (5.6)$$

In a grid-connected VSC model, the PQ/V $\theta$  model at PCC point is calculated in (5.7).

$$\begin{bmatrix} \Delta P_1 + \Delta P_2 \\ \Delta Q_1 + \Delta Q_2 \end{bmatrix} = \underbrace{[G_{grid} + G_{VSC}]}_{G_{total}} \begin{bmatrix} \Delta V \\ \Delta \theta \end{bmatrix} = 0 \quad (5.7)$$

With the linear model of  $G_{total}$ , eigenvalue analysis can be carried out to conduct stability analysis.

### 5.2.2 Participation Factor Analysis

Case studies in Chapter 3 illustrate some oscillation phenomena of VSC in weak grid. However, we still do not find which states are most relevant to oscillation. From participation factor analysis, we can reveal the most influencing state on oscillation mode. This analysis will be validated with EMT model and frequency response model, such as  $dq$ -frame admittance and PQ/V $\theta$  model.

## References

- [1] U.S. Energy Information Administration. Annual energy outlook 2021, <https://www.eia.gov/todayinenergy/detail.php?id=46676>.
- [2] Liansong Xiong, Fang Zhuo, Feng Wang, Xiaokang Liu, Ying Chen, Minghua Zhu, and Hao Yi. Static synchronous generator model: A new perspective to investigate dynamic characteristics and stability issues of grid-tied pwm inverter. *IEEE Transactions on Power Electronics*, 31(9):6264–6280, 2016.
- [3] Huakun Liu, Xiaorong Xie, Jingbo He, Tao Xu, Zhao Yu, Chao Wang, and Chuanyu Zhang. Subsynchronous interaction between direct-drive pmsg based wind farms and weak ac networks. *IEEE Transactions on Power Systems*, 32(6):4708–4720, 2017.
- [4] Shun-Hsien Huang, John Schmall, Jose Conto, John Adams, Yang Zhang, and Cathey Carter. Voltage control challenges on weak grids with high penetration of wind generation: Ercot experience. In *2012 IEEE Power and Energy Society General Meeting*, pages 1–7, 2012.
- [5] Lingling Fan and Zhixin Miao. An explanation of oscillations due to wind power plants weak grid interconnection. *IEEE Transactions on Sustainable Energy*, 9(1):488–490, 2018.
- [6] Yin Li, Lingling Fan, and Zhixin Miao. Wind in weak grids: Low-frequency oscillations, subsynchronous oscillations, and torsional interactions. *IEEE Transactions on Power Systems*, 35(1):109–118, 2020.

- [7] Lingling Fan and Zhixin Miao. Wind in weak grids: 4 hz or 30 hz oscillations? *IEEE Transactions on Power Systems*, 33(5):5803–5804, 2018.
- [8] Yin Li, Lingling Fan, and Zhixin Miao. Stability control for wind in weak grids. *IEEE Transactions on Sustainable Energy*, 10(4):2094–2103, 2019.
- [9] Mostafa Farrokhabadi, Claudio A. Cañizares, John W. Simpson-Porco, Ehsan Nasr, Lingling Fan, Patricio A. Mendoza-Araya, Reinaldo Tonkoski, Ujjwol Tamrakar, Nikos Hatziargyriou, Dimitris Lagos, Richard W. Wies, Mario Paolone, Marco Liserre, Lasantha Meegahapola, Mahmoud Kabalan, Amir H. Hajimiragha, Dario Peralta, Marcelo A. Elizondo, Kevin P. Schneider, Francis K. Tuffner, and Jim Reilly. Microgrid stability definitions, analysis, and examples. *IEEE Transactions on Power Systems*, 35(1):13–29, 2020.
- [10] Frede Blaabjerg and Ke Ma. Future on power electronics for wind turbine systems. *IEEE Journal of Emerging and Selected Topics in Power Electronics*, 1(3):139–152, 2013.
- [11] Yunhui Huang, Xiaoming Yuan, Jiabing Hu, and Pian Zhou. Modeling of vsc connected to weak grid for stability analysis of dc-link voltage control. *IEEE Journal of Emerging and Selected Topics in Power Electronics*, 3(4):1193–1204, 2015.
- [12] G. Reed, R. Pape, and M. Takeda. Advantages of voltage sourced converter (vsc) based design concepts for facts and hvdc-link applications. In *2003 IEEE Power Engineering Society General Meeting (IEEE Cat. No.03CH37491)*, volume 3, pages 1816–1821 Vol. 3, 2003.
- [13] Bo Wen, Dong Dong, Dushan Boroyevich, Rolando Burgos, Paolo Mattavelli, and Zhiyu Shen. Impedance-based analysis of grid-synchronization stability for three-phase paralleled converters. *IEEE Transactions on Power Electronics*, 31(1):26–38, 2016.

- [14] Pinaki Mitra, Lidong Zhang, and Lennart Harnefors. Offshore wind integration to a weak grid by vsc-hvdc links using power-synchronization control: A case study. *IEEE Transactions on Power Delivery*, 29(1):453–461, 2014.
- [15] Xia Jiang, Xinghao Fang, Joe H. Chow, Abdel-Aty Edris, Edvina Uzunovic, Michael Parisi, and Liana Hopkins. A novel approach for modeling voltage-sourced converter-based facts controllers. *IEEE Transactions on Power Delivery*, 23(4):2591–2598, 2008.
- [16] Nikolas Flourentzou, Vassilios G. Agelidis, and Georgios D. Demetriades. Vsc-based hvdc power transmission systems: An overview. *IEEE Transactions on Power Electronics*, 24(3):592–602, 2009.
- [17] IEEE PES WindSSO Taskforce. *PES TR-80: Wind Energy Systems Subsynchronous Oscillations: Events and Modeling*. 2020.
- [18] Yunzhi Cheng, Lingling Fan, Jonathan Rose, Fred Huang, John Schmall, Xiaoyu Wang, Xiaorong Xie, Jan Shair, Jayanth Ramamurthy, Nilesh Modi, Chun Li, Chen Wang, Shahil Shah, Bikash Chandra Pal, Zhixin Miao, Andrew Isaacs, Jean Mahseredjian, and Zheng Jenny Zhou. Real-world subsynchronous oscillation events in power grids with high penetrations of inverter-based resources. *IEEE Transactions on Power Systems*, pages 1–1, 2022.
- [19] NERC. Reliability Guideline Forced Oscillation Monitoring & Mitigation, September 2017.
- [20] J. Dixon, L. Moran, J. Rodriguez, and R. Domke. Reactive power compensation technologies: State-of-the-art review. *Proceedings of the IEEE*, 93(12):2144–2164, 2005.
- [21] John Liston. Typical synchronous condenser installations. *General Electric Company Review*, 14:234–241, 1911.
- [22] 2018 state of the market report for the ercot electricity markets, 2019.

- [23] J. Skliutas, D. LaForest, R. D'Aquila, D. Derr, and E. Kronbeck. Next-generation synchronous condenser installation at the velco granite substation. In *2009 IEEE Power Energy Society General Meeting*, pages 1–8, 2009.
- [24] B Singh, R Saha, Ambrish Chandra, and Kamal Al-Haddad. Static synchronous compensators (statcom): a review. *IET Power Electronics*, 2(4):297–324, 2009.
- [25] G. Reed, J. Paserba, T. Croasdaile, M. Takeda, Y. Hamasaki, T. Aritsuka, N. Morishima, S. Jochi, I. Iyoda, M. Nambu, N. Toki, L. Thomas, G. Smith, D. LaForest, W. Allard, and D. Haas. The velco statcom based transmission system project. In *2001 IEEE Power Engineering Society Winter Meeting. Conference Proceedings (Cat. No.01CH37194)*, volume 3, pages 1109–1114 vol.3, 2001.
- [26] A. Hoke, V. Gevorgian, S. Shah, P. Koralewicz, R. W. Kenyon, and B. Kroposki. Island power systems with high levels of inverter-based resources: Stability and reliability challenges. *IEEE Electrification Magazine*, 9(1):74–91, 2021.
- [27] The age of the syncons, 2019. <https://www.energynetworks.com.au/news/energy-insider/age-syncons/>. accessed: 2021-09-02.
- [28] Trevor Lim and Total Eren. A generator's perspective. <https://aemo.com.au/en/learn/energy-explained/system-strength-workshop>.
- [29] Dewu Shu, Xiaorong Xie, Hong Rao, Xiaodan Gao, Qirong Jiang, and Ying Huang. Sub- and super-synchronous interactions between statcoms and weak ac/dc transmissions with series compensations. *IEEE Transactions on Power Electronics*, 33(9):7424–7437, 2018.
- [30] B. Gustavsen and A. Semlyen. Rational approximation of frequency domain responses by vector fitting. *IEEE Transactions on Power Delivery*, 14(3):1052–1061, 1999.

- [31] Yao Xu and Fangxing Li. Adaptive pi control of statcom for voltage regulation. *IEEE Transactions on Power Delivery*, 29(3):1002–1011, 2014.
- [32] An Luo, Ci Tang, Zhikang Shuai, Jie Tang, Xian Yong Xu, and Dong Chen. Fuzzy-pi-based direct-output-voltage control strategy for the statcom used in utility distribution systems. *IEEE Transactions on Industrial Electronics*, 56(7):2401–2411, 2009.
- [33] A. I. Semlyen. s-domain methodology for assessing the small signal stability of complex systems in nonsinusoidal steady state. *IEEE Transactions on Power Systems*, 14(1):132–137, 1999.
- [34] L. Fan and Z. Miao. Admittance-based stability analysis: Bode plots, nyquist diagrams or eigenvalue analysis? *IEEE Transactions on Power Systems*, 35(4):3312–3315, 2020.
- [35] Mohammad Kazem Bakhshizadeh, Changwoo Yoon, Jesper Hjerrild, Claus Leth Bak, Lukasz Hubert Kocewiak, Frede Blaabjerg, and Bo Hesselbæk. The application of vector fitting to eigenvalue-based harmonic stability analysis. *IEEE Journal of Emerging and Selected Topics in Power Electronics*, 5(4):1487–1498, 2017.
- [36] Chroma. Labview driver installation guide, <https://www.chromausa.com/document-library/labview-driver-installation-guide/>.
- [37] J. Huang, K. A. Corzine, and M. Belkhat. Small-signal impedance measurement of power-electronics-based ac power systems using line-to-line current injection. *IEEE Transactions on Power Electronics*, 24(2):445–455, Feb 2009.
- [38] B. Badrzadeh, M. Sahni, Y. Zhou, D. Muthumuni, and A. Gole. General methodology for analysis of sub-synchronous interaction in wind power plants. *IEEE Transactions on Power Systems*, 28(2):1858–1869, May 2013.





- [39] N. Johansson, L. Ängquist, and H. Nee. A comparison of different frequency scanning methods for study of subsynchronous resonance. *IEEE Transactions on Power Systems*, 26(1):356–363, Feb 2011.
- [40] G. Francis, R. Burgos, D. Boroyevich, F. Wang, and K. Karimi. An algorithm and implementation system for measuring impedance in the d-q domain. In *2011 IEEE Energy Conversion Congress and Exposition*, pages 3221–3228, Sep. 2011.
- [41] A. Yazdani and R. Iravani. *Voltage-Sourced Converters in Power Systems: Modeling, Control, and Applications*. Wiley, 2010.
- [42] M. Jaksic, D. Boroyevich, R. Burgos, Z. Shen, I. Cvetkovic, and P. Mattavelli. Modular interleaved single-phase series voltage injection converter used in small-signal dq impedance identification. In *2014 IEEE Energy Conversion Congress and Exposition (ECCE)*, pages 3036–3045, Sep. 2014.
- [43] P.K. Rajan and Arun Sekar. 1 - linear circuit analysis. In WAI-KAI CHEN, editor, *The Electrical Engineering Handbook*, pages 3–29. Academic Press, Burlington, 2005.
- [44] Li Bao, Lingling Fan, Zhixin Miao, and Zhengyu Wang. Hardware demonstration of weak grid oscillations in grid-following converters. In *2021 North American Power Symposium (NAPS)*, pages 01–06, 2021.
- [45] Li Bao, Lingling Fan, and Zhixin Miao. Wind farms in weak grids stability enhancement: Syncon or statcom? *Electric Power Systems Research*, 202:107623, 2022.
- [46] Li Bao, Lingling Fan, and Zhixin Miao. Control interaction of statcom and type-4 wind turbines. *2022 IEEE Power Energy Society General Meeting (PESGM)*.
- [47] Matlab. Statcom (detailed model), <https://www.mathworks.com/help/physmod/sps-/ug/statcom-detailed-model.html;jsessionid=27a0ed8be24ebda6d117a511cdd9>.

- [48] N. G. Hingorani and L. Gyugyi. *Static Shunt Compensators: SVC and STATCOM*, pages 135–207. 2000.
- [49] IEEE Recommended Practice for Excitation System Models for Power System Stability Studies. *IEEE Std 421.5-1992*, pages 1–56, 1992.
- [50] J. Sun. Small-signal methods for ac distributed power systems—a review. *IEEE Transactions on Power Electronics*, 24(11):2545–2554, Nov 2009.
- [51] Sigurd Skogestad and I Postlethwaite. *Multivariable Feedback Control: Analysis and Design*, volume 2. 01 2005.
- [52] A. Rygg, M. Molinas, C. Zhang, and X. Cai. A modified sequence-domain impedance definition and its equivalence to the dq-domain impedance definition for the stability analysis of ac power electronic systems. *IEEE Journal of Emerging and Selected Topics in Power Electronics*, 4(4):1383–1396, 2016.
- [53] A.R. Bergen. *Power Systems Analysis*. Prentice-Hall series in electrical and computer engineering. Prentice-Hall, 1986.

## Appendix A: Copyright Permissions

The permission below is for Fig. 1.2.

Home Help ▾ Live Chat Sign in Create Account



Voltage control challenges on weak grids with high penetration of wind generation: ERCOT experience

Conference Proceedings: 2012 IEEE Power and Energy Society General Meeting

Author: Shun-Hsien Huang

Publisher: IEEE

Date: July 2012

Copyright © 2012, IEEE

### Thesis / Dissertation Reuse

The IEEE does not require individuals working on a thesis to obtain a formal reuse license, however, you may print out this statement to be used as a permission grant:

*Requirements to be followed when using any portion (e.g., figure, graph, table, or textual material) of an IEEE copyrighted paper in a thesis:*

- 1) In the case of textual material (e.g., using short quotes or referring to the work within these papers) users must give full credit to the original source (author, paper, publication) followed by the IEEE copyright line © 2011 IEEE.
- 2) In the case of illustrations or tabular material, we require that the copyright line © [Year of original publication] IEEE appear prominently with each reprinted figure and/or table.
- 3) If a substantial portion of the original paper is to be used, and if you are not the senior author, also obtain the senior author's approval.

*Requirements to be followed when using an entire IEEE copyrighted paper in a thesis:*

- 1) The following IEEE copyright/ credit notice should be placed prominently in the references: © [year of original publication] IEEE. Reprinted, with permission, from [author names, paper title, IEEE publication title, and month/year of publication]
- 2) Only the accepted version of an IEEE copyrighted paper can be used when posting the paper or your thesis on-line.
- 3) In placing the thesis on the author's university website, please display the following message in a prominent place on the website: In reference to IEEE copyrighted material which is used with permission in this thesis, the IEEE does not endorse any of [university/educational entity's name goes here]'s products or services. Internal or personal use of this material is permitted. If interested in reprinting/republishing IEEE copyrighted material for advertising or promotional purposes or for creating new collective works for resale or redistribution, please go to [http://www.ieee.org/publications\\_standards/publications/rights/rights\\_link.html](http://www.ieee.org/publications_standards/publications/rights/rights_link.html) to learn how to obtain a License from RightsLink.

If applicable, University Microfilms and/or ProQuest Library, or the Archives of Canada may supply single copies of the dissertation.

BACK

CLOSE WINDOW

The permission below is for the reproduction of material in Chapter 3.

6/1/22, 11:08 AM

Rightslink® by Copyright Clearance Center



- Home
- Help
- Live Chat
- Sign in
- Create Account



### Hardware Demonstration of Weak Grid Oscillations in Grid-Following Converters

Conference Proceedings: 2021 North American Power Symposium (NAPS)

Author: Li Bao

Publisher: IEEE

Date: 14 Nov. 2021

Copyright © 2021, IEEE

#### Thesis / Dissertation Reuse

The IEEE does not require individuals working on a thesis to obtain a formal reuse license, however, you may print out this statement to be used as a permission grant:

*Requirements to be followed when using any portion (e.g., figure, graph, table, or textual material) of an IEEE copyrighted paper in a thesis:*

- 1) In the case of textual material (e.g., using short quotes or referring to the work within these papers) users must give full credit to the original source (author, paper, publication) followed by the IEEE copyright line © 2011 IEEE.
- 2) In the case of illustrations or tabular material, we require that the copyright line © [Year of original publication] IEEE appear prominently with each reprinted figure and/or table.
- 3) If a substantial portion of the original paper is to be used, and if you are not the senior author, also obtain the senior author's approval.

*Requirements to be followed when using an entire IEEE copyrighted paper in a thesis:*

- 1) The following IEEE copyright/ credit notice should be placed prominently in the references: © [year of original publication] IEEE. Reprinted, with permission, from [author names, paper title, IEEE publication title, and month/year of publication]
- 2) Only the accepted version of an IEEE copyrighted paper can be used when posting the paper or your thesis on-line.
- 3) In placing the thesis on the author's university website, please display the following message in a prominent place on the website: In reference to IEEE copyrighted material which is used with permission in this thesis, the IEEE does not endorse any of [university/educational entity's name goes here]'s products or services. Internal or personal use of this material is permitted. If interested in reprinting/republishing IEEE copyrighted material for advertising or promotional purposes or for creating new collective works for resale or redistribution, please go to [http://www.ieee.org/publications\\_standards/publications/rights/rights\\_link.html](http://www.ieee.org/publications_standards/publications/rights/rights_link.html) to learn how to obtain a License from RightsLink.

If applicable, University Microfilms and/or ProQuest Library, or the Archives of Canada may supply single copies of the dissertation.

BACK

CLOSE WINDOW

© 2022 Copyright - All Rights Reserved | [Copyright Clearance Center, Inc.](#) | [Privacy statement](#) | [Terms and Conditions](#)  
Comments? We would like to hear from you. E-mail us at [customer@copyright.com](mailto:customer@copyright.com)

The permission below is for the reproduction of material in Chapter 4.

6/1/22, 11:15 AM

Rightslink® by Copyright Clearance Center



### Wind farms in weak grids stability enhancement: SynCon or STATCOM?

Author: Li Bao, Lingling Fan, Zhixin Miao  
Publication: Electric Power Systems Research  
Publisher: Elsevier  
Date: January 2022

© 2021 Elsevier B.V. All rights reserved.

#### Journal Author Rights

Please note that, as the author of this Elsevier article, you retain the right to include it in a thesis or dissertation, provided it is not published commercially. Permission is not required, but please ensure that you reference the journal as the original source. For more information on this and on your other retained rights, please visit: <https://www.elsevier.com/about/our-business/policies/copyright#Author-rights>

BACK

CLOSE WINDOW

© 2022 Copyright - All Rights Reserved | [Copyright Clearance Center, Inc.](#) | [Privacy statement](#) | [Terms and Conditions](#)  
Comments? We would like to hear from you. E-mail us at [customercare@copyright.com](mailto:customercare@copyright.com)

## **About the Author**

Li Bao was born in 1992 in Liupanshui, China. He received the B.S. degree in electrical engineering from Northwestern Polytechnical University, Xi'an, China, in 2015, and the M.S. degree in electrical engineering from University of South Florida, Tampa, USA, in 2016. He is currently pursuing the Ph.D. degree in electrical engineering in the University of South Florida, Tampa, USA. His research interests include the renewable energy, EMT modeling, impedance-based weak grid stability analysis, reactive power compensation, and system identification.